



SAPIENZA
UNIVERSITÀ DI ROMA

Wake fields and impedance calculations of LHC collimators' real structures

Dipartimento di Fisica

Dottorato di Ricerca in Fisica degli Acceleratori – XXVIII Ciclo

Candidate

Oscar Frasciello

ID number 1224545

Thesis Advisors

Prof. Mauro Migliorati

Dr. Mikhail Zobov

Co-Advisor

Dr. Simone Di Mitri

A thesis submitted in partial fulfillment of the requirements
for the degree of Doctor of Philosophy in Accelerator Physics

October 2015

Wake fields and impedance calculations of LHC collimators' real structures
Ph.D. thesis. Sapienza – University of Rome

© 2015 Oscar Frasciello. All rights reserved

This thesis has been typeset by \LaTeX and the Sapthesis class.

Author's email: oscar.frasciello@lnf.infn.it

To Lucia and Federico, for their conscious and unconscious patience...

Acknowledgments

When I started working on the subject of wake fields and impedances in particle accelerators, I did not know anything about how something that I always ascribed only to the Ohm's law could be of such a concern in particle's world. Nor that something I always thought to be fully revealed and described with superb clarity by J. C. Maxwell, almost two centuries ago, could be of such an impressive and latest developments.

Not even I ever thought to have the great chance and honour to work for two prestigious and world renowned scientific institutions, the Italian National Institute for Nuclear Physics, National Laboratories of Frascati (INFN-LNF) and the European Center for Nuclear Physics (CERN), in Geneva. Despite the gratification, however, it was a hard challenge.

I owe to all those people who I encountered along the way, for their support and their contribution to my present experience.

Thanks to Mikhail Zobov, who has followed me as the principal supervisor of this PhD work, throughout the open up mysteries of wake fields and the stimulating requirements of the HiLumi LHC project. To Mauro Migliorati and Simone Di Mitri, for their careful support and the useful discussions. Thanks also to David Alesini and Sandro Tomassini for their help, as well as to Alessandro Gallo, who let me resonate guitar strings apart from electromagnetic fields. Thanks to Andrea Ghigo, as the head of the LNF Accelerator Division, for having given me the opportunity to start working in the field of Accelerator Physics and, thus, instilled the beginning of this work.

I am thankful to the CERN colleagues Elias Metral, Benoit Salvant, Nicolas Mounet, Alexej Grudiev, Nicolò Biancacci and Luca Gentini. Thanks for the many informations shared, for the many discussions, for the support and for having listened to me during the many meetings at CERN and around the world.

I devote special thanks to Warner Bruns, for his invaluable support, every time a stuck, a bug or an "oops!" revealed their harmful potential.

Kind thoughts of gratitude are addressed to Adolfo Esposito, Maurizio Pelliccioni and Fiorello Martire, for their authentic friendship and the chance they gave me to look forward into the future, once again, with passion. Among neutrons, photons and all other charged particles, there is also the need to protect ourselves from fast meals and lonely cigarettes. Thanks to Tiziano Ferro, for his presence and straight friendship.

To you, being always with me even if we never find a way to meet, so far but so brotherly close to each other, what loving does really mean...grazie Compare!

Thanks to my large family, no words are needed to explain why.

Thanks to life, for having opened up the real beauty to my eyes and inspired the dedication of this work, day by day.

This work was supported by HiLumi LHC Design Study, which is included in the High Luminosity LHC project and is partly funded by the European Commission within the Framework Programme 7 Capacities Specific Programme, Grant Agreement 284404.

Eppur ti vidi nascere,
al chiarore di un sole sbiadito
in un timido autunno.
Remissivi si fecer da parte,
lasciando il cielo obnubilato
e anelo del suo albore,
al fulgor dei giorni nostri.
Di tal bellezza ci commovemmo,
di magnifica pienezza
tuoi devoti
ci iniziasti a vivere.

Oscar Frasciello

Abstract

The Large Hadron Collider (LHC) hosted at CERN, the European Organization for Nuclear Research in Geneva, Switzerland, is the world's largest particle accelerator. With a circumference of 27 km, it can bring proton beams into collisions at a centre of mass energy of 14 TeV. It has been conceived and built to let scientific research to explore the high energy physics frontiers, keeping collision events at a design luminosity of $10^{34} \text{ cm}^{-2}\text{s}^{-1}$.

Beyond this goal challenging in itself, the High Luminosity LHC (HiLumi-LHC) project aims at increasing the LHC luminosity by an order of magnitude and one of the key ingredients to achieve that is to increase beam intensity. In order to keep beam instabilities under control and to avoid excessive power losses a careful design of new vacuum chamber components and continuous update and improvement of the LHC impedance model are required.

Collimators are among the major impedance contributors. During LHC Run I, measurements with beam have revealed that the betatron coherent tune shifts were higher by about a factor of 2 with respect to the theoretical predictions based on the impedance model up to 2012. In that model the resistive wall impedance was considered as the dominating impedance contribution for collimators. By means of GdfidL electromagnetic code simulations, the geometric impedance of secondary and tertiary (TCS/TCT) collimators' real structures (i.e. not simplified) was calculated, contributing to the update of the LHC impedance model. This resulted also in a better agreement between the measured and simulated betatron tune shifts.

During the LHC Long Shutdown I (LS I), some of the Run I TCS and TCT collimators were replaced by new devices, embedding Beam Position Monitor (BPM) pick-up buttons in the tapering regions, in order to provide accurate and continuous measurements of the beam centres, and ferrite blocks for the damping of the Higher Order Modes (HOMs) trapped in the collimators' structure.

The injection collimators (TDI) are undergoing a substantial design review and upgrade study stage, as part of the whole LHC injection protection system upgrade foreseen to be finished in the LHC LS II (2018-2019). Measurements performed during LHC Run I have shown that the presently installed TDIs contribute significantly to both longitudinal and transverse impedance, determining beam induced heating and high vacuum pressure that affected background of experiments. In the view of higher intensities planned for the Run III and HiLumi-LHC operations, all these impedance related issues have to be minimized.

The aim of this work was to perform accurate simulations of collimators' impedance, which has become very important and challenging. Accurate does mean as close as possible to the real conditions. Thus, in order to afford such a task, the huge collimators' CAD designs were used as input into GdfidL code. Besides, several dedicated tests have been performed to verify correct simulations of lossy dispersive material properties, such as resistive wall and ferrites, benchmarking code results with analytical, semi-analytical and other numerical codes outcomes. The results of the collimators wake fields and impedances calculations, together with their comparison with experimental measurements are shown and discussed.

Contents

1	Introduction	3
1.1	The CERN Large Hadron Collider	3
1.2	The High Luminosity LHC project	7
1.3	The LHC collimation system	9
2	Wake fields and beam coupling impedances	14
2.1	Where do Wake fields originate from	14
2.2	Panofsky-Wenzel theorem and Wake functions	19
2.2.1	Basic approximations	19
2.2.2	The Panofsky-Wenzel theorem	20
2.2.3	Decomposition into modes and Wake functions definition . .	21
2.2.4	General properties of Wake functions	23
2.3	Wake Potentials	24
2.4	Beam coupling Impedance	25
2.4.1	Longitudinal impedance	25
2.4.2	Transverse impedance	27
2.4.3	General properties of impedances	27
2.4.4	Resonator impedance	29
2.4.5	Bunch modes	31
2.4.6	Loss factor, kick factor and effective impedance	35
2.5	Collective effects	38
2.5.1	Single bunch	38
2.5.2	Multi-bunch	40
3	LHC Run I TCS-TCT collimators	42
3.1	Theoretical considerations	45
3.1.1	Geometric and resistive wall kick factors evaluation	46
3.2	Numerical calculations	47
3.3	LHC impedance model update	50
4	Simulation tests of resistive and dispersive properties of materials in GdfidL	56
4.1	RW simulation tests	56
4.1.1	Resistive cylindrical pipe	56
4.1.2	Beam pipe with thick resistive insert	59
4.2	Ferrite Material Simulation Test	61

4.2.1	Scattering parameter S_{11} of a coaxial probe	63
4.2.2	Impedance of a ferrite filled pillbox	65
4.2.3	Tsutsui model for TT2-111R ferrite kicker	66
5	LHC Run II TCS/TCT collimators	73
5.1	New TCS/TCT's taper design optimization study	74
5.1.1	Resistive wall impedance contribution from the new angle set	76
5.2	TCS/TCT impedance study	78
5.2.1	S_{1x} parameters simulations vs loop measurements	81
5.2.2	Z_{\perp} simulations versus wire measurements	82
6	LHC TDI collimators	88
6.1	TDI taper optimization study	89
6.2	TDIS' real structures impedance study	91
7	Conclusions	98
A	The linear accelerator model	100
B	The GdfidL Finite Difference code	102

PhD activity related outcomes

Publications

1. N. Biancacci *et al.*, “Impedance simulations and measurements on the LHC TCTP collimators with embedded BPMs”, *Physical Review Special Topics - Accelerators and Beams*, to be submitted.
2. O. Frasciello *et al.*, “Geometric beam coupling impedance of LHC secondary collimators”, *Nuclear Instruments and Methods in Physics Research Section A*, 2015. DOI:10.1016/j.nima.2015.11.139
3. O. Frasciello *et al.*, “Numerical Calculations of Wake Fields and Impedances of LHC Collimators’ Real Structures”, *Proceedings of ICAP 2015*, Shanghai, China. arXiv:1511.01236.
4. J. Uythoven *et al.*, “Injection protection upgrade for the HL-LHC”, *Proceedings of IPAC 2015*, Richmond, VA, USA, TUPTY051.
5. B. Salvant *et al.*, “Expected Impact of Hardware Changes on Impedance and Beam-induced Heating during Run 2”, *Proceedings of LHC Performance Workshop*, Chamonix, France, September 22-25, 2014.
6. The HiLumi LHC Collaboration, “HL-LHC Preliminary Design Report : Deliverable: D1.5”, CERN-ACC-2014-0300.
7. E. Metral, “Beam intensity limitations”, CERN-ACC-2014-0297.
8. O. Frasciello *et al.*, “Geometric beam coupling impedance of LHC secondary collimators”, *Proceedings of IPAC 2014*, Dresden, Germany, TUPRI049.
9. N. Mounet *et al.*, “Tranverse impedance in the HL-LHC era”, CERN-ACC-SLIDES-2014-0085.

Scientific talks

1. “Numerical Calculations of Wake Fields and Impedances of LHC Collimators’ Real Structures”, **Invited talk** at ICAP 2015, October 16th, 2015, Shanghai, China.

2. “Wake fields and impedances of LHC collimators”, **Invited talk** at 100th National Congress of the Italian Physical Society (SIF), September 22 - 26 2014, Pisa, Italy.
3. “Beam coupling impedance of the new LHC collimators”, Contributed talk at 101st National Congress of the Italian Physical Society (SIF), September 24th 2015, Rome, Italy.
4. “Present status and future plans of LHC collimators wake fields and impedances simulations”, Contributed talk at BE-ABP Impedance meeting, March 23rd 2015, CERN, Geneva, Switzerland.
5. “Wake fields and impedances calculations with GdfidL, MMM and CST for benchmarking purposes”, Contributed talk at BE-ABP Impedance meeting, February 2nd 2015, CERN, Geneva, Switzerland.
6. “Wake fields and impedances simulations of LHC collimators with GdfidL code”, Contributed talk at 4th HiLumiLHC-LARP Annual Meeting, November 19th 2014, KEK, Tsukuba, Japan.
7. “Wake fields and impedances simulations of LHC collimators with GdfidL code”, Contributed talk at 17th meeting HiLumi-LHC WP 2.4, October 29th 2014, CERN, Geneva, Switzerland.
8. “Test simulations of TT2-111R lossy dispersive material properties”, Contributed talk at 8th meeting HiLumi-LHC WP 2.4, March 26th 2014, CERN, Geneva, Switzerland.
9. “Geometric coupling impedance of LHC secondary collimators”, Contributed talk at Topical Workshop on Instabilities, Impedance and Collective Effects 2014 (TWIICE2014), January 16-17 2014, SOLEIL, France.

Posters

1. O. Frasciello *et al.*, “Geometric beam coupling impedance of LHC secondary collimators”, IPAC 2014, Dresden, Germany.
2. O. Frasciello *et al.*, “Beam coupling impedance of LHC secondary collimators”, X international scientific workshop to the memory of professor V.P. Sarantsev, Alushta, Ukraine.

Chapter 1

Introduction

1.1 The CERN Large Hadron Collider

The Large Hadron Collider (LHC) hosted at CERN, the European Organization for Nuclear Research in Geneva, Switzerland, is the world's largest particle accelerator. With a circumference of 27 km, it can bring into collisions proton beams at a centre of mass energy of 14 TeV. It is the last element of a more complex chain of accelerators (Fig. 4.4). Each machine of this chain injects the beam into the next

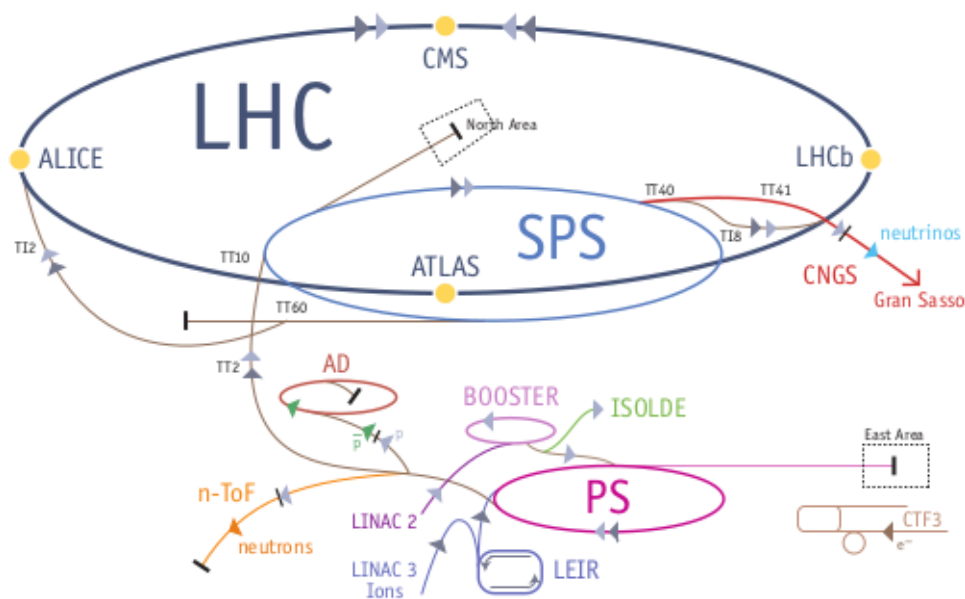


Figure 1.1. A sketch of the whole LHC accelerator complex, together with the main experiments and beam lines.

one at increasing energy. First, Hydrogen atoms are ionized by a Duoplasmatron Proton Source, stripping orbiting electrons and producing protons to be injected into Linac 2. Linac 2 accelerates protons up to the energy of 50 MeV, before they are transferred to the Proton Synchrotron Booster (PSB) which brings them to 1.4 GeV. Protons are again transferred in sequence to the Proton Synchrotron (PS) and

the Super Proton Synchrotron (SPS) where they reach energies of, respectively, 25 GeV and 450 GeV. At the end of the SPS stage, protons are ready to feed the LHC where they are accelerated to the final energy of 7 TeV. The SPS injects two bunched beams into the LHC, B1 and B2, via two transfer lines, TI2 and TI8, according to the filling schemes in Fig. 4.5[1].

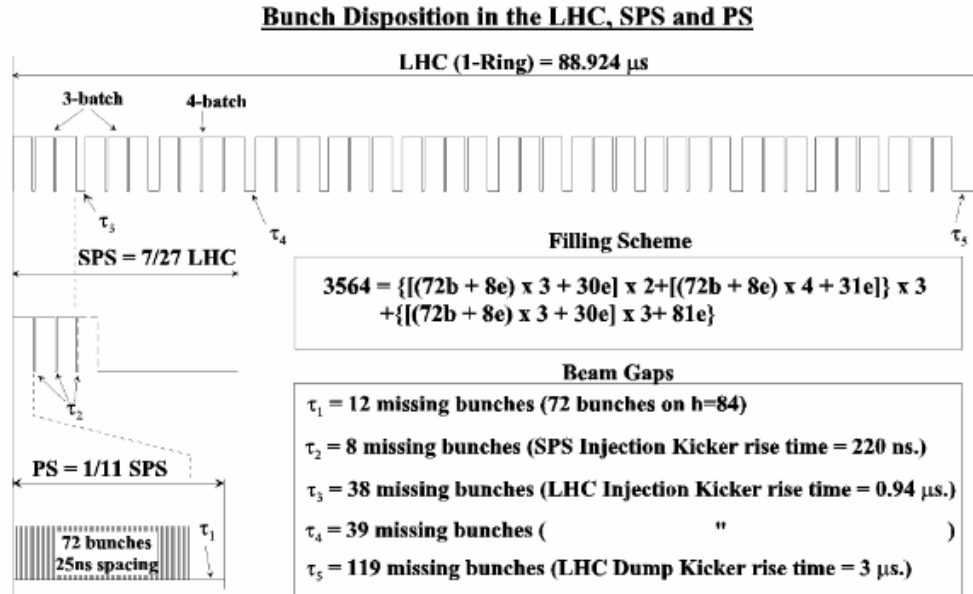
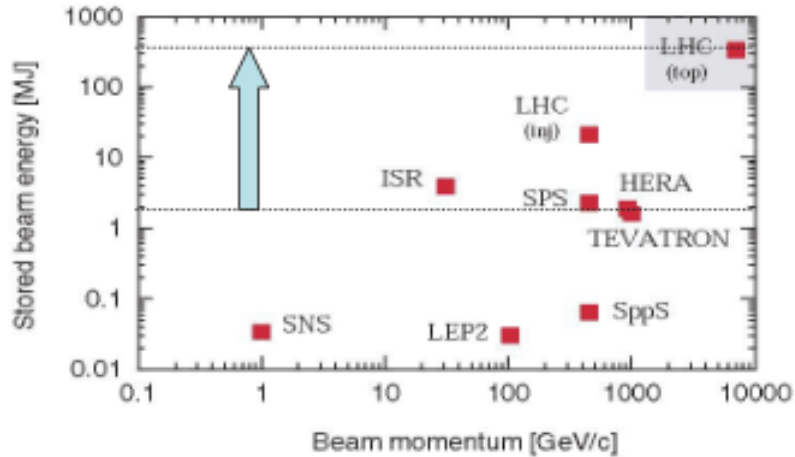


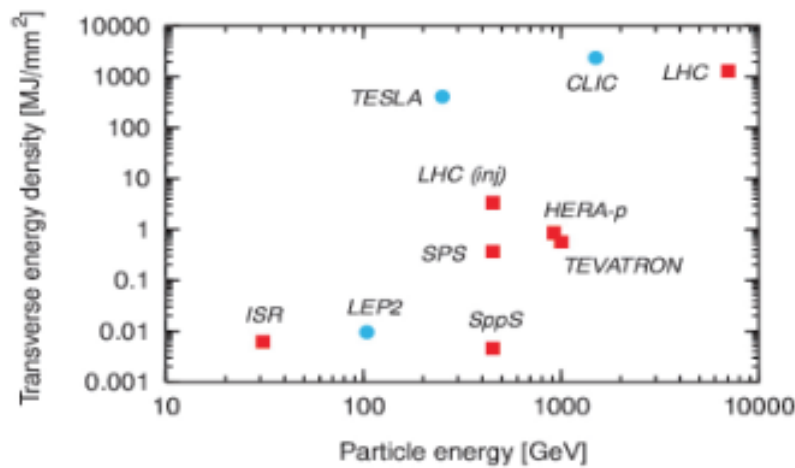
Figure 1.2. Bunches in the LHC, SPS and PS. PS batch consists of 72 bunches on $h = 84$ at extraction. Either three or four of these batches are sequentially transferred to the SPS, thereby partially filling 3/11 or 4/11 of the SPS circumference. For each LHC ring, 12 of these 216 or 288 bunch trains are transferred from SPS to LHC. With $9 \cdot 216 + 3 \cdot 288$ injections, the LHC is filled with 2808 bunches.

The accelerator complex can accelerate not only protons, but also Lead ions, produced heating to a temperature of about 500°C a highly purified lead sample, then ionizing the formed vapours by means of an electron current. The Pb^{29+} ions are accelerated to 4.2 MeV/u and brought to impinge on carbon foils to be stripped to Pb^{54+} . These latter ions constitutes the intermediate beam accumulated in the Low Energy Ion Ring (LEIR) and accelerated to 72 MeV/u before being injected into the PS, which lets the beam to reach the energy of 5.9 GeV/u. This is the energy at which the SPS is fed by the ion beam, finally stripped to Pb^{82+} and accelerated to 177 GeV/u before being finally transferred to the LHC, where Pb^{82+} ion beams will be accelerated at 2.76 TeV/u.

The nominal energy stored per beam in the LHC is about 362 MJ, what characterize the LHC as a record machine both from the stored energy and the energy density points of view (Fig. 1.3(a) and Fig. 1.3(b)) [2]. Such an extreme facility puts strong constraints on the reliability of the safety and the collimation systems. The former has the role of aborting the beams in a clean way in case of any dangerous condition; the latter one has to protect the machine and detectors from halo particles and other unavoidable losses, as will be further discussed in more detail in section 1.3.



(a)



(b)

Figure 1.3

A schematic layout of LHC is shown in Fig. 1.4. There are eight arcs housing 154 dipole bending magnets and eight straight sections housing LHC detectors in four of them and other machine utilities, such as radiofrequency, collimators and beam dumps in four others. The four detectors are:

- ALICE (A Large Ion Collider Experiment), which studies the properties of quark-gluon plasma;
- ATLAS (A Toroidal LHC ApparatuS), designed to study a wide range of Physics at LHC, from the search for Higgs Boson[3, 4] to supersymmetries (SUSY) and extra dimensions;
- CMS (Compact Muon Solenoid), aimed at the same Physics hunt as ATLAS but with different technical solutions;

- LHCb (LHC Beauty), designed to study asymmetries between matter and antimatter in B particles interactions.

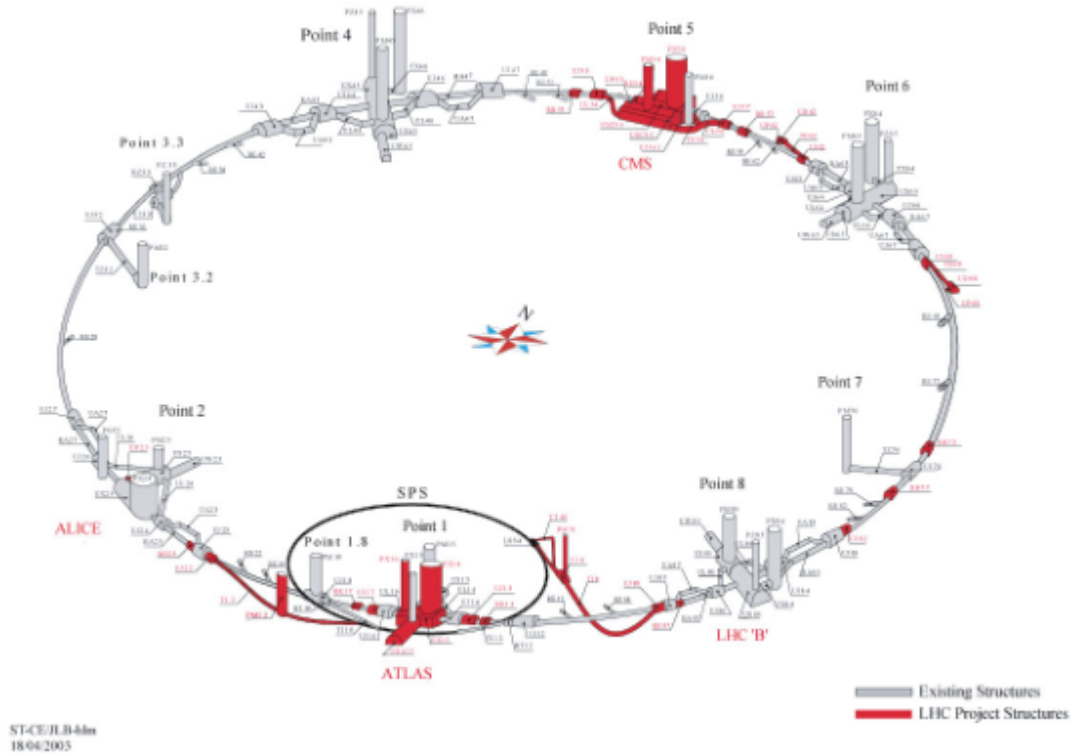


Figure 1.4

All the above mentioned detectors study very rare events. The number of events per second generated by beam-beam collisions for a given process is given by

$$N = L\sigma, \quad (1.1)$$

where L is the luminosity and σ the cross section for the process under study. The luminosity is a crucial figure of merit for a particle collider and for rare events the demand is for it to be as large as possible, $10^{34}\text{cm}^{-2}\text{s}^{-1}$ for LHC. Depending only on the beam parameters, the luminosity for a Gaussian beam profile can be written as

$$L = \frac{N_b^2 n f_r \gamma}{4\pi \epsilon_n \beta^*}, \quad (1.2)$$

where N_b is the number of particles per bunch, n the number of bunches per beam, f_r the revolution frequency, γ the relativistic Lorentz factor, ϵ_n the normalized transverse emittance and β^* the β function at collision points. The integrated luminosity performances over three years of operation, reported in Table 1.1, together with the machine operational parameters before LS I reported in Table 1.2[5], allowed ATLAS and CMS to discover the Higgs Boson¹ [7, 8, 9, 10].

¹ATLAS and CMS collaborations announced the Higgs boson discovery on July 4th, 2012 during a joint seminar at CERN. More recently, the LHCb experiment claimed for pentaquark discovery on July 14th, 2015[6].

Year	Overview	COM	Integrated Luminosity [fb^{-1}]
2010	Commissioning	7 TeV	0.04
2011	Exploring limits	7 TeV	6.1
2012	Performance	8 TeV	23.1

Table 1.1. LHC operations 2010-2012

Parameter	Value in 2012	Design value
Beam energy [TeV]	4	7
β^* in IP 1,2,5,8 [m]	0.6,3.0,0.6,3.0	0.55
Bunch spacing [ns]	50	25
Number of bunches	1374	2808
Average bunch intensity [p/bunch]	$1.6\text{-}1.7 \cdot 10^{11}$	$1.5 \cdot 10^{11}$
Normalized emittance at start of fill [mm mrad]	2.5	3.75
Peak luminosity [$\text{cm}^{-2}\text{s}^{-1}$]	$7.7 \cdot 10^{33}$	$1 \cdot 10^{34}$
Max. mean number of events per bunch crossing	≈ 40	19
Stored beam energy [MJ]	≈ 140	362

Table 1.2. Performance related parameter overview

1.2 The High Luminosity LHC project

The European strategy for particle physics has, as its highest priority, the full exploitation of the LHC discovery capabilities [11, 12]. In order to extend LHC potential, a substantial upgrade is needed to increase the luminosity beyond its design values, by a factor of 5 the instantaneous luminosity and by a factor of 10 its integrated one. According to the baseline programme until 2025 shown in Fig. 1.5, this upgrade is planned to take place in 2020s [13].



Figure 1.5. LHC baseline plan for the next decade. The red upper line shows collision energy while the green lower lines the integrated luminosity.

Several innovative technologies will support the reliability of the novel machine, High Luminosity LHC (HL-LHC hereinafter), such as 11-12 tesla Super Conducting (SC) magnets, ultra compact SC cavities for ultra precise phase control and beam

rotation, new collimation system and long high power SC links with zero energy dissipation. With the just started Run II phase after LS I², LHC is expected to reach the design parameters, entering in the 13-14 TeV regime at a peak luminosity of $10^{34} \text{ cm}^{-2}\text{s}^{-1}$, delivering an integrated luminosity to the installed experiments of about 40 fb^{-1} per year. The physical reason making the HL-LHC upgrade strictly necessary rely on the well assessed condition that running the machine at its full luminosity capabilities after 2020 will not lead to a significant statistical gain in experimental measurements [11].

The possible evolution of both peak and integrated luminosity in the next decade is shown in Fig. 1.6, whereas in Fig. 1.7 the same quantities evolution is forecast in the HL-LHC era.

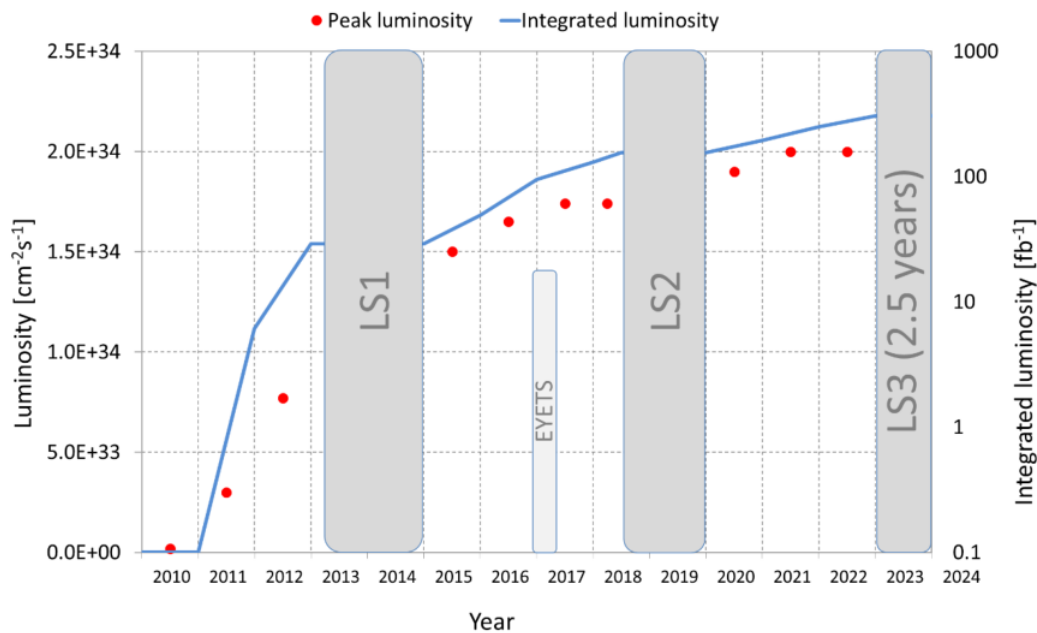


Figure 1.6. LHC luminosity evolution in the next decade, showing peak luminosity in red dots and integrated luminosity in blue line.

Several limitations for the luminosity increase are foreseen coming from the LHC injector chain, beam impedance and beam-beam interactions, apart from the present LHC being already affected by potential performance limitations from the beam current, cleaning efficiency with 350 MJ beam stored energy, e-cloud and other effects [14]. Among others, the collimation system will need changes and improvements in the new HL-LHC machine configuration, because of vulnerabilities that will arise as a consequence of the accelerator operations. It has been designed for the first operation phase of LHC and optimized for robustness, but the lower impedance required for the planned increase in beam intensity will lead to its significant upgrade.

²First Run II proton-proton collisions at 13 TeV center of mass energy took place already in May 2015.

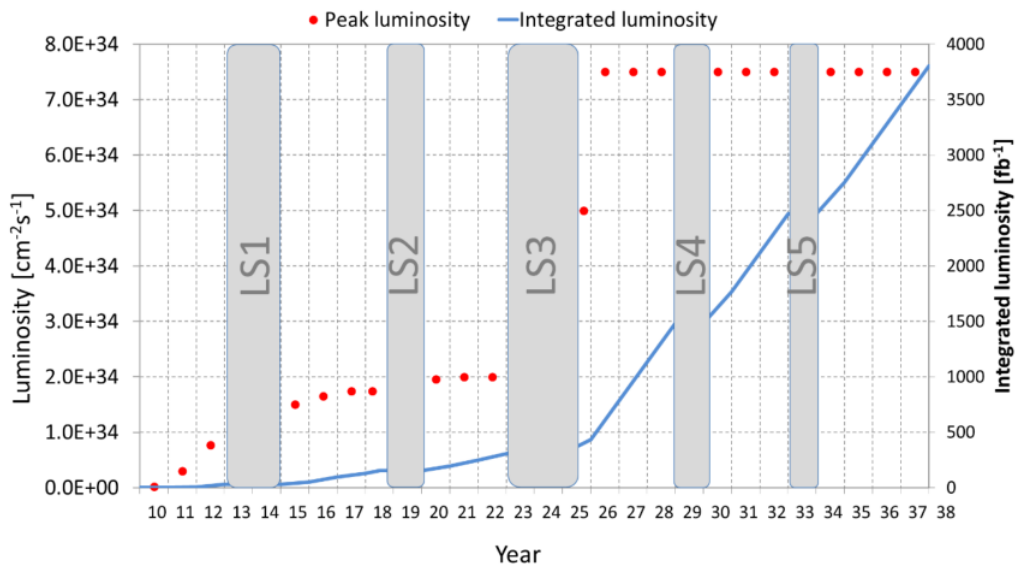


Figure 1.7. HL-LHC luminosity evolution, showing peak luminosity in red dots and integrated luminosity in blue line.

1.3 The LHC collimation system

Bunched³ particle beams are generally characterized by a Gaussian-like distribution of particles in the transverse plane. So within one standard deviation, 1σ , of the Gaussian beam $\sim 68\%$ of the particles are comprised. Looking at Fig. 1.8, the beam core is usually defined as $0 - 3\sigma$ (99.7% of all particles), while the region $> 3\sigma$ is recognized as the beam halo. For the LHC the beam profile is more parabolic-like than Gaussian-like. However no lack of validity is found in what follows, if a Gaussian-like distribution is assumed.

Partial or total beam losses are unavoidable in particle accelerators. There are several effects leading to beam losses, such as collisions in interaction points, interactions with residual gas in vacuum systems and intra-beam scattering, beam instabilities (single bunch, multi-bunch, beam-beam effects), dynamic changes driven by machine operational cycle (orbit drifts, optics changes), RF noises and out-of-bucket losses, injection and dump losses. All these effects can increase the beam halo population and ultimately cause beam losses. Their mechanisms are characterized by a time-dependent beam lifetime during the machine cycle, τ_b , where the beam intensity time dependence is given by

$$I(t) = I_0 \cdot e^{-\frac{t}{\tau_b}}, \quad (1.3)$$

and the particle loss rate by

$$-\frac{1}{I_0} \frac{dI}{dt} = \frac{1}{\tau_b}. \quad (1.4)$$

As an example, with $\tau_b = 1\text{ h}$ and $I_0 = 3.2 \cdot 10^{14}\text{ p}$, the total loss per second would be $90 \cdot 10^9\text{ p/s}$, or $0.1\text{ MJ/s} = 100\text{ kW}$. Again, at 7 TeV only 1% of total beam intensity

³Bunched beams are formed by “packets” or pulses of particles named bunches. On the contrary “coasted” or unbunched beams have no longitudinal substructure.

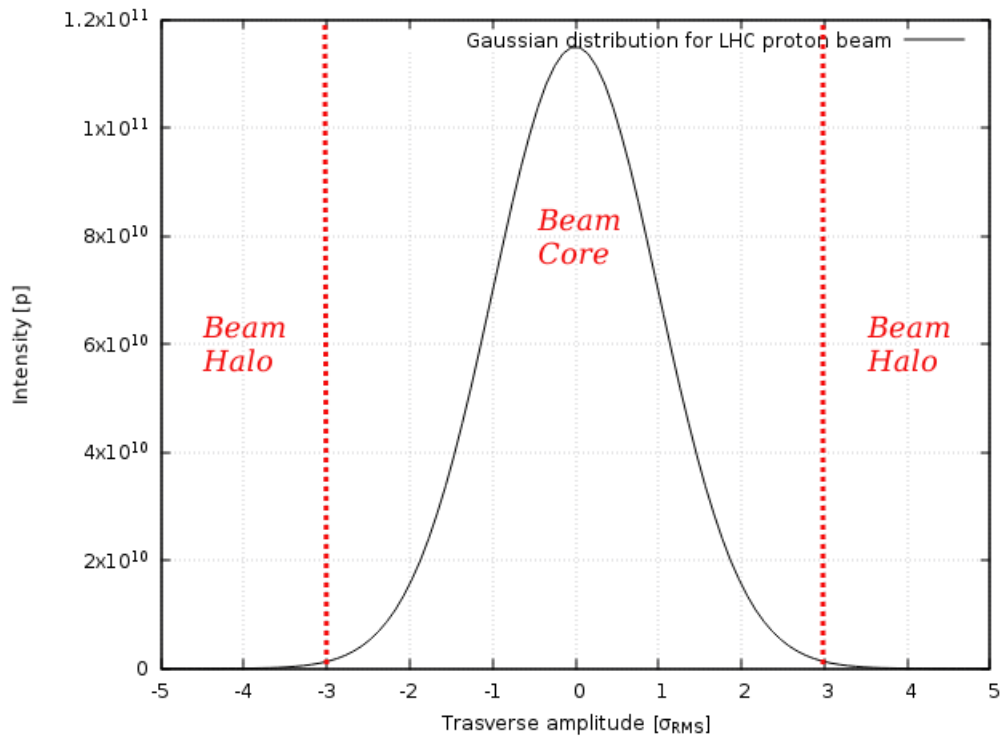


Figure 1.8. Core and halo definition for a particle beam with Gaussian transverse particle distribution.

loss in a period of 10 s, would produce a peak load of 500 kW, whereas the upper limit to SC magnets energy deposition, without quench, is ~ 8.5 W/m.

Collimation system has been designed to accomplish several tasks, such as SC magnets protection against quenching, beam halo cleaning throughout the LHC beam cycle (reaching an efficiency of 99.998%), its diagnostic and scraping, machine aperture passive protection against radiation and hardware protection against radiation hardness [15, 16, 17]. For the collimation system to be successful in all the assigned tasks means to be subtended to the condition that all losses occur at collimators, and not elsewhere in the machine. This entails all particles' oscillations growing to large amplitudes having to be intercepted by the collimators, thus protecting the machine. Collimators are placed around the beam with various settings of longitudinal position orientation in the H-V transverse planes and transverse distances from the beam.

Fig. 1.9 shows the collimators' layout in the LHC machine, with the three stage collimation system installed in the dedicated cleaning insertions IP3 and IP7, to ensure that only a small fraction of lost protons escapes from there, while in Fig. 1.10 the LHC collimation hierarchy is depicted, with collimators disposition with respect to the beam core depending upon material robustness. Generally low Z materials, like Carbon Fiber Composite (CFC), ensure for higher robustness at the expenses of absorption power.

The collimators' design relies on two parallel jaws that define a slit for the beam passage (Fig. 1.11(a)) [19]. The collimator whole box (Fig. 1.11(b)) can be rotated

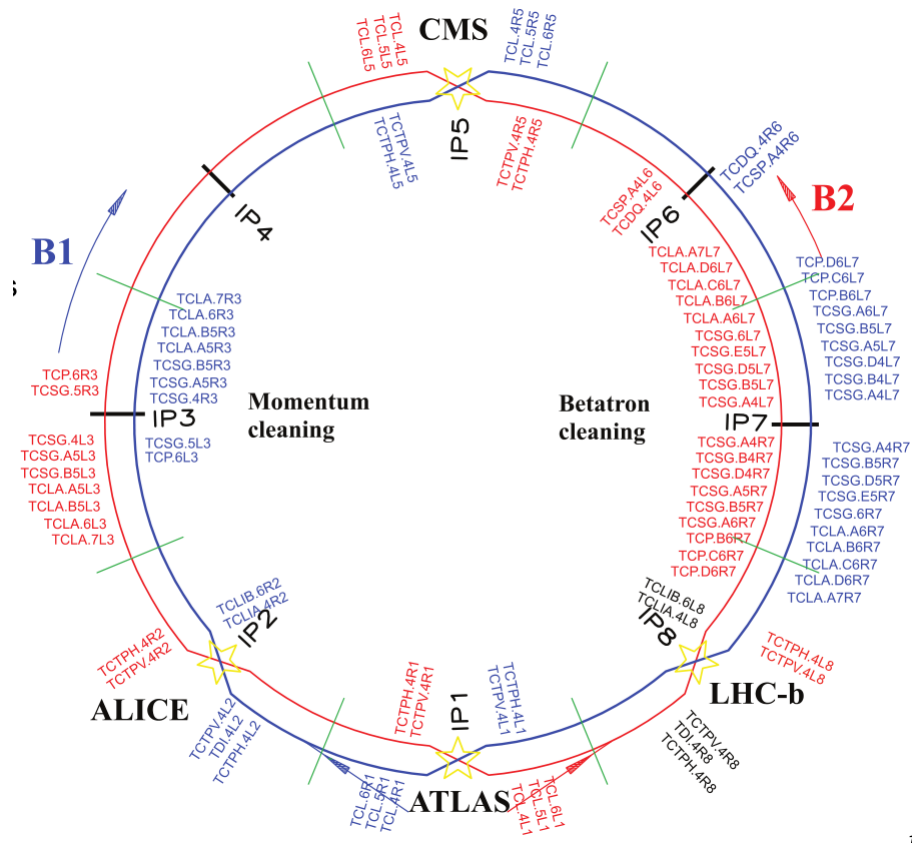


Figure 1.9. The LHC collimations system layout. Two three-stages cleaning insertions are installed in IP3 and IP7. Other absorber collimators are distributed along the machine. Injection collimators are also shown near IP2 and IP8.

in the H-V plane to collimate horizontal, vertical or skew halo, as shown in Fig. 1.12(a), 1.12(b) and 1.12(c).

The collimation hierarchy is composed of:

- Primary collimators (TCP) with Carbon Fiber Composite (CFC) jaws;
- Secondary collimators (TCS) made again of CFC jaws;
- Tertiary collimators absorbers with Tungsten (W) or Copper (Cu) made jaws.

Among others, injection collimators (TDI) are noteworthy also, with important role in beam cleaning at the exit of SPS and local protection against injection failures. Table 1.3 summarizes some TCP and TCS collimators specifications, while in Table 1.4 the main specifications for other LHC ring collimators are listed.

TCP collimators intercept stray particles of the primary halo for horizontal, vertical, skew or momentum offsets, spraying losses downstream. Further losses of secondary halo particles interception and dilutions happen at TCS collimators. At the end of the warm cleaning insertions, less robust high Z (W, Cu) jaws collimators absorb the diluted proton halo and showers. After this three-stage cleaning process,

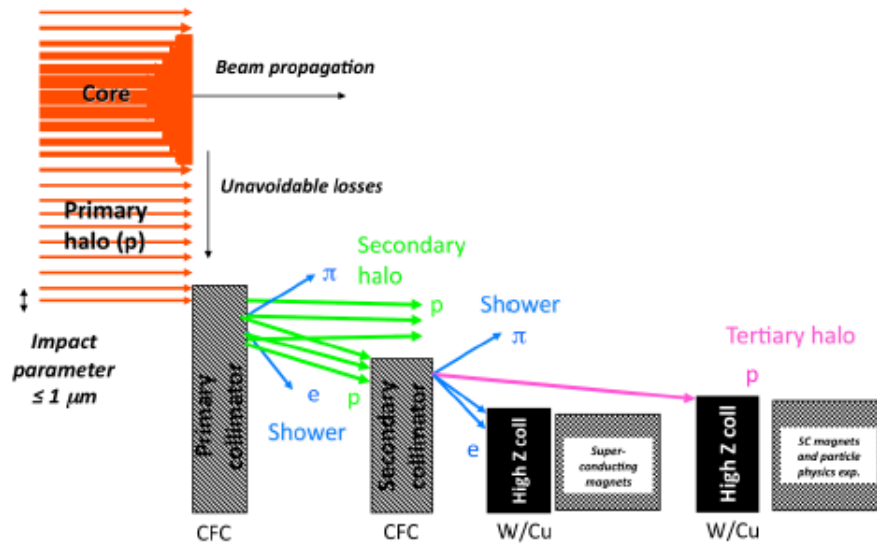


Figure 1.10. LHC collimation hierarchy. Collimators are disposed in order to protect the machine against primary, secondary and tertiary radiation fields and hadronic showers produced by the interaction of the primary proton beam halo [18].

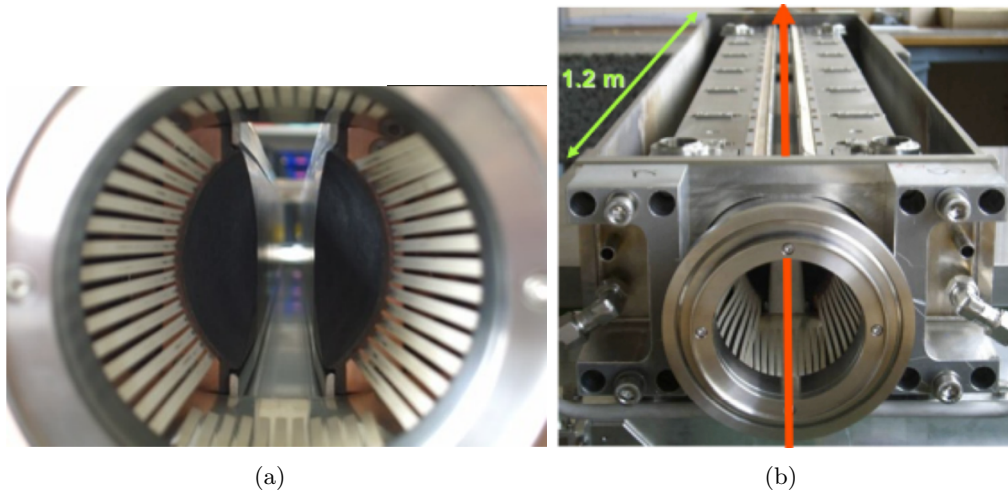


Figure 1.11. Photograph of a TCP/TCS LHC Run I type collimator along the beam path (a) and of a TCP/TCS LHC Run I type collimator box during assembling (b).

finally, a fourth stage takes place again with high Z jaws collimators, having to intercept tertiary halo close to the particle physics experiments and triplet magnets.

The LHC collimation design has taken into account many requirements, one being the coupling impedance whose transverse and longitudinal component depends strongly on collimator settings, both at injection and at top energy, given the collimation gaps going down to 2.5 mm and a total installed collimators' jaw length of about 48 m per beam [20, 21]. The LHC performance relies upon beam cleaning efficiency and coupling impedance, both potentially constituting a limitation in the maximum achievable beam intensity.

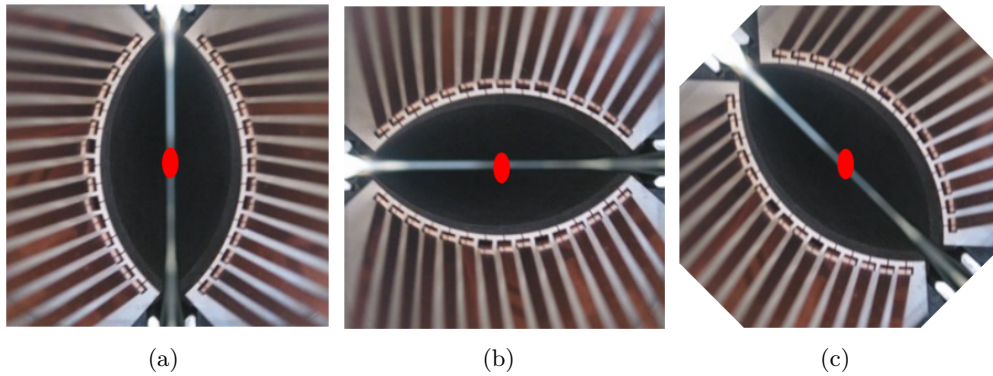


Figure 1.12. Collimators orientation in horizontal (a), vertical (b) and skew (c) planes, with the beam sketched as a red spot.

Parameter	TCP	TCS
Jaw material	CFC	CFC
Jaw length [cm]	60	100
Jaw tapering [cm]	10 + 10	10 + 10
Jaw cross section [mm ²]	65 · 25	65 · 25
Jaw resistivity [$\mu\Omega$ m]	≤ 10	≤ 10
Heat load [kW]	≤ 7	≤ 7
Jaw temperature [°C]	≤ 50	≤ 50
Residual vacuum pressure [mbar]	$\leq 4 \cdot 10^{-8}$	$\leq 4 \cdot 10^{-8}$
Minimal gap [mm]	≤ 0.5	≤ 0.5
Maximal gap [mm]	≥ 58	≥ 58
Maximumm Jaw angle [mrad]	2	2

Table 1.3. Some specifications for TCP and TCS collimators.

Parameter	TCT	TCLA	TCL	TCLP	TCLI
Jaw material	W	W	Cu	Cu	CFC
Jaw length [cm]	100	100	100	100	100
Jaw tapering [cm]	10+10	10+10	10+10	10+10	10+10
Minimal gap [mm]	≤ 0.8	≤ 0.8	≤ 0.8	≤ 0.8	≤ 0.5

Table 1.4. Some specifications for other LHC ring collimators.

In the next chapter the concepts of wake fields and beam coupling impedances will be exploited. Their influence on particle beam dynamics by means of induced beam instabilities will be addressed also. Comprehensive and fully exhaustive treatments of collective beam instabilities exist elsewhere and are referred to [22, 23] throughout this thesis but are not its main subject, so that the discussion will be focused only on those type of instabilities of concern for the study conducted on LHC collimators.

Chapter 2

Wake fields and beam coupling impedances

2.1 Where do Wake fields originate from

The motion of charged particles in the electromagnetic fields (\vec{E}, \vec{B}) is governed by the Lorentz force \vec{F} [24]:

$$m_0\gamma\frac{d\vec{v}}{dt} = \vec{F} = q(\vec{E} + \vec{v} \times \vec{B}), \quad (2.1)$$

γ being the Lorentz energy factor $\gamma = 1/\sqrt{1 - \beta^2}$, $\beta = v/c$. The design of an accelerator relies on the consideration of the motion of a single charged particle in the environment of magnets and RF cavities, which must be stable (i.e. the particle and the beam lifetime must be long enough to allow sufficient luminosity to the installed physics experiments). So that, in what is usually called the *linear lattice* design for a circular machine, three basic elements are addressed:

- the *Dipoles* which guides the particle trajectory via the magnetic field, weakly focusing in the transverse horizontal x direction;
- the *Quadrupoles* which confines the particle motion near the design trajectory via the magnetic field, focusing in the transverse x and y directions;
- the *Sextupoles* and higher order multipole magnets for the control of chromatic and geometric aberrations;
- the *RF cavities* which keep the particle energy near the design energy via the electric field, thus focusing in the longitudinal z direction.

A charged particle moving on a circular orbit is sketched in Fig. 2.1, in which the three directions x , y and z above referred to are specified.

There are, however, additional electromagnetic fields coming from the interaction of the charged beam particle (here called *source*) with its vacuum chamber environment in the accelerator. The interaction takes place owing to the Gauss's law, which for a charge in free space reads

$$\vec{\nabla} \cdot \vec{E} = \frac{\rho}{\epsilon_0}, \quad (2.2)$$

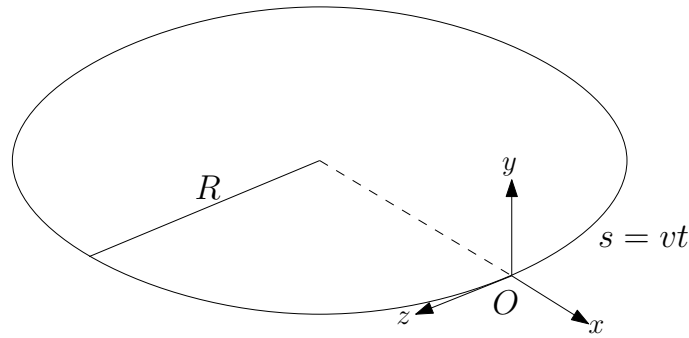


Figure 2.1. A simple sketch of a reference charged particle moving on a circular orbit, specifying the reference coordinate system.

where ρ is the charge density at the point where the field is \vec{E} and ϵ_0 is the electric permittivity of free space, equal to 8.854×10^{-12} F/m, in the SI system of units. Its physical meaning is that electric field lines are absolutely attached to the charges, they can be distorted but never cut away from the charges under any circumstances. If the charge is in free space and stationary, its electric field lines radiate outwards isotropically, as in Fig. 2.2(a). As a result of the theory of relativity, if the charge moves relativistically with velocity $v \approx c$, $c = 2.997925 \times 10^8$ m/s being the velocity of light, electric field lines get contracted into a thin disk, usually called “pancake”, perpendicular to the particle’s direction of motion with an angular spread of $\frac{1}{\gamma}$, as in Fig. 2.2(b). When the charge moves in the ultrarelativistic limit $v = c$, then the pancake reduces to δ -function thin sheet, as shown in Fig. 2.2(c)[22].

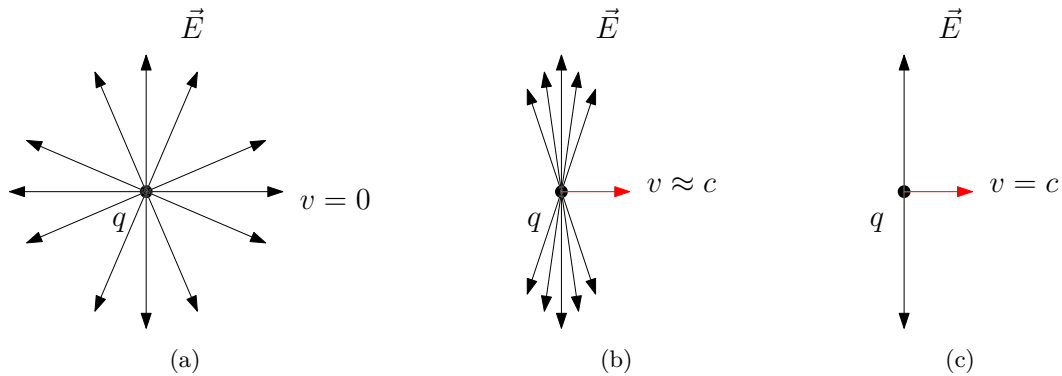


Figure 2.2. Electric field lines for a charge in free space a) stationary, b) moving relativistically and c) in the ultrarelativistic limit.

Magnetic field is also generated by a moving charge, with the same distribution as the electric field but with different properties. It also get contracted into a pancake-like thin disk as v approaches c , but its direction is azimuthal instead of radial as the electric field direction. Choosing a cylindrical coordinate system to describe the particle motion in free space, (r, θ, s) , in which s is the absolute longitudinal position in the laboratory frame, thus pointing in the direction of motion of the charge q , the application of the Gauss’s law 2.2 for the electric field and of the Ampere’s law

for the magnetic field

$$\vec{\nabla} \times \vec{B} = \mu_0 \vec{j} + \frac{1}{c^2} \frac{\partial \vec{E}}{\partial t}, \quad (2.3)$$

where μ_0 is the magnetic permeability of vacuum equal to $4\pi \times 10^{-7}$ H/m in the SI system of units and \vec{j} is the current density vector, the following relations for electric and magnetic fields can be obtained for the moving charge considered:

$$E_r = \frac{2q}{r} \delta(s - ct) \quad (2.4)$$

$$B_\theta = \frac{2q}{r} \delta(s - ct). \quad (2.5)$$

The situation in which a particle moves in the vacuum chamber of an accelerator deserves a bit more of discussion. Let the particle move along the axis of an axially symmetric perfectly conducting vacuum chamber pipe, as shown in Fig. 2.3. Let

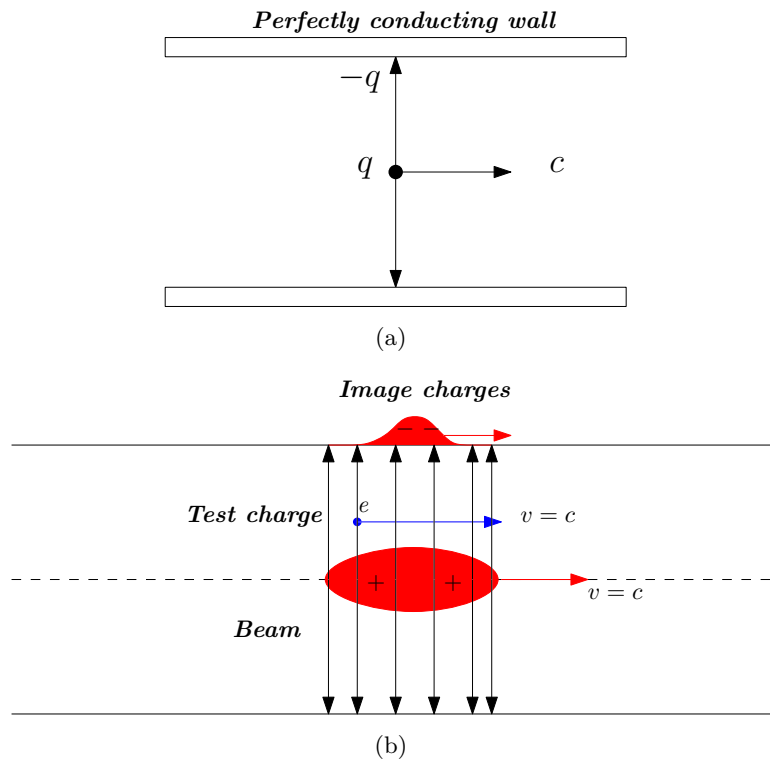


Figure 2.3. Particle a) and beam b) moving on axis in a perfectly conducting wall vacuum chamber. Image charges are shown on the wall.

the pipe be smooth¹. The solution again of the Gauss's and Ampere's laws leads to the same equations 2.2 and 2.3, but with the field lines perfectly terminating on the pipe wall (Fig. 2.3(b)). The image charges on the wall is exactly equal and opposite to that of the particle (or the beam), moving with the same velocity $v = c$ in the same direction. The entire field pattern moves with it and no field are left behind. Both in free space or in perfectly conducting pipe, the dependence of 2.4 on

¹This means that it has no discontinuities.

$\delta(s - ct)$ makes the ultrarelativistic particle not to feel any effect from the fields carried by other particles in the beam. This is unless any two particles move side by side exactly at the same longitudinal position, in which case however electric and magnetic fields cancel exactly thus producing no Lorentz force on the particles. To illustrate the above statement, consider the “test charge” depicted in Fig. 2.3(b), which moves with the beam and has the same charge sign, $v = c$. This particle will experience two forces, the electrical $\vec{F}_E = e \cdot \vec{E}$ due to the electric field of the beam, directed radially, and the magnetic $\vec{F}_B = e(\vec{v} \times \vec{B})/c$ directed along the azimuthal direction, by means of the right hand rule. \vec{F}_E will push the charge e towards the pipe wall whereas \vec{F}_B will point towards the pipe axis, but in the ultrarelativistic limit $|\vec{E}| = |\vec{B}|$ and the two forces cancel exactly. As a consequence, it can be stated that if the beam is ultrarelativistic, the vacuum chamber is smooth and perfectly conducting, no collective instabilities can occur.

When there is a discontinuity in the conducting vacuum chamber, the image charges moving along the pipe have now to move around a corner. It is a well established result of the electromagnetic theory that when a charge is bent it radiates. Thus additional electromagnetic fields are generated as the radiation fields of the image charges when their trajectory is bent. Because of causality, such fields exist *behind* the particle and thus are called *wake fields*. This physical mechanism is illustrated in Fig. 2.4 and Fig. 2.5.

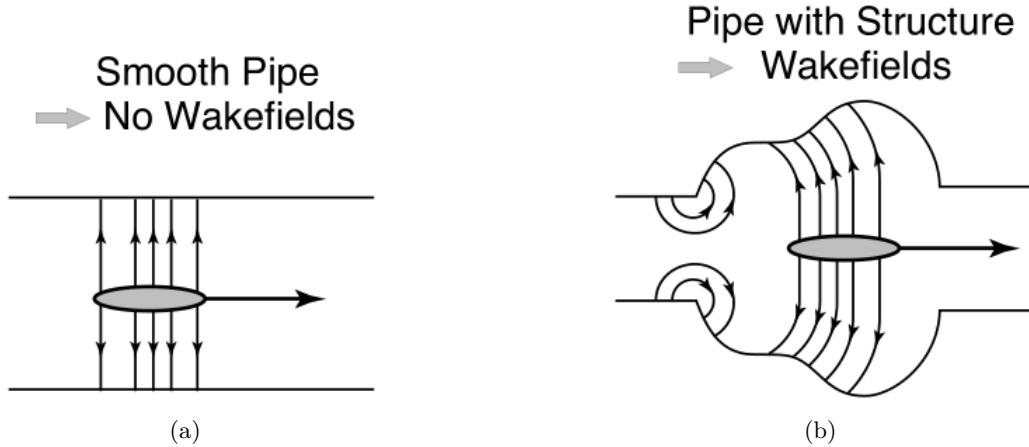


Figure 2.4. Charged beam passing through a) a smooth pipe and through b) a pipe with discontinuous structure [22]. Only in the latter case wake fields are generated, as specified in Fig. 2.5.

An intense beam will generate a strong wakefield and the stronger the wakefield the more the beam can become unstable. Wakefields will perturb the motion of the following particles, called *witness*. This way a particle can experience an “effective” electromagnetic field given by the sum of the one produced by the external lattice elements of the accelerator, and the other being the wakes produced by the particles in front interacting with the vacuum chamber, so that [23]:

$$(\vec{E}, \vec{B})_{effective} = (\vec{E}, \vec{B})_{external} + (\vec{E}, \vec{B})_{wakes}.$$

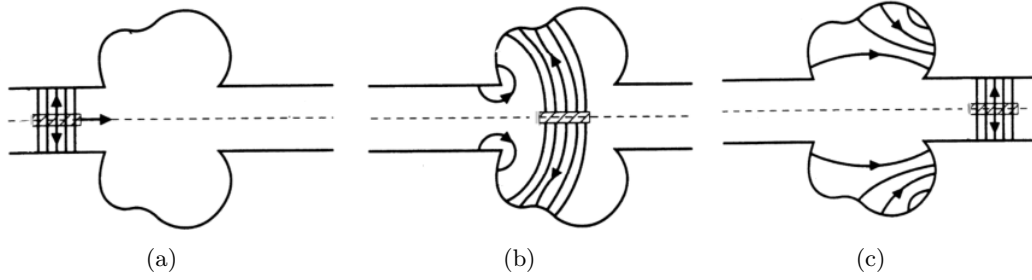


Figure 2.5. Wake fields generated as the the beam passes along the axis of a discontinuous vacuum chamber. In the smooth region in a) no wake fields generate; they start to propagate as soon as the beam approaches the discontinuity in b) and continue propagate inside the structure when the beam as passed away in c) [22].

The two fields summed on the right hand side (RHS) of the equation differs in $(\vec{E}, \vec{B})_{external}$ being beam intensity independent, while $(\vec{E}, \vec{B})_{wakes}$ being proportional to beam intensity. The wakes' influence on the beam can be treated as a perturbation if the condition $(\vec{E}, \vec{B})_{wakes} \ll (\vec{E}, \vec{B})_{external}$ is satisfied. The wake fields generated in the case of perfectly conducting vacuum chamber walls, due to its geometrical discontinuities only, are referred to as “geometric wake fields” [25].

If the vacuum chamber wall is still smooth but has finite constant electric conductivity σ (i.e. it is resistive), the so called “resistive wall” (RW) wake fields are generated. To understand the physical mechanism a brief recall of the main results of Maxwell equations is needed, as illustrated in Fig. 2.6. Electric and magnetic fields

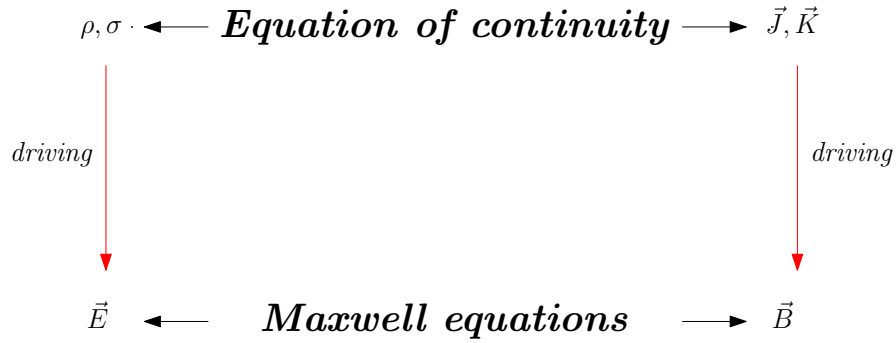


Figure 2.6. A logical sketch of the physical content of Maxwell equations. By definition, metals have $\rho = 0$ and $\vec{J} = \sigma \vec{E}$, whereas insulators have $\vec{J} = 0$ and $\rho = \epsilon \vec{\nabla} \cdot \vec{E}$.

are driven by, respectively, charges and currents. The interplay between electric and magnetic fields is governed by Maxwell equations, while that of charge and current by the equation of continuity. In the case of metals, charges stay on the surface and are not allowed inside, while currents stay near the surface and do penetrate into the conductor. The parameter quantifying how much they do penetrate is the skin depth

$$\delta_{skin} = \frac{c}{\sqrt{2\pi\sigma|\omega|}}, \quad (2.6)$$

where σ is the finite conductivity of the metal and ω the frequency of the electromagnetic field. For insulators, instead, no currents but charges are allowed to stay inside. Thus the physical mechanism giving rise to RW wake fields lies on electric field lines being terminated by a surface charge on the wall surface and on the magnetic field being cancelled by a surface current, when the beam's image charges flow on the vacuum chamber wall. While electric field is terminated by surface currents, magnetic field is “mostly” cancelled, because currents have penetrated the wall by a skin depth. The image currents can re-surface from the chamber wall after the point charge has past and drive new magnetic fields that in turn drive new electric fields by Maxwell equations. In the case of RW wake fields, they are mainly magnetic fields contributing to transverse wake force, while the associated electric field contributes to longitudinal wake force.

The qualitative discussion on the origin of wake fields will be exploited in mathematical detail in the next section, where the concept of beam coupling impedance will arise. This will allow to gain useful informations on the beam dynamics in presence of wake fields and to analyze the beam dynamics subtended to those collective instabilities the work described in the next chapters will concern with.

2.2 Panofsky-Wenzel theorem and Wake functions

2.2.1 Basic approximations

Two basic approximations are introduced in order to simplify the mathematical description of wake functions, the rigid bunch and the impulse approximations [22].

In the rigid bunch approximation, the beam traversing through the vacuum chamber is assumed to be not affected by its discontinuities. Looking at Fig. 2.7, s is the distance of the source particle along the vacuum chamber axis, from an arbitrary reference point. Let the source particle be at $s = \beta ct$ and the following (here called *witness*) particle at $s = z + \beta ct$, with $z < 0$ to indicate that the witness stays behind the source. Being the bunch *rigid*, both z and βc do not change after traversing the discontinuity, even if synchrotron motion is still allowed.

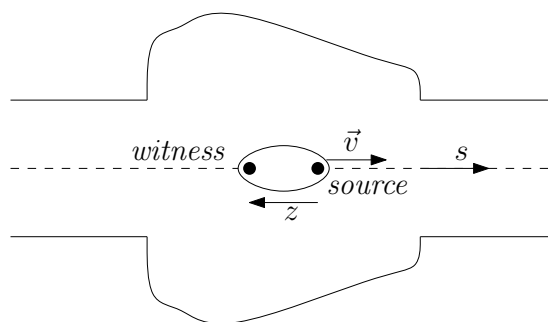


Figure 2.7. The rigid bunch approximation. Both distance between source and witness particles, z , and particles velocity, βc , do not change during vacuum chamber discontinuities traversal.

Let q be the witness particle charge. The impulse approximation relies on nothing of the single \vec{E} or \vec{B} components of the wake field or wake force \vec{F} in themselves

being considered, but only the change in impulse of the witness particle

$$\Delta\vec{p} = \int_{-\infty}^{\infty} \vec{F} dt = \int_{-\infty}^{\infty} q(\vec{E} + \vec{v} \times \vec{B}) dt. \quad (2.7)$$

2.2.2 The Panofsky-Wenzel theorem

Let the Maxwell equations be rewritten for the witness particle at (x, y, s, t) , with z constant and $s = z + \beta ct$,

$$\vec{\nabla} \cdot \vec{E} = \frac{\rho}{\epsilon_0} \quad (2.8)$$

$$\vec{\nabla} \times \vec{B} = \mu_0 \beta c \rho \hat{s} \quad (2.9)$$

$$\vec{\nabla} \cdot \vec{B} = 0 \quad (2.10)$$

$$\vec{\nabla} \times \vec{E} = -\frac{\partial \vec{B}}{\partial t}, \quad (2.11)$$

where \hat{s} is the unit vector of the s direction.

Given the Lorentz force definition in eq. 2.1, the Panofsky-Wenzel theorem arise quite naturally from eqs. 2.8- 2.11 written for the change in impulse $\Delta\vec{p}(x, y, z, t)$. For instance, the calculation of the divergence and curl of Lorentz force leads to:

$$\begin{aligned} \vec{\nabla} \cdot \vec{F} &= q(\vec{\nabla} \cdot \vec{E} + \vec{\nabla} \cdot \vec{v} \times \vec{B}) = \\ &= \frac{q\rho}{\epsilon_0} - q\vec{v} \cdot \left(\frac{1}{c^2} \frac{\partial \vec{E}}{\partial t} + \mu_0 \beta c \rho \hat{s} \right) = \frac{q\rho}{\epsilon_0 \gamma^2} - \frac{q\beta}{c} \frac{\partial E_s}{\partial t}, \end{aligned} \quad (2.12)$$

and

$$\begin{aligned} \vec{\nabla} \times \vec{F} &= q\vec{\nabla} \times \vec{E} + q\vec{\nabla} \times (\vec{v} \times \vec{B}) = \\ &= -q \frac{\partial \vec{B}}{\partial t} + q\vec{v}(\vec{\nabla} \cdot \vec{B}) - qv \frac{\partial \vec{B}}{\partial s} = q \left(\frac{\partial}{\partial t} + v \frac{\partial}{\partial s} \right) \vec{B} = q \frac{d\vec{B}}{dt}. \end{aligned} \quad (2.13)$$

For the curl of the impulse

$$\vec{\nabla} \times \Delta\vec{p}(x, y, z) = \int_{-\infty}^{\infty} [\vec{\nabla} \times \vec{F}(x, y, s, t)]_{s=z+\beta ct}, \quad (2.14)$$

where the first $\vec{\nabla}$ operator on the left hand side acts on (x, y, z) coordinates, while on the second right hand side acts on (x, y, s) coordinates, the eqs. 2.12 and 2.13 give:

$$\begin{aligned} \vec{\nabla} \times \Delta\vec{p} &= -q \int_{-\infty}^{\infty} \left[\left(\frac{\partial}{\partial t} + \beta c \frac{\partial}{\partial s} \right) \vec{B}(x, y, s, t) \right]_{s=z+\beta ct} dt = \\ &= -q \int_{-\infty}^{\infty} \frac{d\vec{B}}{dt} dt = -q \vec{B}(x, y, z + \beta ct, t) \Big|_{t=-\infty}^{\infty} = 0. \end{aligned} \quad (2.15)$$

Taking the dot and cross product of $\vec{\nabla} \times \Delta\vec{p}$ with \hat{s} returns into the following relations:

$$\begin{aligned}\hat{s} \cdot (\vec{\nabla} \times \vec{p}) &= 0 \\ \frac{\partial \Delta p_x}{\partial y} &= \frac{\partial \Delta p_y}{\partial x}\end{aligned}\quad (2.16)$$

$$\begin{aligned}\hat{s} \times (\vec{\nabla} \times \vec{p}) &= 0 \\ \frac{\partial \Delta \vec{p}_\perp}{\partial z} &= \vec{\nabla}_\perp \Delta p_s,\end{aligned}\quad (2.17)$$

the last one being recognized as the Panofsky-Wenzel theorem, which gives strong restrictions on longitudinal and transverse motions and does not depend on any boundary condition.

2.2.3 Decomposition into modes and Wake functions definition

In order to further break down the complicated wake fields, the problem of a vacuum chamber with cylindrical symmetry is analyzed. This allows some simplifications, but also to gain very general results useful to analyze wake fields in any structure, no matter of their shape. Inside such a beam pipe, all the above quantities can be expanded in Fourier series of $\cos(m\theta)$ and $\sin(m\theta)$, where θ is the azimuthal coordinate and m a non-negative integer. Writing

$$\begin{aligned}\Delta p_s &= \Delta \vec{p}_s \cos(m\theta) \\ \Delta p_r &= \Delta \vec{p}_r \cos(m\theta) \\ \Delta p_\theta &= \Delta \vec{p}_\theta \cos(m\theta),\end{aligned}$$

\vec{p}_s , \vec{p}_r and \vec{p}_θ being θ -independent, and taking $\beta = 1$, the components of $\Delta\vec{p}$ curl and divergence become:

$$\begin{aligned}\frac{\partial}{\partial r}(r\Delta p_\theta) &= \frac{\partial \Delta p_r}{\partial \theta} \\ \frac{\partial \Delta p_r}{\partial z} &= \frac{\partial \Delta p_s}{\partial r} \\ \frac{\partial \Delta p_\theta}{\partial z} &= \frac{1}{r} \frac{\partial \Delta p_s}{\partial \theta} \\ \frac{\partial}{\partial r}(r\Delta p_r) &= -\frac{\partial \Delta p_\theta}{\partial \theta},\end{aligned}$$

thus

$$\frac{\partial}{\partial r}(r\Delta \vec{p}_\theta) = -m\Delta \vec{p}_r \quad (2.18)$$

$$\frac{\partial \Delta \vec{p}_r}{\partial z} = \frac{\partial \Delta \vec{p}_s}{\partial r} \quad (2.19)$$

$$\frac{\partial \Delta \vec{p}_\theta}{\partial z} = -\frac{m}{r} \Delta \vec{p}_s \quad (2.20)$$

$$\frac{\partial}{\partial r}(r\Delta \vec{p}_r) = -m\Delta \vec{p}_\theta. \quad (2.21)$$

The components $\Delta\vec{p}_r$ and $\Delta\vec{p}_\theta$ are equal to zero for $m = 0$, while the the only non zero component is $\Delta\vec{p}_s$. For $m \neq 0$ $\Delta\vec{p}_r$ and $\Delta\vec{p}_\theta$ are proportional to r^{-1} and

$$\frac{\partial}{\partial r} \left[r \frac{\partial}{\partial r} (r \Delta\vec{p}_r) \right] = m^2 \Delta\vec{p}_r, \quad (2.22)$$

which implies

$$\Delta p_r(r, \theta, z) \sim m r^{m-1} \cos(m\theta). \quad (2.23)$$

Thus the Maxwell equations' solutions, for the change in impulse of the witness particle inside a cylindrical symmetric vacuum chamber, can get the following forms

$$v \Delta\vec{p}_\perp = -q Q_m W_m(z) m r^{m-1} (\hat{r} \cos(m\theta) - \hat{\theta} \sin(m\theta)), \quad \forall m \quad (2.24)$$

$$v \Delta p_s = -q Q_m W'_m(z) m \cos(m\theta), \quad \forall m \quad (2.25)$$

in which $W_m(z)$ and $W'_m(z)$ are, respectively, the transverse and longitudinal wake function of the azimuthal number m . They depend on the longitudinal distance between the source and the witness particle only, z , and not on the azimuthal angle θ , and are related to each other by means of the Panofsky-Wenzel theorem. Owing to this latter and to the rigid bunch and impulse approximations, the solution of the electromagnetic wake fields \vec{E} and \vec{B} are now reduced to the solution of the wake function $W_m(z)$ only. The negative sign in front of eq. 2.24 means that the witness particle loses energy from the impulse, so as $W'_m(z) > 0$.

Eq. 2.24 stands for the change in impulse of a witness particle of charge q , due to a source particle of charge e , at a deviation a from the axis of a cylindrical symmetric vacuum chamber. $Q_m = ea^m$ is the m multiple of the source particle and $v \Delta\vec{p}$ has the dimension of energy, so $W_m(z)$ has dimension of $V/C/m^{2m-1}$. The wake fields can be decomposed into transverse modes, according to the following table: In a cylindrical vacuum chamber, the m -th mode wake field can be driven

m	mode	Longitudinal Wakes	Moments of the driving beam
0	monopole	$-eqW'_0(z)$	q
1	dipole	$-eq \langle x \rangle xW'_1(z)$	$q \langle x \rangle$
	dipole	$-eq \langle y \rangle yW'_1(z)$	$q \langle y \rangle$
2	quadrupole	$-eq \langle x^2 - y^2 \rangle (x^2 - y^2)W'_2(z)$	$q \langle x^2 - y^2 \rangle$
	skew quadrupole	$-eq \langle 2xy \rangle (2xy)W'_2(z)$	$q \langle 2xy \rangle$
3	sextupole	$-eq \langle x^3 - 3xy^2 \rangle (x^3 - 3xy^2)W'_3(z)$	$q \langle x^3 - 3xy^2 \rangle$
	skew sextupole	$-eq \langle 3x^2y - y^3 \rangle (3x^2y - y^3)W'_3(z)$	$q \langle 3x^2y - y^3 \rangle$

Table 2.1. Longitudinal wake fields decomposition into modes, due to charged beam momenta.

if and only if the driving beam has a multipole moment of order m . Looking at Table 2.2, for example, for a dipole moment $m = 1$, horizontal displacement entails a dipole moment bending force in the horizontal or vertical direction. For $m = 2, 3$, the wakes act like quadrupole and skew quadrupole, sextupole and skew sextupole, respectively.

m	mode	Transverse Wakes	Moments of the driving beam
0	monopole	0	q
1	dipole	$-eq \langle x \rangle \hat{x} W_1(z)$	$q \langle x \rangle$
	dipole	$-eq \langle y \rangle \hat{y} W_1(z)$	$q \langle y \rangle$
2	quadrupole	$-2eq \langle x^2 - y^2 \rangle (x\hat{x} - y\hat{y}) W_2(z)$	$q \langle x^2 - y^2 \rangle$
	skew quadrupole	$-2eq \langle 2xy \rangle (y\hat{x} + x\hat{y}) W_2(z)$	$q \langle 2xy \rangle$
3	sextupole	$-3eq \langle x^3 - 3xy^2 \rangle [(x^2 - y^2)\hat{x} - 2xy\hat{y}] W_3(z)$	$q \langle x^3 - 3xy^2 \rangle$
	skew sextupole	$-3eq \langle 3x^2y - y^3 \rangle [2xy\hat{x} + (x^2 - y^2)\hat{y}] W_3(z)$	$q \langle 3x^2y - y^3 \rangle$

Table 2.2. Transverse wake fields decomposition into modes, due to charged beam momenta.

2.2.4 General properties of Wake functions

A simple sketch of longitudinal and transverse wake functions, $W'_m(z)$ and $W_m(z)$, is reported in Fig. 2.8. The longitudinal wake function starts from a positive

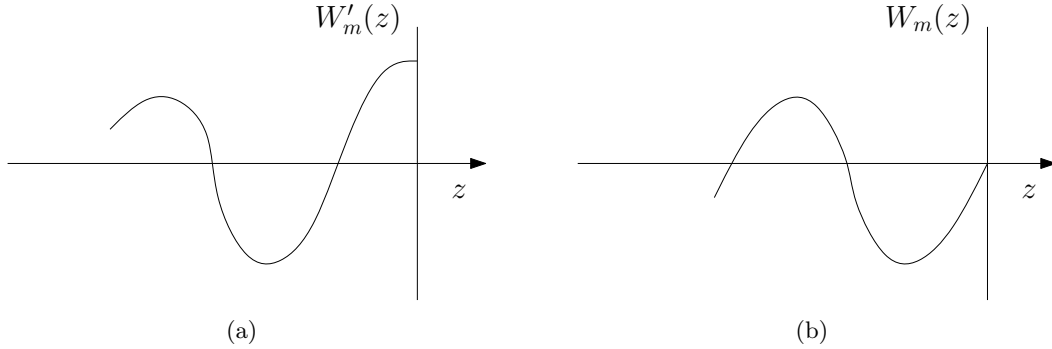


Figure 2.8. a) longitudinal and b) transverse wake functions, showing their different starting values.

value, while the transverse one from zero. Consistently with the assumptions at the beginning of the section, z is measured from the source particle in the direction of longitudinal particle motion, so as for a following witness particle to be $z < 0$. This ensures for $W'_m(z)$ to be the derivative of $W_m(z)$ with respect to z . Both wake functions vanish for $z > 0$ because of causality, while $W'_m(0_-) \geq 0$ as a result of energy conservation. It is noteworthy to say that the finite non zero value of $W'_m(0)$ and of $\lim_{z \rightarrow 0^-} W'_m(z)$ represent how much of its own wake the source particle actually sees.

This latter qualitative statement finds its mathematical proof in the fundamental theorem of beam loading, formulated by P. Wilson [26], which states that a particle sees exactly half of its own wake, $\frac{1}{2}W'_m(0_-)$. To prove the theorem, let a particle of charge q traverse a thin lossless cavity, exciting it. Assuming f to be the fraction of its own wake experienced by the particle, it will gain an energy $\Delta\mathcal{E}_1 = -fq^2W'_m(0_-)$. If a second particle with the same charge passes the cavity half a cycle later, it will gain an energy $\Delta\mathcal{E}_2 = -fq^2W'_m(0_-) + q^2W'_m(0_-)$, where the contribution $-fq^2W'_m(0_-)$ comes from its own wake and $q^2W'_m(0_-)$ from the wake left behind by the first

particle. Thus, being the cavity lossless, the field inside cancels out and

$$\Delta\mathcal{E}_1 + \Delta\mathcal{E}_2 = -2fq^2W'_m(0_-) + q^2W'_m(0_-) = 0, \quad (2.26)$$

which implies $f = \frac{1}{2}$. Adopting the same physical picture used to proof the beam loading theorem and using its result, another important property of wake functions can be deduced. If the first particle, indeed, loses an energy $\frac{1}{2}q^2W'(0_-)$ and the second $\frac{1}{2}q^2W'_0(-z)$, the total loss will be $q^2W'(0_-) + q^2W'_0(-z) \geq 0$. If, again, the second particle brings a charge $-q$, the total loss will be $q^2W'(0_-) - q^2W'_0(-z) \geq 0$. Thus bringing the latter two disequalities together, implies

$$|W'_m(-z)| \leq W'_m(0_-), \quad (2.27)$$

which means that $W'_m(z)$ is bounded by the value at 0_- for all $z \neq 0$. If $W'_m(-D) = W'_m(0_-)$ for some $D > 0$, the wake is periodic with period D^2 . Let's take into consideration a dc beam current I . Then, for a beam particle of charge q the energy loss would be $q \int W'_0(z)I/v dz \geq 0$, so as the area under $W'_m(z)$ is non negative. Finally, it must be noticed that from eqs. 2.24- 2.25 results clear that the most important mode for the longitudinal wake is the lowest azimuthal for $m = 0$, $W'_0(z)$, while for the transverse it is the lowest for $m = 1$, $W_1(z)$. Higher azimuthal modes can be relevant for large transverse beam sizes with respect to beam pipe radii.

2.3 Wake Potentials

Similar to the description of the wake fields excited by charged particles by means of wake functions, wake potentials are the integrals of the electromagnetic forces exerted by wake fields excited by a bunch of particles of finite length, at the position of a following witness particle. In this case, instead of measuring the distance of the witness particle from the source one, the distance of the witness particle from the bunch center will be of concern. For any bunch of arbitrary shape, the wake potentials can be found as the convolution of the wake functions with the normalized line density

$$\int_{-\infty}^{\infty} \lambda(\tau) d(\tau) = 1, \quad (2.28)$$

where τ is the time of arrival of a reference particle at a designated point in the accelerator ring ahead of the synchronous particle. The longitudinal wake potential is given by

$$W_{\parallel}^{\lambda}(\tau) = \int_0^{\infty} W'_0(t)\lambda(\tau - t) dt, \quad (2.29)$$

where the integration can be taken from 0 to ∞ because the wake function of a particle vanishes in front of it ($t < 0$, $z > 0$)³. So the wake functions come out to be the wake potentials of a delta function distribution, thus Green functions for the wake potentials of finite charge distributions in the considered structure.

²For a proof of this assertion, the textbook by K. Y. Ng is referred [23].

³This is because of causality, as discussed in section 2.2.4.

The transverse wake potential can also be found, given the transverse wake function for a particular geometry. In this case, assuming a constant displacement of the bunch from the longitudinal axis, the convolution with the charge density returns to be

$$W_{\perp}^{\lambda}(\tau) = \int_0^{\infty} W_m(t)\lambda(\tau - t) dt, \quad (2.30)$$

with $m \neq 0$. If the assumption of the constant displacement of the bunch from the traveling axis cannot be taken anymore as valid, with different parts of the bunch having different displacements $\xi(\tau)$, then the equation 2.30 must be replaced by

$$W_{\perp}^{\lambda}(\tau) = \frac{1}{\bar{\xi}} \int_0^{\infty} W_m(t)\xi(\tau - t)\lambda(\tau - t) dt, \quad (2.31)$$

where the first moment of the distribution function, $\xi(\tau)\lambda(\tau)$, has been used and the whole expression has been divided by the average displacement $\bar{\xi}$.

The computation of the wake functions for point charges is generally a very complicated task, affordable only in few cases for simplified structures for which an analytical solution can be found. Usually cylindrical pillbox cavities accomplish this condition. For arbitrary (and in many cases, very complicated) geometries, the wake functions calculations cannot be performed with sufficient accuracy, making the calculation of the wake potentials for finite bunches the only practicable approach to the problem. Then, given a finite bunch length σ_z , $\lim_{\sigma_z \rightarrow 0} \lambda(s, \sigma_z) = \delta(s)$, thus the wake functions for a particular geometry of interest could also be, in principle, approximated by the wake potentials calculated for a bunch length as short⁴ as reasonably allowed by the computer code used.

2.4 Beam coupling Impedance

2.4.1 Longitudinal impedance

Beam particles form current. For the following discussion a current harmonic component with frequency ω , $I(s, t) = \hat{I}e^{-i\omega(t-s/v)}$, will be considered⁵. As the wake functions describe the wake effects in the time domain, impedances do it in the frequency domain. This is useful especially for accelerator rings, where beam particles traverse the same positions periodically in time (also several millions of times per second). Let a particle of charge q traverse a discontinuity in the vacuum chamber at some position s_i along the chamber axis. According to Fig. 2.9, that particle will experience the wake left by the particles $-z$ in front, gaining a voltage

⁴Short means much lower than the “nominal” bunch length, i.e. the bunch length at which wake potentials are currently calculated. As an example, the nominal bunch length of LHC beams is $\sigma_z = 7.5$ cm. Wake functions, for instance, could be approximated by a wake potentials calculation for a bunch length, say, of the order of 1 mm.

⁵The Fourier harmonic of a function $f(t)$ is defined as $\hat{f} = f(\omega) \equiv \int_{-\infty}^{\infty} f(t)e^{i\omega t} dt$.

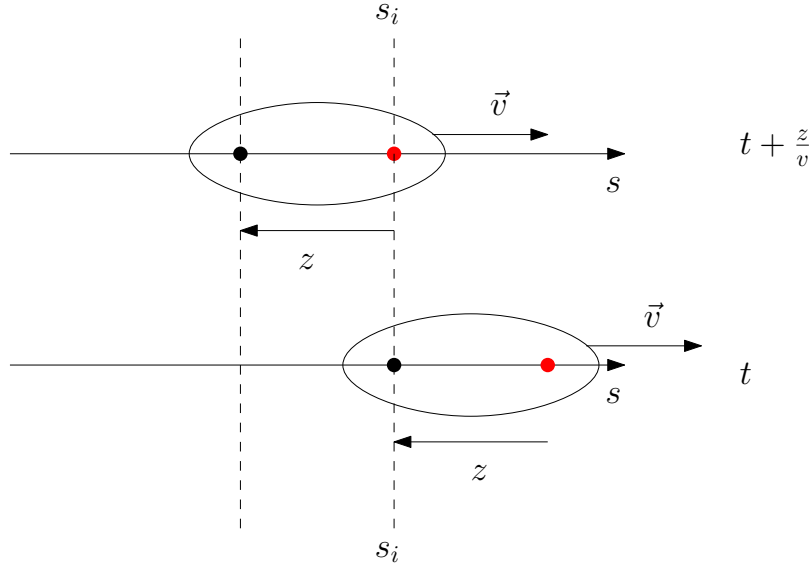


Figure 2.9. The particle beam moves to the right. The source particle is in red, the witness in black. Witness particle crosses the discontinuity at s_i at time t , after the source has already passed at earlier time $t + \frac{z}{v}$, experiencing the wake this latter left behind. It has to be recalled that z is negative from source to witness particle.

($m = 0$)

$$V(s_1, t) = - \int_{-\infty}^{\infty} [W'_0(z)]_i \left[\hat{I} e^{-i\omega[(t+z/v)-s_1/v]} \frac{dz}{v} \right] = \quad (2.32)$$

$$= -I(s_1, t) \int_{-\infty}^{\infty} [W'_0(z)]_i e^{-i\omega z/v} \frac{dz}{v}, \quad (2.33)$$

where the definition of the longitudinal impedance $[Z_0^{\parallel}(\omega)]_i$ at location s_i can be identified. For instance, if the potential across the discontinuity at s_1 is written as $V(s_1, t) = \hat{V}_1 e^{-i\omega(t-s_1/v)}$, the above equation simplifies to

$$\hat{V}_1 = -\hat{I} \int_{-\infty}^{\infty} [W'_0(z)]_i e^{-i\omega z/v} \frac{dz}{v} \equiv -\hat{I} [Z_0^{\parallel}(\omega)]_i. \quad (2.34)$$

Therefore the longitudinal impedance of azimuthal mode $m = 0$ over one turn of the accelerator ring follows directly from eq. 2.34, summing up over all i discontinuities

$$Z_0^{\parallel} = \int_{-\infty}^{\infty} W'_0(z) e^{-i\omega z/v} \frac{dz}{v}, \quad (2.35)$$

where $Z_0^{\parallel} = \sum_i [Z_0^{\parallel}(\omega)]_i$ and $W'_0(z) = \sum_i [W'_0(z)]_i$.

Having beams also transverse dimension, they bring higher azimuthal multipoles, as specified in Tables 2.1 and 2.2, that become crucial when the beam is off-center

by an amount a . The m_{th} current multipole is $Q_m(s, t) = I(s, t)a^m = \hat{Q}e^{-i\omega(t-s/v)}$ and the corresponding m_{th} multipole element is $Q_m(s, t) dz/v$. Following the above discussion about the $m = 0$ case for the wake left behind an on-axis source particle and experienced by a witness on-axis particle, traversing a discontinuity at location s_i , a test particle at the same location s_i at time t , would now experience a m_{th} azimuthal wake left behind by a m_{th} multipole element passed a time $-\frac{z}{v}$ earlier. Being $\frac{\delta(r-a)\delta(\theta)}{a}$ the particle density needed to integrate over all particles, in the beam, which are off-axis by a , the gain in voltage of the witness particle will now be

$$\begin{aligned} V(s_i, t) &= - \int Q_m(s_i, t + z/v) [W'_m(z)]_i \frac{dz}{v} \int r^m \cos(m\theta) \frac{\delta(r-a)\delta(\theta)}{a} r dr d\theta = \\ &= - \int \hat{Q} e^{-i\omega[(t+z/v)-s/v]} [W'_m(z)]_i a^m = \\ &= - \frac{P_m}{q} Q_m(s_i, t) \int_{-\infty}^0 [W'_m(z)]_i e^{-i\omega z/v} \frac{dz}{v}, \end{aligned} \quad (2.36)$$

with $P_m = qa^m$. Again as for the $m = 0$ case, given the m_{th} multipole longitudinal impedance at location i

$$[Z_m^{\parallel}(\omega)]_i = - \frac{q\hat{V}}{P_m} \hat{Q}_m = \int_{-\infty}^{\infty} [W'_m(z)]_i e^{-i\omega z/v} \frac{dz}{v}, \quad (2.37)$$

the whole ring longitudinal impedance will be given by the sum $Z_m^{\parallel} = \sum_i [Z_m^{\parallel}(\omega)]_i$.

2.4.2 Transverse impedance

If in the above eqs. 2.33 and 2.37 the longitudinal wake functions $W'_m(z)$ are replaced by the transverse ones $W_m(z)$, the definition of transverse impedance immediately follows

$$Z_m^{\perp}(\omega) = \frac{i}{\beta} \int_{-\infty}^{\infty} W_m(z) e^{-i\omega z/v} \frac{dz}{v}. \quad (2.38)$$

Owing to the Panofsky-Wenzel theorem, longitudinal and transverse impedances are related by

$$Z_m^{\parallel}(\omega) = \frac{\omega}{c} Z_m^{\perp}(\omega). \quad (2.39)$$

Both $Z_m^{\parallel}(\omega)$ and $Z_m^{\perp}(\omega)$ are complex functions of ω and their real parts, $\text{Re}\{Z_m^{\parallel}(\omega)\}$ and $\text{Re}\{Z_m^{\perp}(\omega)\}$ represent an energy gain or loss. They are recognized as the *real resistive* component of the impedance. In order for $\text{Re}\{Z_m^{\perp}(\omega)\}$ to dissipate energy, the transverse force $F_{\perp} \propto -W_m$ must have a phase shift of $\frac{\pi}{2}$ with respect to Q_m , that is why of the factor i in front of eq. 2.38.

2.4.3 General properties of impedances

In addition to the consequence of the Panofsky-Wenzel theorem for the impedance, eq. 2.39, other properties characterize this quantity, like those already shown for

the wake functions. For instance, because the function $W_m(z)$ is real, it follows that $Z_m^\parallel(-\omega) = [Z_m^\parallel(\omega)]^*$ and $Z_m^\perp(-\omega) = -[Z_m^\perp(\omega)]^*$. The equations defining longitudinal and transverse impedances, eqs. 2.37 and 2.38, can be managed to write down the expressions for $W'_m(z)$ and $W_m(z)$ as functions of $Z_m^\parallel(\omega)$ and $Z_m^\perp(\omega)$:

$$W'_m(z) = \frac{1}{2\pi} \int_{-\infty}^{\infty} Z_m^\parallel(\omega) e^{i\omega z/v} d\omega \quad (2.40)$$

$$W_m(z) = -\frac{i\beta}{2\pi} \int_{-\infty}^{\infty} Z_m^\perp(\omega) e^{i\omega z/v} d\omega, \quad (2.41)$$

in which the causality requires $W'_m(z) = W_m(z) = 0, \forall z > 0$. Thus it follows that both $Z_m^\parallel(\omega)$ and $Z_m^\perp(\omega)$ are analytic functions of ω , with poles in the upper half ω -plane only. Being the upper half ω -plane free of singularities⁶, Hilbert transforms of $Z_m^\parallel(\omega)$ and $Z_m^\perp(\omega)$ result in

$$\operatorname{Re}\{Z_m^\parallel(\omega)\} = \frac{1}{2\pi} \mathcal{P} \int_{-\infty}^{\infty} \frac{\operatorname{Im}\{Z_m^\parallel(\omega')\}}{\omega' - \omega} d\omega' \quad (2.42)$$

$$\operatorname{Im}\{Z_m^\parallel(\omega)\} = -\frac{1}{2\pi} \mathcal{P} \int_{-\infty}^{\infty} \frac{\operatorname{Re}\{Z_m^\parallel(\omega')\}}{\omega' - \omega} d\omega', \quad (2.43)$$

and

$$\operatorname{Re}\{Z_m^\perp(\omega)\} = \frac{1}{2\pi} \mathcal{P} \int_{-\infty}^{\infty} \frac{\operatorname{Im}\{Z_m^\perp(\omega')\}}{\omega' - \omega} d\omega' \quad (2.44)$$

$$\operatorname{Im}\{Z_m^\perp(\omega)\} = -\frac{1}{2\pi} \mathcal{P} \int_{-\infty}^{\infty} \frac{\operatorname{Re}\{Z_m^\perp(\omega')\}}{\omega' - \omega} d\omega', \quad (2.45)$$

\mathcal{P} being the principal value. If the beam pipe has the same entrance and exit cross-section, there will be no trapped wake fields inside the pipe, resulting in no accelerating forces generating from the pipe itself, thus $\operatorname{Re}\{Z_m^\parallel(\omega)\} \geq 0$ and $\operatorname{Re}\{Z_m^\perp(\omega)\} \geq 0$. Finally, recalling the Panofsky-Wenzel theorem and that $W_m(z) = 0$ at $z = 0$, the following equalities hold for the imaginary parts of longitudinal and transverse impedances, due respectively to the two conditions just mentioned:

$$\int_0^{\infty} \frac{\operatorname{Im}\{Z_m^\parallel(\omega)\}}{\omega} d\omega = 0$$

⁶Many textbooks and reviews on beam coupling impedances use the so called “engineering” convention $j = -i$, thus using $e^{j\omega t}$ instead of $e^{i\omega t}$ factor in the Fourier transforms. In that case all the above and following impedance properties remain the same, given the exponential factor convention is accordingly applied, apart from no singularities existing in the lower half ω -plane.

and

$$\int_0^{\infty} \text{Im}\{Z_m^{\perp}(\omega)\} d\omega = 0.$$

It must be pointed out that because of analyticity, both $\text{Re}\{Z_0^{\parallel}(\omega)\}/\omega$ and $\text{Re}\{Z_1^{\perp}(\omega)\}$ must vanish at $\omega = 0$. The physical reason for this to happen is that at $\omega = 0$ no Faraday-Lenz's law (eq. 2.11) exists, establishing no relation between \vec{E} and \vec{B} fields. This means that no dc loss occur and because no image currents are created, no beam coupling impedance does arise.

2.4.4 Resonator impedance

Cavity structures usually show an impedance behaviour in frequency consisting of many resonant peaks, mainly due to trapped modes. These latter are electromagnetic field resonances with frequencies below the lowest cutoff frequency of the beam pipe. A parallel RLC resonator circuit, consisting of a resistance, an inductance and a capacitance, can be used to approximate each of these resonances [27]. The admittance of such a circuit can be easily calculated from the elementary circuit theory as

$$Y(\omega) = G + i\frac{1}{\omega L} - i\omega C, \quad (2.46)$$

where $G = R_s$ is the conductance of the circuit (not to be confused with the conductance of the metallic wall), R_s being usually recognized as the shunt impedance, L is the inductance and C the capacitance. From eq. 2.46 the complex impedance of the parallel resonator circuit directly follows,

$$Z_{\parallel}(\omega) = \frac{R_s}{1 - iQ_r(\omega/\omega_r - \omega_r/\omega)}, \quad (2.47)$$

where $\omega_r = 1/\sqrt{LC}$ is the resonant frequency, i.e. the frequency at which the real part of the impedance reach the maximum $\text{Re}\{Z_{\parallel}\} = R_s$ while its imaginary part vanishes and $Q_r = R_s\sqrt{C/L}$ is the quality factor. When the wall resistivity increases Q_r decreases, the shunt impedance being inversly proportional to the wall resistivity. The difference between the maximum and minimum frequencies delimiting the range where the impedance reaches half of its maximum is defined as the resonance bandwidth $\Delta\omega$, related to Q_r by $Q_r = \omega_r/\Delta\omega$. For $\omega \rightarrow 0$ the real part of the impedance vanishes quadratically as $\omega^2 R_s/\omega_r^2 Q_r^2$, and the impedance is purely imaginary reactive. For $\omega = \omega_r$, the impedance is purely real and equal to R_s . The real part of the impedance is always positive.

For cavities made by good metallic conductors, usually $Q_r \gg 1$ and the impedance shows many well distinguishable resonant peaks, due to parasitic Higher Order Modes (HOMs), and thus is generally referred to as *narrow-band impedance*. Its expression can be simplified near the resonance. For small deviation from ω_r , $\zeta = \delta\omega/\omega_r \ll 1$, indeed, it is given by

$$Z_{\parallel}(\omega) \approx \frac{R_s}{1 - 2iQ_r\zeta} = R_s \frac{1 + 2iQ_r\zeta}{1 + (2Q_r\zeta)^2}, \quad (2.48)$$

for which the real part reaches its half maximum at $\zeta = \pm\omega_r/2Q_r$.

The narrow-band impedance may be described as a sum of narrow resonances. Each resonance is produced by a localized mode whose frequency is below or not much above the cutoff frequency of openings present in the structure. In the time domain, this corresponds to a slowly decaying oscillating wake potential. Above the cutoff frequency, in the high frequency region, the resonances overlap producing a smooth frequency dependence of the impedance. In the time domain this corresponds to the short range behaviour of the wake potential. The high-frequency impedance is significant if the bunch length is small compared to the beam pipe radius. It describes the interaction of particles due to the presence of abrupt changes of the beam pipe cross section and of high-frequency tails of resonant structures. If the bunch length is larger than the beam pipe radius, the detailed behaviour of the high-frequency impedance can be approximated by a smooth function generally referred to as *broad-band impedance*. All vacuum chamber gaps and breaks, joints, Beam Position Monitors (BPMs), bellows, tapers, can be lumped into a term of the type of eq. 2.47, with $Q_r \approx 1$ and $\omega_r \approx \omega_c$, ω_c being the beam pipe cutoff frequency. Just as an example, in Fig. 2.10 a schematic behaviour of the transverse impedance is shown, with the real and imaginary parts being odd and even functions of frequency, respectively.

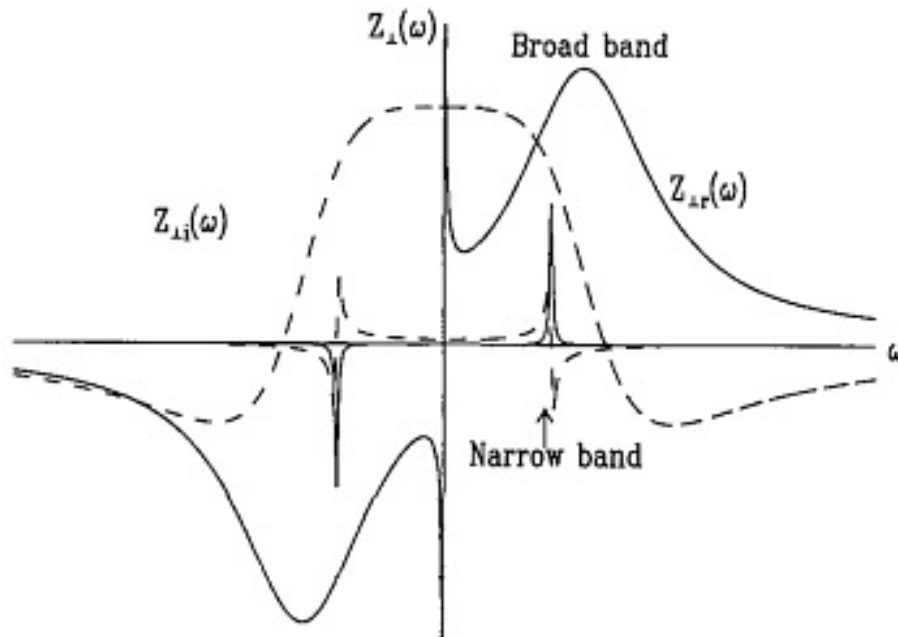


Figure 2.10. General behaviour of the transverse broad-band and narrow-band impedance for an arbitrary accelerator ring. Solid lines represent real parts whereas dashed lines imaginary parts (picture adapted from S. Y. Lee's book [28]).

Broad-band impedances and, thus, wake potentials, can be resistive, inductive or capacitive, depending on the dominant term in eqs. 2.46 and 2.47 [29].

In the resistive case, the impedance is given by a broad-band resonator at

frequency $\omega_r \approx \omega_b$, where $\omega_b = c/\sigma_z$ is the cutoff frequency of the bunch of length σ_z . The real part of the impedance dominates, with $\text{Re}\{Z_{\parallel}(\omega)\} \approx \text{const.}$, while the imaginary part switches sign for frequencies below ω_r and frequencies above ω_r , which partly cancel each other.

For the inductive impedance, ω_r is far above the cutoff frequency of the bunch and the impedance is dominated by its negative imaginary part, which grows proportional to ω in the frequency range of the bunch, $\text{Im}\{Z_{\parallel}(\omega)\} \propto -\omega$. The wake fields transfer energy from the head to the tail of the bunch. The overall energy loss is proportional to the real part of the impedance and can be neglected.

For the capacitive impedance, the resonance frequency is much lower than ω_b and the impedance is dominated by the capacitor $\text{Im}\{Z_{\parallel}(\omega)\} \propto \omega^{-1}$, while the real part due to the resistivity is proportional to $1/\omega^2$. As an example for a qualitative analysis of the different impedance behaviours, the inductive, resistive and capacitive action on impedance and corresponding wake potential, of a single resonant mode, is shown in Fig. 2.11, for quality factors $Q_r = 100, 0.5, 10$ respectively. Given the bunch distribution in frequency and time domain (for the impedance and wake potentials, respectively), reported in dotted lines, it is clear that for the inductive impedance the response lags in phase behind the excitation, while for the capacitive one the response is ahead of the excitation.

2.4.5 Bunch modes

Particles in bunches perform *synchrotron oscillations*, which are longitudinal periodic oscillations of the time delay from the synchronous particle and of energy deviations about its nominal energy. This phenomenon is due to the applied radiofrequency voltage and the drift of particles with different energies. It is an *incoherent* effect occurring with arbitrary phases, leading to the net effect of generated external fields cancelling out.

The bunch oscillations as a whole, instead, is a *coherent* phenomenon, which generates external electromagnetic fields that interact with the vacuum chamber wall. In the longitudinal phase space $\tau - \Delta E$, where τ is the arrival time of the beam particle ahead of the synchronous particle, and ΔE the energy deviation, such oscillations are characterized by the bunch shape mode number m , for the azimuthal ϕ -coordinate⁷, as sketched in Fig. 2.12. The bunch stationary mode corresponds to $m = 0$, while the dipole, quadrupole, sextupole etc. modes correspond to values of $m = 1, 2, 3, \dots, m$ giving also the number of nodes where the bunch line density vanishes, as also shown in the lower part of Fig. 2.12. Dipole mode oscillation is usually observed when the injection of the beam occurs with a phase error, whereas the quadrupole mode occurs in case of a mismatch between the bunch and the RF bucket.

It is possible to derive analytically the bunch spectrum modes, following the arrival time τ of a particle ahead of the synchronous particle, at a fixed location along the accelerator ring. If θ is the azimuthal angle of the location along the ring

⁷Because the beam particles execute synchrotron oscillations, it is more convenient to use circular coordinates (r, ϕ) in the longitudinal phase space, defined as $\tau = r \cos(\phi)$ and $p_{\tau} = r \sin(\phi)$, p_{τ} being the particle conjugate momentum.

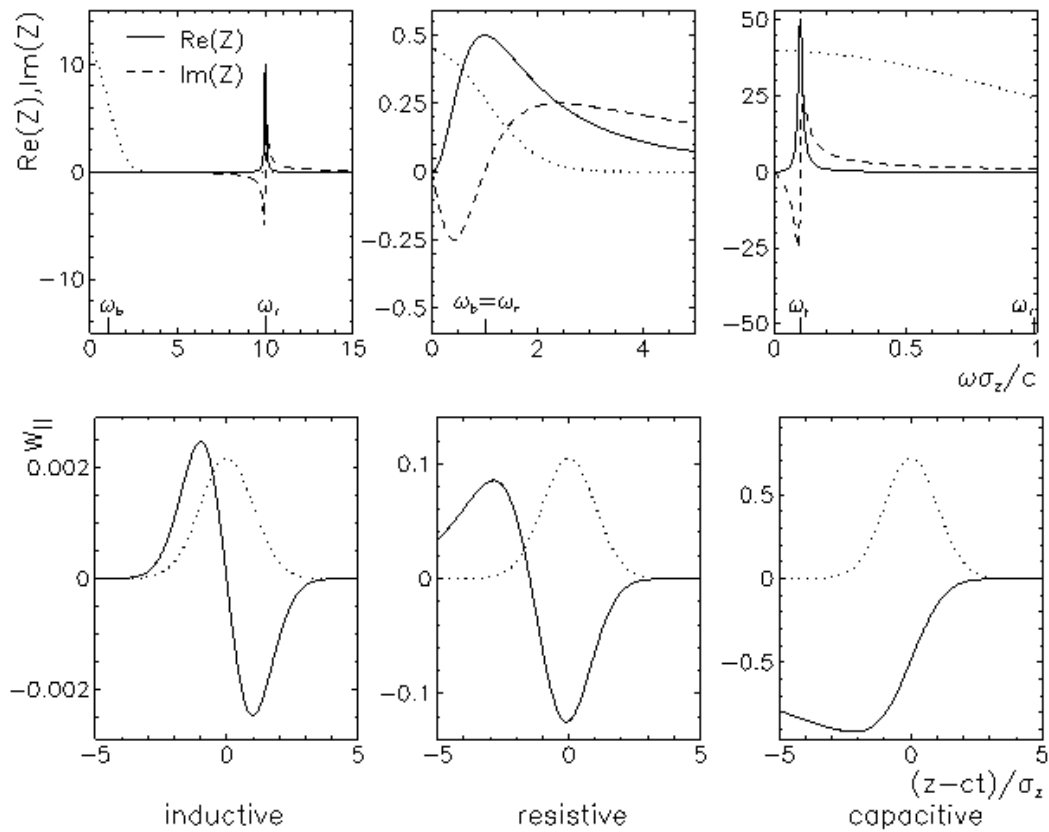


Figure 2.11. Impedance (up) and wake potential (down) for single modes acting on a bunch mainly inductively, resistively and capacitively. Solid curves represent real part of the impedances, dashed ones the imaginary part and the dotted line the bunch distribution in frequency and time domains.

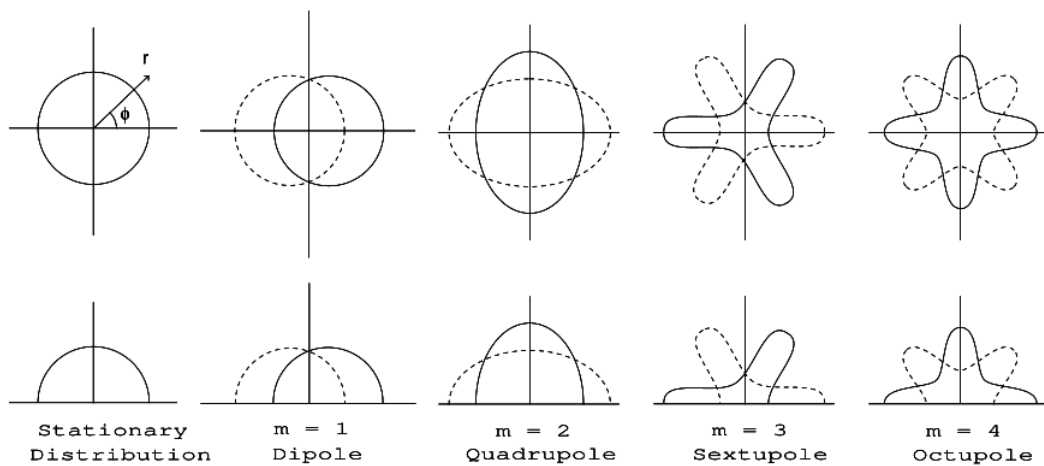


Figure 2.12. Top, azimuthal synchrotron modes of a bunch in the longitudinal phase space and, bottom, as linear density [23].

the signal recorded, for example, by a wall-gap monitor placed at $\theta_0 = 0$ will be

$$I(\hat{\tau}, \phi, s) = ev \sum_{k=-\infty}^{\infty} \delta \left[s + R\theta_0 - kC_0 - v\hat{\tau} \cos \left(\frac{\omega_s s}{v} + \phi \right) \right], \quad (2.49)$$

where C_0 is the length of the closed orbit followed by the synchronous particle with velocity v , R its mean radius, ω_s the synchrotron frequency and $\hat{\tau}$ the amplitude of synchrotron oscillation reflected in the cosine term. The synchrotron oscillation amplitude is usually small, i.e. $v\hat{\tau} \ll C_0$, so that it is possible to substitute $s = kC_0$ in the cosine term of eq. 2.49. Moreover, given the integral representation of the δ -function and the relations

$$e^{jx \cos \phi} = \sum_{m=-\infty}^{\infty} (-j)^m J_m(x) e^{-jm\phi}; \quad \frac{1}{2\pi} \sum_{k=-\infty}^{\infty} e^{jk\theta} = \sum_{n=-\infty}^{\infty} \delta(\theta - 2\pi n) \quad (2.50)$$

for the mathematical formula of Bessel functions, on the left, and the Poisson formula, on the right, eq. 2.49 can be written as

$$\begin{aligned} I(\hat{\tau}, \phi, s) &= \frac{e}{2\pi} \int_{-\infty}^{\infty} \sum_{k=-\infty}^{\infty} e^{j[s - kC_0 - \hat{\tau}v \cos(k\omega_s C_0/v + \phi)]\omega/v} d\omega = \\ &= \frac{e}{2\pi} \int_{-\infty}^{\infty} \sum_{k=-\infty}^{\infty} \sum_{m=-\infty}^{\infty} (-j)^m J_m(\omega\hat{\tau}) e^{j(s - kC_0)\omega/v} e^{jm(k\omega_s C_0/v + \phi)} d\omega = \\ &= \frac{e}{T_0} \int_{-\infty}^{\infty} \sum_{n=-\infty}^{\infty} \sum_{m=-\infty}^{\infty} (-j)^m J_m(\omega\hat{\tau}) \delta(\omega - n\omega_0 - m\omega_s) e^{jm\phi} e^{j\omega s/v} d\omega = \\ &= \frac{e}{T_0} \sum_{n=-\infty}^{\infty} \sum_{m=-\infty}^{\infty} (-j)^m J_m[(n\omega_0 + m\omega_s)\hat{\tau}] e^{jm\phi} e^{j(n\omega_0 + m\omega_s)s/v}, \quad (2.51) \end{aligned}$$

where $T_0 = 2\pi/\omega_0$ is the revolution period of the synchronous particle. Thus the spectrum is composed of synchrotron sidebands on both sides of the revolution harmonics, whose amplitudes are given by the Bessel functions J_m . To observe m -th order sidebands, one should go to a frequency where $J_m(n\omega_0\hat{\tau})$ has a maximum, or at $n\omega_0\hat{\tau} \sim m$. The spectrum of a beam particle performing synchrotron oscillations is reported in Fig. 2.13.

Magnetic quadrupoles are always present in an accelerator ring, in order to achieve transverse focusing of the beam that otherwise would hit the vacuum chamber and get lost. They can focus in one transverse plane only, defocusing in the other. For this reason, the beam has also transverse motion. Thus transverse oscillations develop in both transverse planes and are called *betatron oscillations* with *betatron frequencies* $\omega_\beta/2\pi$, different in the two transverse planes. The *betatron tune* is defined as the number of betatron oscillations made by the beam in a revolution turn, $\nu_\beta = \omega_\beta/\omega_0$. The transverse motion of a beam is commonly monitored by a system of BPMs. Thus, in analogy to the discussion preliminary to eq. 2.49, it is possible to write down the transverse displacement of a charged particle registered

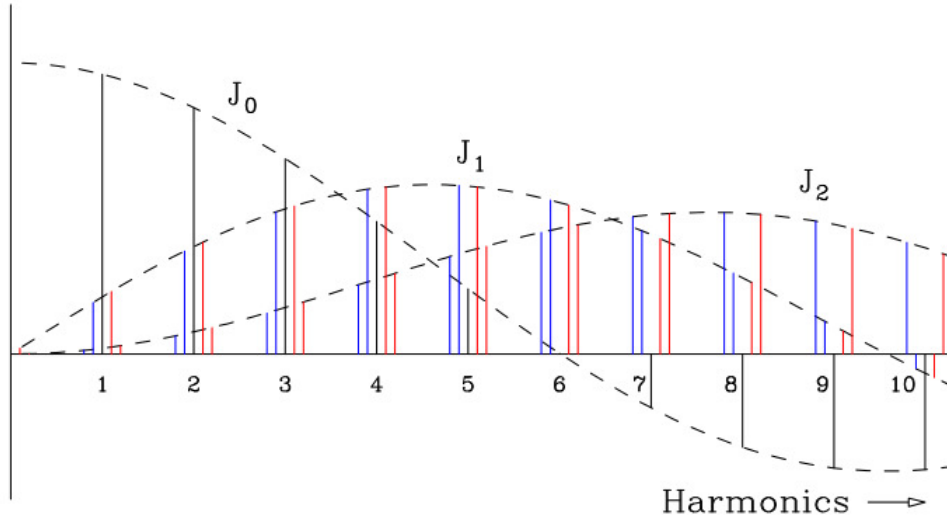


Figure 2.13. Spectrum of a beam particle performing synchrotron oscillations, in the positive frequency range only and for $\omega\hat{\tau} = 0.4$ which is usually a large value. The m -th revolution harmonic is bounded by the Bessel function of order m , J_m [23].

at a BPM at position θ_0 along the ring, as

$$\begin{aligned}
 d(\psi, \theta, t) &= e\omega_0 A \cos(\nu_\beta \omega_0 t + \psi) \sum_{p=-\infty}^{\infty} \delta(\omega_0 t - \theta + \theta_0 - 2\pi p) = \\
 &= \frac{e\omega_0 A}{2\pi} \cos(\nu_\beta \omega_0 t + \psi) \sum_{n=-\infty}^{\infty} e^{j(n\omega_0 t - n\theta + n\theta_0)} = \\
 &= \frac{e\omega_0 A}{2\pi} \sum_{n=-\infty}^{\infty} \left\{ e^{j[(n+\nu_\beta)\omega_0 t - n(\theta - \theta_0) + \psi]} + e^{j[(n-\nu_\beta)\omega_0 t - n(\theta - \theta_0) - \psi]} \right\} = \\
 &= \frac{e\omega_0 A}{2\pi} \sum_{n=-\infty}^{\infty} \left\{ e^{j[(n+\nu_\beta)\omega_0 t - n(\theta - \theta_0) + \psi]} + e^{-j[(n+\nu_\beta)\omega_0 t - n(\theta - \theta_0) + \psi]} \right\} = \\
 &= \frac{e\omega_0 A}{2\pi} \sum_{n=-\infty}^{\infty} \cos[(n + \nu_\beta)\omega_0 t - n(\theta - \theta_0) + \psi] = \\
 &= \frac{e\omega_0 A}{2\pi} \sum_{n=-\infty}^{\infty} \cos[(n - \nu_\beta)\omega_0 t - n(\theta - \theta_0) - \psi], \tag{2.52}
 \end{aligned}$$

where A is the amplitude of the betatron oscillation and ψ is the betatron phase at time $t = 0$. The last two equations above show that both positive and negative harmonics can be dealt with, so both upper and lower sidebands can appear, as shown in Fig. 2.14. Because BPMs and network analyzers monitor positive frequencies only, it is common convention to talk about upper sidebands only and for the dipole current registered by the BPM the second to last expression in eq. 2.52 is assumed. It consists of waves with phase velocity

$$\omega_{ph} = (1 + \nu_\beta)\omega_0, \quad n \neq 0, \tag{2.53}$$

which in turn corresponds to two type of waves, fast waves with $n > 0$ and $\omega_{ph} > \omega_0$ and slow waves with $n < 0$ and $\omega_{ph} < \omega_0$. Actually the betatron tune has an integer

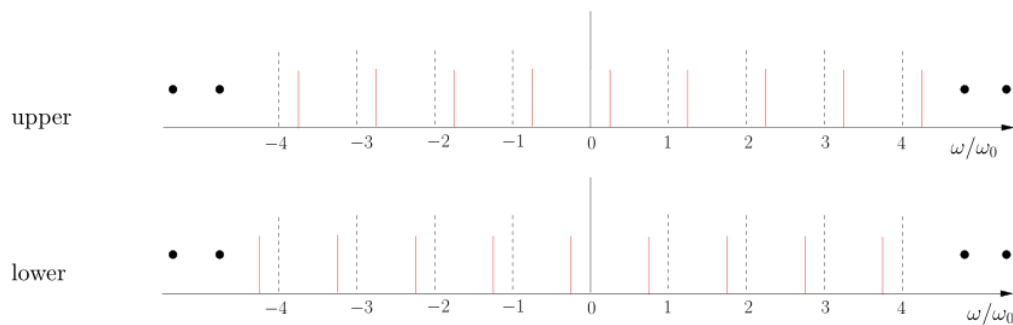


Figure 2.14. Upper and lower betatron sidebands spectra of a single particle performing betatron oscillations, with the fast waves in red solid lines and slow waves in black dashed lines. Both spectra lead to the same physical observation [23].

part and a non integer part, what in addition to fast and slow waves gives rise to backward waves also. For a detailed discussion of this real case other textbooks are addressed [22, 23]. What is important to say here is that the distinction between fast and slow waves is crucial because only slow waves can be susceptible to instabilities, because of $\text{Re}\{Z_1^\perp(\omega)\}$ being an even function of ω , as discussed in section 2.4.3.

The two above discussions about synchrotron and betatron oscillations were exploited referring to a single particle in a bunch. For many particles, both the current $I(\hat{r}, \phi, s)$ and the dipole moment $d(\psi, \theta, t)$ in eqs. 2.51 and 2.52 respectively, are obtained summing up the currents and dipole moments of all particles. In the case of the dipole moment, because the betatron phase ψ is random among the particles, this sum will average to zero, which means that all the upper and lower sidebands will be observable only when excited coherently by a transverse driving force, like a kicker or a transverse coupling impedance [23].

2.4.6 Loss factor, kick factor and effective impedance

The energy loss of a bunched beam, caused by both wake fields generated while traversing vacuum chamber discontinuities and synchrotron radiation, deserves accurate calculations in order to avoid overheat of sensitive elements that, because of temperature increase, can suffer deformations or even destruction. These latter phenomena can occur despite of the whole beam absorption, as in the case of beam dumps, because the portion of the energy spectrum above the beam pipe cutoff propagates, in general, out of the cavity-like object, travelling along the pipe.

The calculation of this energy loss is much simplified if the concepts of *loss* and *kick factors* are introduced. The loss factor include the energy loss of the beam travelling parallel to the reference trajectory. The kick factor (or transverse loss factor) accounts for the dependence of the energy loss on the beam transverse displacement with respect to the beam trajectory, describing a localised deflection exerted on the beam.

Recalling the discussion in section 2.2.4, if a bunch passes through a given structures, it will suffer an energy change proportional to the square of the charge⁸,

⁸The energy change is equal to the product of the bunch charge q and the induced voltage

written as

$$\Delta\mathcal{E} = -k_{\parallel}q^2, \quad (2.54)$$

where k_{\parallel} is the (longitudinal) loss factor. In the frequency domain, the energy loss is given by the integral of the product of the longitudinal impedance $Z_{\parallel}(\omega)$ and the bunch power spectrum $h(\omega) = \hat{\lambda}(\omega)\hat{\lambda}^*(\omega)$, where $\hat{\lambda}(\omega)$ and $\hat{\lambda}^*(\omega)$ are the Fourier harmonic and the complex conjugate Fourier harmonic, respectively, of the particle distribution line density $\lambda(z/v)$. The power spectrum of bunches inside circular machines is composed of discrete lines, corresponding to multiples of the revolution frequency ω_0 , with a spectrum envelope whose width is inversely proportional to the bunch length. Thus the loss factor is given by the sum

$$k_{\parallel} = \frac{\omega_0}{2\pi} \sum_{p=-\infty}^{\infty} Z_{\parallel}(p\omega_0)h(p\omega_0). \quad (2.55)$$

As long as the spacing between the spectral lines is small compared to the scale of impedance variations, the infinite sums in eq. 2.55 can be replaced by integrals. For short bunches, a broad-band impedance can suffice for the calculation of the loss factor, because single resonances cannot be resolved in the time of a bunch passage. Narrow resonances can be important in the case of both long and short bunches, for example in multiple turn and in multiple bunch regimes, because if one of the beam spectral lines lies close to a resonance, electromagnetic fields can be excited coherently and the energy increases quadratically [23]. Thus the power spectrum will depend also on the bunch shape, i.e. on its rms length σ_z , so as the loss factor:

$$k_{\parallel}(\sigma_z) = \frac{1}{2\pi} \int_{-\infty}^{\infty} Z_{\parallel}(\omega)h(\omega, \sigma_z/v) d\omega. \quad (2.56)$$

Given the integral in the above equation extending over both negative and positive frequencies, it has to be taken into account that the product of an even function of frequency, as it is always the case for the power spectrum, and an odd one, as for the imaginary part of the impedance, does not contribute to the integral. So this latter can be calculated over the positive frequencies and the real part of the impedance only, as

$$k_{\parallel}(\sigma_z) = \frac{1}{\pi} \int_0^{\infty} \text{Re}\{Z_{\parallel}(\omega)\}h(\omega, \sigma_z/v) d\omega. \quad (2.57)$$

For a Gaussian bunch distribution, with rms bunch length σ_z and normalized linear density $\hat{\lambda}(\omega) = e^{-\omega^2\sigma_z^2/2v^2}$, the power spectrum is given by $h(\omega) = e^{-\omega^2\sigma_z^2/v^2}$, and the loss factor by

$$k_{\parallel}(\sigma_z) = \frac{1}{\pi} \int_0^{\infty} \text{Re}\{Z_{\parallel}(\omega)\}e^{-\omega^2\sigma_z^2/v^2} d\omega. \quad (2.58)$$

The longitudinal loss factor has the dimensions of V/C.

$V = -Z_{\parallel}I_b$, where $I_b = q\omega/2\pi$. Thus the voltage is proportional to the charge, and the energy change to its square.

A definition analogous to eq. 2.57, for the loss factor, holds for the transverse kick factor, but given the discussion at the beginning of section 2.4.3 about the parity of the longitudinal and transverse impedances, it results:

$$k_{\perp}(\sigma_z) = \frac{1}{2\pi} \int_{-\infty}^{\infty} Z_{\perp}(\omega) h(\omega, \sigma_z/v) d\omega = \frac{1}{\pi} \int_0^{\infty} \text{Im}\{Z_{\perp}(\omega)\} h(\omega, \sigma_z/v) d\omega. \quad (2.59)$$

Since $Z_{\perp}(\omega)$ is an impedance per unit transverse displacement, the dimensions of the kick factor are V/Cm. Again, for a Gaussian bunch distribution it results, following the same derivation of eq. 2.58, for the kick factor:

$$k_{\perp}(\sigma_z) = \frac{1}{\pi} \int_0^{\infty} \text{Im}\{Z_{\perp}(\omega)\} e^{-\omega^2 \sigma_z^2 / v^2} d\omega. \quad (2.60)$$

As already mentioned in the discussion leading to eq. 2.55, the bunch oscillation spectrum consists of many discrete lines, spaced by multiples of the revolution frequency ω_0 . For k_b equally spaced bunches, only the k_b^{th} line can be excited, spectral lines being spaced by $k_b \omega_0$, the bunch frequency. In a way analogous to the definition of loss factors for bunched beams, eq. 2.55, the effective impedance is the convolution of the coupling impedance and the bunch oscillation spectrum. It is the effective impedance that is responsible for the coherent stability of bunched beams.

The *effective longitudinal impedance* for the m^{th} bunch mode can be written as [30]

$$Z_{eff}^m = \sum_{p=-\infty}^{\infty} \frac{Z_{\parallel}}{n}(\omega_p) H_m(\omega_p), \quad (2.61)$$

where $\omega_p = \omega_0(k_b p + n_b + m\nu_s)$ are the spectral frequencies of a beam consisting of k_b bunches equally spaced, $\nu_s = \omega_s/\omega_0$ is the synchrotron tune and $0 \leq n_b < k_b$ is the coupled bunch mode number describing the phase shift $\Delta\phi = 2\pi n_b/k_b$ between bunches. In the above equation, $H_m(\omega) = C_m \hat{\lambda}(\omega) \hat{\lambda}^*(\omega)$ is the normalized spectral power density, with normalization constants C_m given by the condition $\sum_{p=-\infty}^{\infty} H_m(\omega_p) = 1$.

The *effective transverse impedance* for the m^{th} longitudinal mode of a dipole oscillation of a bunched beam, instead, can be written as [31]

$$Z_{eff}^{\perp m} = \sum_{p=-\infty}^{\infty} Z_{\perp}(\omega_p) H_m(\omega_p - \omega_{\xi}), \quad (2.62)$$

where the spectral frequencies for transverse oscillations are $\omega_p = \omega_0(p + n_b + m\nu_s + \nu_{\beta})$ and $\omega_{\xi} = \omega_0 \xi / \eta$ is the *chromatic frequency*, $\xi = \frac{P d\nu_{\beta}}{\nu_{\beta} dP}$ being the chromaticity, P the longitudinal particle momentum, $\eta = \alpha - 1/\gamma^2$ the slippage factor and α the momentum compaction factor⁹.

⁹All these quantities, in the context of an accelerator model like that shown in Fig. 2.1, are discussed in detail in Appendix A.

2.5 Collective effects

Collective effects include incoherent phenomena of many particles and coherent interactions of the beam with its surroundings. Both are dependent on the beam intensity and on the bunch filling patterns, being responsible of beam instabilities, parasitic losses, beam quality degradation due to emittance growth and poor lifetime of all or some specific bunches and radio frequency heating of the components surrounding the beam.

Single bunch and multibunch (or coupled bunch) instabilities may be driven by both broad-band and narrow-band impedances, depending on how these latter couple with the bunch spectrum lines. In the case of the LHC accelerator complex, a detailed impedance evaluation of all the structures installed around the beams has been carried out, in order to calculate the beam performances of the collider in the present configuration and for the future High Luminosity LHC upgrade [13, 14].

2.5.1 Single bunch

Single bunch collective effects arise from the interaction of a bunch with itself, when the generated wake fields have a range comparable to its length or shorter.

For longitudinal effects, an instability mechanism was already implicitly discussed in the previous section 2.4.6, about eq. 2.54, which is generally referred to as *parasitic heating*. It was shown that only the real (resistive) part of the impedance contributes to the parasitic loss. Inductive impedances, indeed, do not introduce a net energy loss to the beam, even if individual particles can change their energy because of it. However this individual particle energy loss lead to a compensation between the loss occurring at the head of the bunch and an energy recovery by particles in the tail, so apart from an energy transfer from the head to the tail of the bunch, the net effect on the entire bunch is that even if no energy is lost, an energy spread does appear. Parasitic heating is an effect occurring mainly for high beam intensities, for short bunches and also for long bunches with full coupling with an HOM. For instance, the longitudinal resistive wall impedance it is found [22] to be

$$\left. \frac{Z_0^{\parallel}}{n} \right|_{\text{RW}} = [1 - i \operatorname{sgn}(\omega)] \frac{R}{nb\sigma_c} \sqrt{\frac{\mu\omega\sigma_c}{2}}, \quad (2.63)$$

and the corresponding loss factor

$$\frac{k_{\parallel}(\sigma)}{L} = \frac{\Gamma(\frac{3}{4})c}{4\pi^2 b\sigma_z^{3/2}} \left(\frac{Z_0}{2\sigma_c} \right)^{1/2}, \quad (2.64)$$

where R is the mean radius of the accelerator ring, μ the magnetic permeability of the walls of the beam pipe of radius b , L is the pipe length, $\Gamma(\frac{3}{4}) = 1.225$ the Euler Gamma function, $Z_0 = \sqrt{\mu_0/\epsilon_0} = 377\Omega$ the impedance of free space, σ_c the continuous electric conductivity of the metal pipe wall and σ_z , as usual, the rms bunch length. Parasitic loss gives rise to heating of the vacuum chamber wall where there are impedances, i.e. as the beam traverses a discontinuity. Part of the generated wakefield is trapped by the structure, if this latter is cavity-like and the wake's frequency is below the pipe cutoff. The trapped field energy is deposited

as heat on the cavity walls, while the wake field portion with frequency above the cutoff propagates down the pipe and eventually deposits its energy on lossy materials elsewhere in the vacuum chamber. The most of the parasitic energy loss goes into heating of the vacuum chamber wall, only a small portion being transferred back to the beam motion. Thus under favorable conditions, parasitic heating can drive beam instabilities.

The *microwave instability* is one of the most commonly encountered in accelerator rings, but it is triggered more easily for electron machines than for hadron machine like the LHC. However it is useful to briefly discuss it, in order to introduce the concept of beam intensity threshold.

If the beam current is large enough to excite this instability, the induced effect is a bunch length and energy spread increase. At higher currents, indeed, exponential growth of the ripples caused by the high frequency components of the wake field in the longitudinal beam density can occur, leading to beam instability. Physically, a perturbation λ_1 of harmonic frequency Ω in the linear beam density causes a perturbation of the local revolution frequency ω_1 and the local beam current I_1 , having the same harmonic number $n = \omega/\omega_0$ and frequency Ω . The perturbed current I_1 interacts with the longitudinal impedance Z_0^{\parallel} and changes the particles' energy E , which in turn drives a change in its revolution frequency ω_1 . The longitudinal impedance, in other words, drives a longitudinal force that changes the revolution frequency. Under Boussard [32] conditions for bunched beams, i.e. the perturbing wavelength $\lambda_1 \ll \sigma_z$, the instability growth time $\tau \ll T_s$ the synchrotron period and the average beam current I_0 is substituted by the local peak current I_{pk} , the Keil-Schnell stability criterion [33], can be used to establish a threshold for the bunch current, as

$$eI_{pk}\beta^2 \left| \frac{Z_0^{\parallel}}{n} \right| \geq 2\pi E \sigma_\delta^2 |\eta| F_{dist}, \quad (2.65)$$

where $I_{pk} = F_B I_0$, $F_B = 2\pi R / \sqrt{2\pi} \sigma_z$ is the bunching factor, σ_z the usual rms bunch length, E the beam energy, η the slippage factor, σ_δ is the rms beam momentum spread and $F_{dist} \approx 1$ a factor that generally depends on the longitudinal beam distribution [23].

It is possible for wakefields to drive also coherent transverse oscillations within a single bunch. It is a more complicated situation with respect to the longitudinal case, because of the constant exchange of the head and tail of the bunch via longitudinal oscillations over a synchrotron period. This continuous exchange does not allow the growth of the oscillation amplitude of the tail to accumulate as quickly, thus extending the stability threshold. If the transverse wake fields are so intense that the growth time of the oscillation amplitude of the tail is less than half a synchrotron period, the bunch becomes unstable and is quickly lost. This mechanism is known as *transverse mode coupling instability* (TMCI), for which a threshold for the bunch current is given by

$$\left| \frac{eI_b \bar{\beta}_\perp Z_1^\perp |_{\text{eff}}^m}{2\beta E_0 \omega_s \tau_L} \right| \lesssim 1, \quad (2.66)$$

where $\bar{\beta}_\perp$ is some reference betatron function so that $Z_1^\perp |_{\text{eff}}^m$ retains the dimensions

of transverse impedance, E_0 is the average beam particle energy in the bunch and τ_L the total time length of the bunch from the head to the tail.

2.5.2 Multi-bunch

Wake fields whose range is long enough to couple the motion of the different bunches in the beam, can cause coupled bunch instabilities. As already discussed at the beginning of this section, these instabilities are driven by narrow-band impedances of high- Q resonators, like RF cavities. Even though they remain localized in the cavities, they last for a long enough time that the motion of any given bunch is perturbed by all its predecessors by means of transverse or longitudinal coherent structure in the bunch-by-bunch oscillations. If these coherent oscillations grow indefinitely, they lead to rapid beam loss, whereas if they remain bounded, they degrade the beam quality by inducing emittance growth.

Limiting the present brief discussion to dipole coupled bunch oscillations, these are characterized by the motion of the bunches about their nominal centers as if they were rigid macroparticles. The most basic longitudinal instability mechanism in the multi bunch regime is the *Robinson instability* [34], for which a very short physical picture is discussed here just for completeness, because the work described in the following chapters did not deal with it.

Robinson instability comes from the fact that the revolution frequency of an off-momentum beam is not simply given by ω_0 but by $\omega_0(1 - \eta\delta)$, where $\delta = \Delta E/E$ is the relative energy error. Considering a beam executing synchrotron oscillation above transition, due to an energy error of the beam, the longitudinal impedance will sample the beam signal at a frequency slightly below $h\omega_0$, h being the harmonic number, if $\delta > 0$ and slightly above $h\omega_0$ if $\delta < 0$. In order to damp this synchrotron oscillation of the beam, it is needed to let the beam lose energy when $\delta > 0$ and to gain energy when $\delta < 0$. This can be achieved with an impedance that decreases with increasing frequency in the neighborhood of $h\omega_0$, and from these considerations follows the Robinson stability criterion for the instability growth rate [22]

$$\tau^{-1} = \text{Im}\{(\Omega - \omega_s)\} = \frac{Nr_0\eta}{2\gamma T_0^2\omega_s} \sum_{p=-\infty}^{\infty} (p\omega_0 + \omega_s) \text{Re}\{Z_0^{\parallel}\}(p\omega_0 + \omega_s), \quad (2.67)$$

where, apart from the recurrent terms already specified in the above discussions, N is the number of particles in the beam and r_0 is the classical radius of the beam particle type. Thus, it is the real part of the impedance that contributes to the instability growth rate (the imaginary part contributing to the collective frequency shift of the beam).

The *Transverse Coupled Bunch Instability* (TCBI) is driven by narrow-band dipole HOMs of RF cavities and also by the resistive wall impedance. For low frequencies, the skin depth is relatively large and hence the wake field can last for a sufficiently long time to couple the motion of different bunches. The transverse dipole resistive wall impedance is found to be [22]

$$Z_1^{\perp} = \frac{2c}{b^2\omega_0} \frac{Z_0^{\parallel}|_{\text{RW}}}{n}, \quad (2.68)$$

being b , as usual, the beam pipe radius. The transverse complex frequency shift for coupled bunch mode l and dipole head-tail mode (rigid bunch shape) is given by

$$\Delta\Omega_{\parallel}^l = -i \frac{\omega_0 I_0 \beta_{\perp}}{4\pi E/e} Z_{eff}^{\perp l}, \quad (2.69)$$

in which $Z_{eff}^{\perp l}$ is the transverse effective impedance given by eq. 2.62. In the case of a single high- Q resonator tuned near the frequency $pM\omega_0$, with zero chromaticity and a bunch length which is short with respect to the resonant wavelength of the resonator, the growth rate is given by

$$\frac{1}{\tau_{\perp,l}} = \frac{\omega_0 I_0 R_{eff}^{\perp,l}}{4\pi(E/e)}, \quad (2.70)$$

in which

$$R_{eff}^{\perp,l} = -\beta_{\perp} \operatorname{Re} \left\{ \left\{ Z_1^{\perp}[\omega_0(pM + l + \nu_{\beta})] - Z_1^{\perp}[\omega_0(pM - l - \nu_{\beta})] \right\} \right\}. \quad (2.71)$$

Chapter 3

LHC Run I TCS-TCT collimators

For LHC, the betatron tune shifts and instability growth rates can be estimated by means of beam dynamics simulations and the machine impedance model. Beam dynamics simulations are carried out with analytical models or the multi-bunch code HEADTAIL. Up to 2012, the LHC impedance model accounted for RW impedance from collimators, beam-screens, vacuum pipe and broad-band model from the design report [35]. As a reference for the following impedance study, the various contributions to the transverse vertical dipolar impedance is shown in Fig. 3.1, where it is clearly seen that the collimators are among the main contributors, playing the major role ($\sim 90\%$) over a wide frequency range, both for real and imaginary parts. [36].

In June 2012 single bunch tune shifts were measured, as an indirect measurement of beam-based impedance. Measurements were performed with 8 bunches filling the machine, some of them having different intensities. Being them equally spaced along the LHC ring, the influence of neighboring bunches on tune shifts was considered negligible, that is why such measured quantities are considered as single-bunch tune shifts. Thus, tune shifts vs. intensity were measured, both at injection ($E = 450$ GeV) and at flat top ($E = 4$ TeV) [37]. A specific measurement was also performed for several collimator families (secondary collimators in IR7, TCSG, and primary collimators always in IR7, TCP) all at top energy, giving their tune shifts upon moving back and forth the jaws [38]. The experimental results for both the measurements sessions are shown in Fig. 3.2 and Fig. 3.2, as the ratio of the measured tune slope vs. intensity to the numerical simulations results from HEADTAIL, which used the wake fields from the LHC impedance model. The abscissa labels B1 and B2 stay for beam 1 and beam 2, respectively, and the H or V letters indicate the horizontal or vertical planes. The measured tune shifts are higher than predicted ones by a factor of ~ 2 at top energy and of ~ 3 at injection [39]; so the existing LHC impedance model accounted only for a fraction, $\sim \frac{1}{3} - \frac{1}{2}$, of the measured transverse coherent tune shifts. This fact led to the need for an LHC impedance model refining which, first of all, required a careful collimator geometric impedance calculation. For instance, it was approximated only by that of a round circular taper.

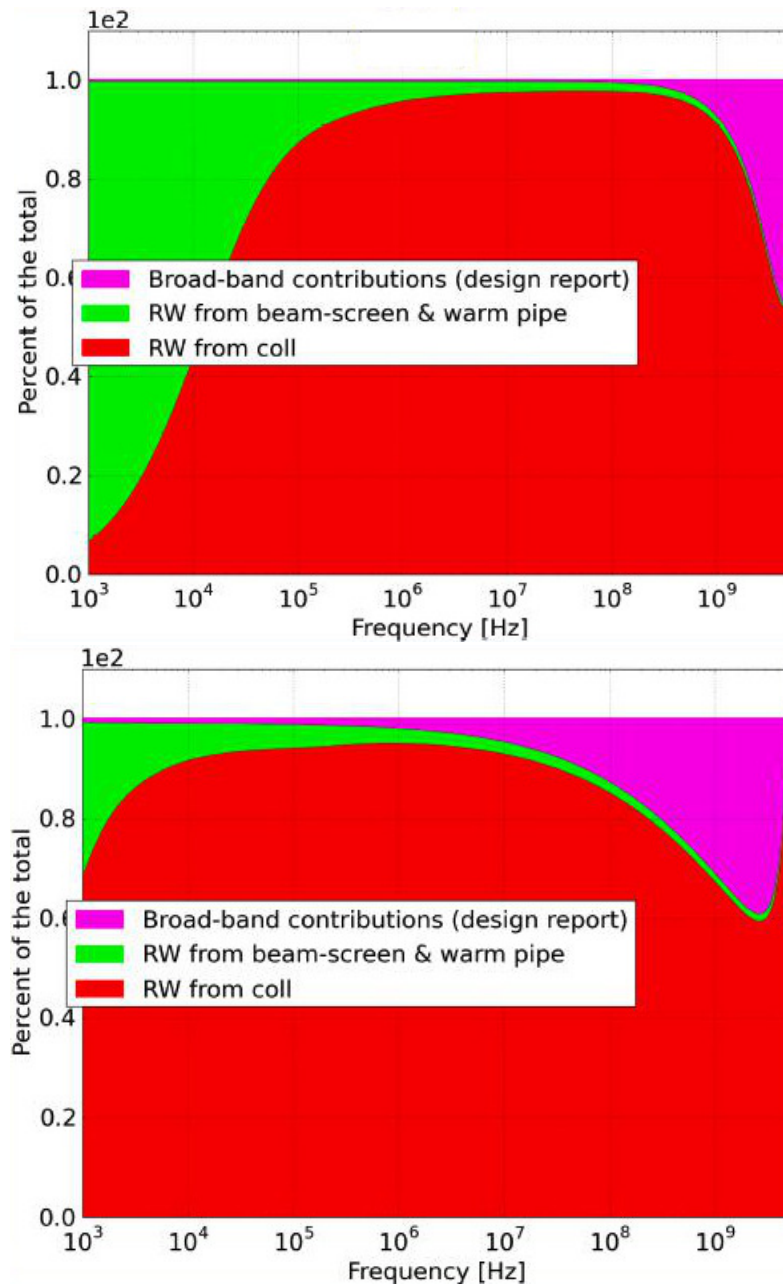


Figure 3.1. Real (up) and imaginary (down) parts of the 2012 LHC vertical dipolar impedance model.

For this purpose, numerical calculations of the geometric impedance of the LHC secondary collimator TCS were carried out, as close as possible to its real design and evaluated the collimator contribution to the overall LHC impedance budget. CAD drawings including all the mechanical details were used as inputs for the high performing, parallelizable, UNIX-platform FDTD GdfidL code¹ [40]. A very fine

¹For an overview of the general method used by the code to solve Maxwell equations, see Appendix B.

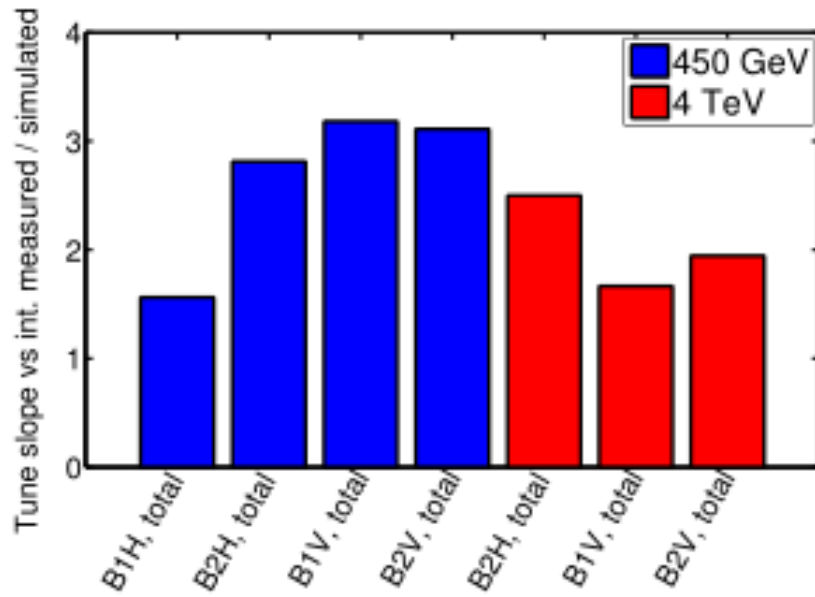


Figure 3.2

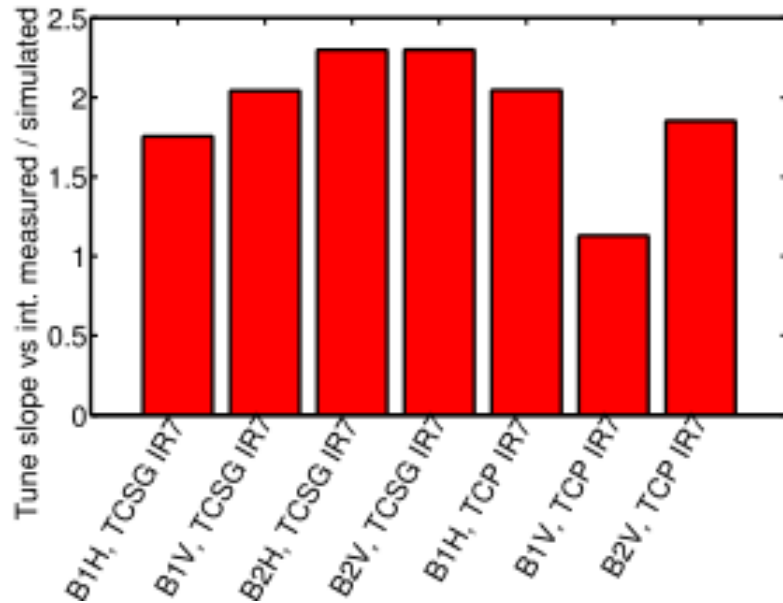


Figure 3.3

mesh, typically, of several billions mesh points, was required to reproduce the long and complicated structures, described in huge Stereo Lithography interface format (STL) files, and to overcome arising numerical problems. As an accuracy criterion, indeed, it is recommended that for structures with long tapers (14.7 cm, in the case of LHC RUN I TCS/TCT) the following relations hold [41]:

$$\frac{a\phi}{\Delta z} \cdot \frac{\sigma_z}{\Delta z} \geq 100, \quad (3.1)$$

in which a is the pipe radius ², ϕ the tapering angle, σ_z the bunch length and Δz the mesh size in the specified direction (here z for axially symmetric structures, but it can be also any of the other two transverse directions, x or y , depending on how much finely the discontinuities in that direction must be resolved). In the case under study, given the very complicated structure and small discontinuities of the collimator jaws, a mesh size of 0.2 mm in all three directions was used, leading to a very huge computing task.

The only way to afford such a huge computational task was to use the GdfidL dedicated cluster at CERN, *EngPara*, which allowed to study the wake fields and impedances for of LHC collimators without using any model simplifications. In such circumstances, GdfidL wake fields computations up to wake length of hundreds times the typical devices lengths (~ 1 m) took several days or two weeks at maximum (15 days is, however, the user runtime limit on *EngPara*).

3.1 Theoretical considerations

In order to verify whether the geometric collimator impedance can give a noticeable contribution to the betatron tune shifts, the suggestion exploited in this thesis was to compare transverse kick factors due to the resistive wall impedance and the geometric one. First of all, as shown below, the tune shifts are directly proportional to the kick factors. Besides, this approach has several advantages: 1) it is a quite straightforward way to compare contributions from impedances having different frequency behaviour into the transverse tune shifts; 2) only calculations of the broad band wakes are necessary without the exact knowledge of the transverse impedance $Z_T(\omega)$; 3) both kick factors and broad-band impedances are easily calculated by many numerical codes.

The well known expression for the coherent mode tune shifts can be found in [31],

$$\Delta\omega_{c_m} = j \frac{1}{1 + |m|} \frac{I_c^2}{2\omega_0 Q(E/e)L} \frac{\sum_p Z_T(\omega_p) h_m(\omega_p - \omega_\xi)}{\sum_p h_m \omega_p - \omega_\xi}, \quad (3.2)$$

where $\Delta\omega_{c_m}$ is the shift of the angular frequency of the m^{th} transverse coherent mode, with m being the azimuthal mode number, ω_0 the angular revolution frequency, I_c is the average bunch current, Q the betatron tune, E the machine energy, L is the full bunch length and $\omega_\xi = \omega_0 \frac{\xi}{\eta}$ is the ‘‘chromatic’’ angular frequency, with ξ being the chromaticity and η the slippage factor of a circular accelerator. For a given mode m , the bunch power spectrum for a Gaussian bunch, with rms bunch length σ_z , is given by:

$$h_m(\omega) = \left(\frac{\omega \sigma_z}{c} \right)^{2|m|} e^{-\left(\frac{\omega \sigma_z}{c} \right)^2}. \quad (3.3)$$

Given the sum in Eq. 3.2 being performed over the mode spectrum lines

$$\omega_p = (p + \Delta Q)\omega_0 + m\omega_s \quad ; \quad -\infty < p < +\infty \quad (3.4)$$

²For axially symmetric structures. For rectangular flat ones, like the TCS/TCT jaws, it can be considered as the half gap between the beam axis and the jaw.

where ΔQ is the fractional part of the betatron tune and ω_s is the angular synchrotron frequency, it results that the tune shifts are real if the imaginary transverse impedance, $\text{Im}\{Z_T(\omega_p)\}$, differs from zero. For $\xi = 0$ and dipole coherent mode ($m = 0$) we get a proportionality relation:

$$\Delta\omega_{c_0} = -const \cdot I_c \sum_p \text{Im}\{Z_T(\omega_p)\} e^{-\left(\frac{\omega\sigma_z}{c}\right)^2}. \quad (3.5)$$

On the other hand, from kick factor definition, we have

$$k_T = \frac{1}{2\pi} \int_{-\infty}^{\infty} \text{Im}\{Z_T(\omega)\} e^{-\left(\frac{\omega\sigma_z}{c}\right)^2} d\omega \quad (3.6)$$

so that, comparing Eq. 3.6 with Eq. 3.5, we find

$$\Delta\omega_{c_0} \propto -k_T \quad (3.7)$$

In what follows the impedance theory developed in [35] is used, in order to evaluate the kick factors due to the wall resistivity.

3.1.1 Geometric and resistive wall kick factors evaluation

The geometric kick factors are easily returned by the code computations. For a smooth taper, indeed, it can be shown [42] that:

$$k_T = \int_0^{\infty} G\left(\frac{\omega}{c}\sigma_z\right) \text{Re} Z_T(\omega) d\omega - \frac{c}{2\pi^{1/2}\sigma_z} \text{Im} Z_T(0), \quad (3.8)$$

where, apart from the obvious meanings of ω , σ_z and c , G is a weighting function introduced for convergence purposes. From the above equation, one can easily argue that if $\text{Re} Z_T(\omega) \ll \text{Im} Z_T(\omega)$, then $k_T \propto \text{Im} Z_T(0)$ which is a very advantageous relation because calculation of $\text{Im} Z_T(0)$ is much easier to perform than $Z_T(\omega)$, involving only solutions of Maxwell equations for static fields.

In order to evaluate RW kicks [29], the thick wall impedance of a flat vacuum chamber [43] can be considered, with $2a \cdot 2b$ cross section:

$$\frac{Z_{T_y}}{L} = \frac{(1+j)Z_0\delta}{2\pi b^3} F_{1y}\left(\frac{b}{a}\right). \quad (3.9)$$

So,

$$Z_{T_y} = \frac{L(1+j)Z_0\delta}{2\pi b^3} F_{1y}\left(\frac{b}{a}\right) = \frac{LZ_0\delta}{2\pi b^3} F_{1y}\left(\frac{b}{a}\right) + j \frac{LZ_0\delta}{2\pi b^3} F_{1y}\left(\frac{b}{a}\right)$$

and

$$\text{Im} Z_T = \text{Im} Z_{T_y} = \frac{LZ_0\delta}{2\pi b^3} F_{1y}\left(\frac{b}{a}\right). \quad (3.10)$$

Substituting (3.10) into (3.6) and after some simple algebra, it is found:

$$k_T = \frac{L}{2\pi^2 b^3} \sqrt{2c\rho Z_0} F_{1y}\left(\frac{b}{a}\right) \int_0^{\infty} \frac{1}{\sqrt{\omega}} e^{-\frac{\omega^2 \sigma_z^2}{c^2}} d\omega,$$

where $\int_0^{\infty} \frac{1}{\sqrt{\omega}} e^{-\frac{\omega^2 \sigma_z^2}{c^2}} d\omega$ is an Euler Γ function

$$\Gamma(z) = \int_0^{\infty} e^{-t} t^{z-1} dt,$$

with $z = 0$. So that:

$$\int_0^{\infty} \frac{1}{\sqrt{\omega}} e^{-\frac{\omega^2 \sigma_z^2}{c^2}} d\omega = 2\Gamma\left(\frac{5}{4}\right) \frac{1}{\sqrt{\frac{\sigma_z}{c}}}$$

and

$$k_T = \frac{L}{2\pi^2 b^3} \sqrt{2c\rho Z_0} F_{1y}\left(\frac{b}{a}\right) 2\sqrt{\frac{c}{\sigma_z}} \Gamma\left(\frac{5}{4}\right) \quad (3.11)$$

For a flat rectangular vacuum chamber, the form factor

$$F_{1y}\left(\frac{b}{a}\right) = \frac{\pi^2}{12}$$

and, finally, the RW contributions:

$$k_T = \frac{Lc}{12b^3} \sqrt{\frac{2Z_0\rho}{\sigma_z}} \Gamma\left(\frac{5}{4}\right) \quad (3.12)$$

Just as remark, note that the same type of calculations hold for $Z_T^x(\omega)$ but taking into account that $F_{1x}\left(\frac{b}{a}\right) = \frac{\pi^2}{24}$, so leading to a weaker vertical kick.

3.2 Numerical calculations

The geometric wakefields and impedances simulations were performed by means of GdfidL, assuming all metallic surfaces perfectly conducting.

As earlier mentioned, the need to simulate the collimator as close as possible to its real design, led to the usage of the collimator CAD drawing, shown in Fig. 4.10(a) (left), including all mechanical details as GdfidL input file. The picture in Fig. 4.10(a) (right) shows the details of the collimator internal structure as reproduced by GdfidL.

The numerical studies have shown that the collimator broad-band impedance is dominated by the impedance of the flat elliptical collimator tapers, the closest to the beam. It is noteworthy to say that the difference in impedance between the round and the flat rectangular tapers can be very large, being proportional to the ratio of the horizontal to the vertical size [44]. The real taper is elliptical in the case under study (see, for example, Figure 2 in [45]), with high ratio of the horizontal to the vertical size. That is why it is better modeled by the flat rectangular taper formula.

In Fig. 4.11³ (left picture) a comparison between the low frequency transverse impedance provided by GdfidL as a function of the collimator half gap and by the

³In both plots of Fig. 4.11 solid and dotted smoothed lines join the five computed points for the five different half gaps.

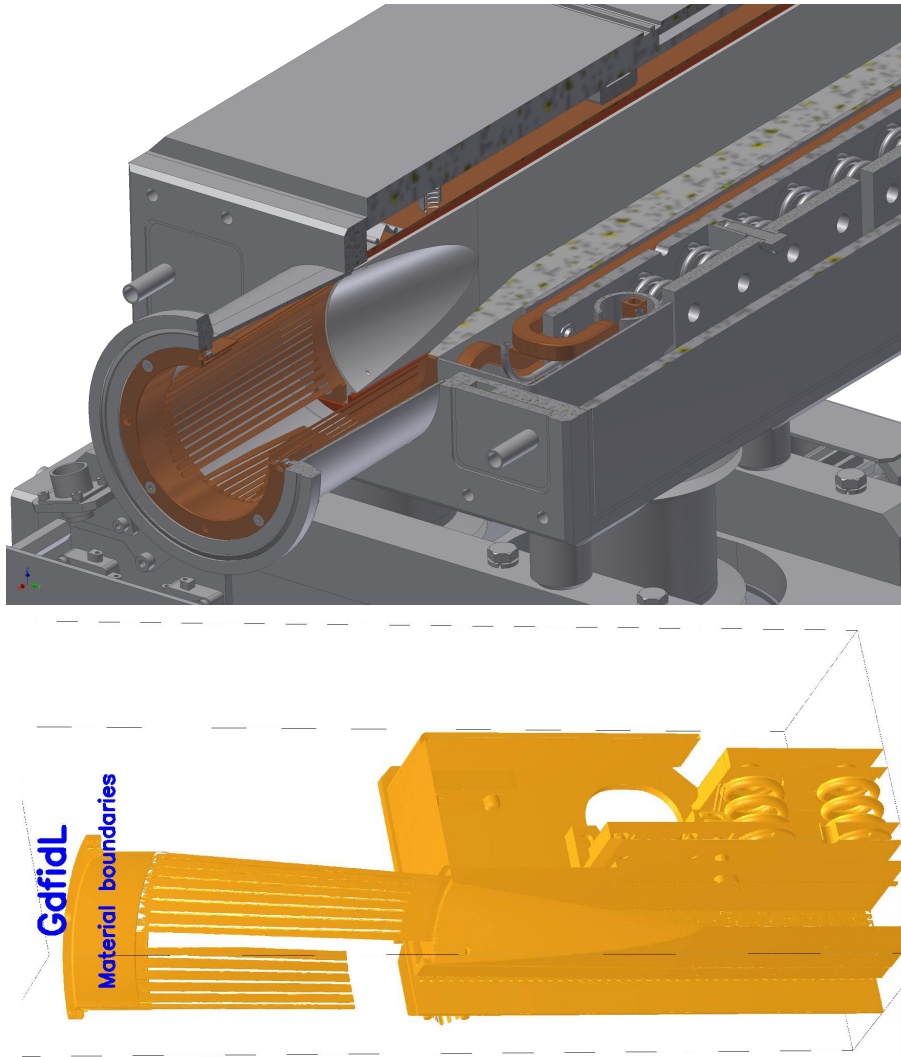


Figure 3.4. Collimator CAD design (left) and internal structure as reproduced by GdfidL (right).

analytical impedance formulas is reported. For a round taper [46] the transverse impedance is given by

$$Z_T = j \frac{Z_0}{2\pi} \int \left(\frac{b'}{b} \right)^2 dz, \quad (3.13)$$

where $Z_0 = 377 \Omega$, b is the variable taper radius and b' its derivative with respect to z . For a flat rectangular taper [44] the transverse impedance is

$$Z_T = j \frac{Z_0 w}{4} \int \frac{(g')^2}{g^3} dz, \quad (3.14)$$

where w is the taper constant width in the transverse vertical direction, g the taper variable gap and g' its derivative with respect to z . In both Eq. 3.13 and Eq. 3.14, the integration is performed over the taper length. The width of the jaws where the taper is carved is 74 mm to be compared with the typical collimator gap g of few

millimeters in operating conditions. What is obtained is a kind of a broad-band

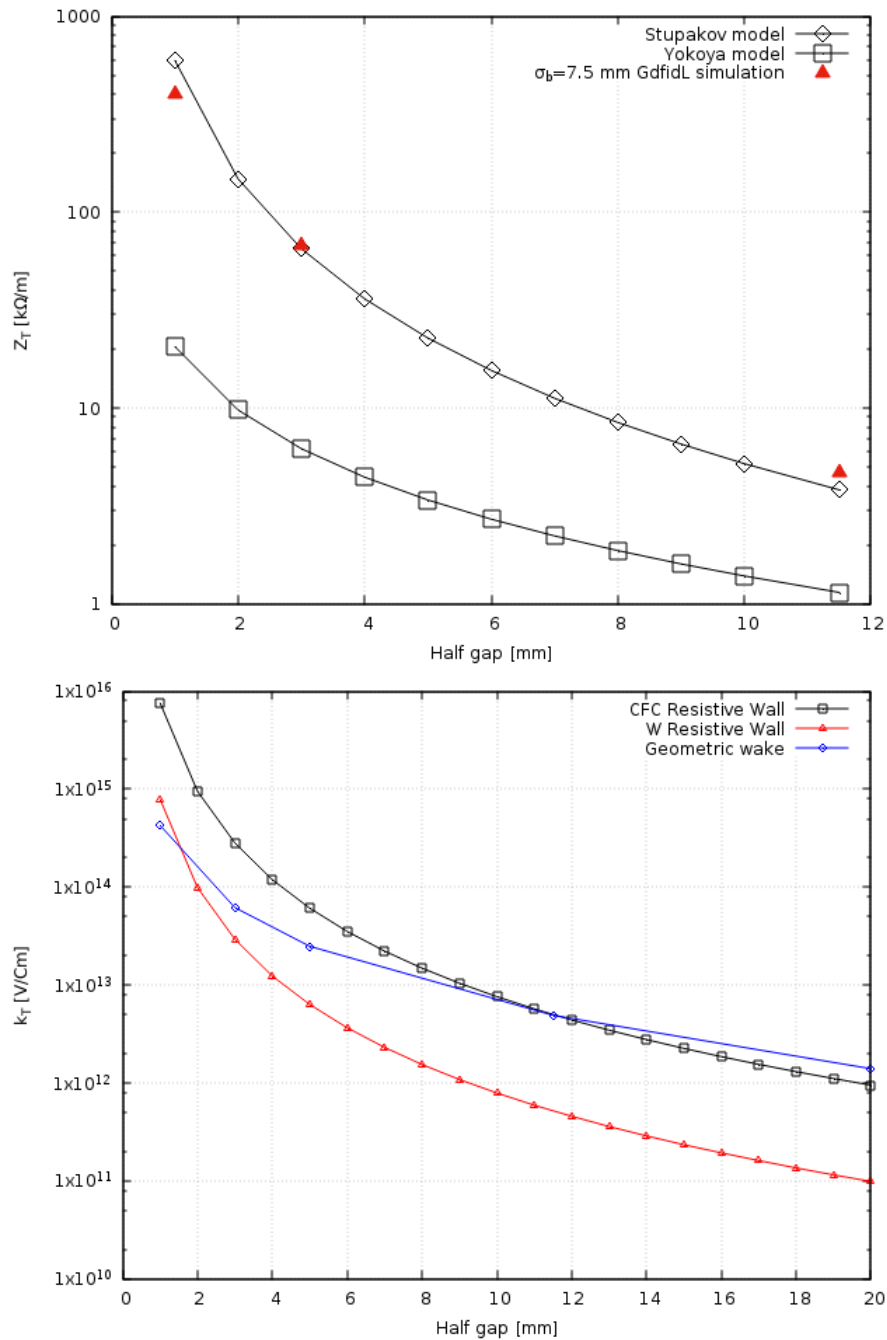


Figure 3.5. GdfidL results for LHC collimator's low frequency broad-band transverse effective impedance (left) and kick factors' comparison (right).

impedance, since at some point the wake was truncated and its Fourier transform performed. This makes the “effective impedance” bunch length dependent. For the nominal LHC bunch length of 7.5 cm, the whole bunch spectrum stays below the beam pipe cutoff, so remaining inductive. That is why the analytical formula comes

back to describe it finely.

Since the jaws' taper represent the closest discontinuity to a beam, it can be expected that the taper would give the dominant impedance contribution. Due to the fact that the collimator taper has a very flat geometry, the available analytical formula for a low frequency transverse impedance of a rectangular taper, Eq. 3.14, should give a reasonable estimate of the impedance in this case. Indeed, as it is seen on the left plot of Fig. 4.11 (upper curve), the calculated low frequency impedance of the complicated collimators' structures is very well approximated by the rectangular taper formula Eq. 3.14. The analytical formula for a round taper Eq. 3.13, instead, used in the early LHC impedance model, drastically underestimates the taper impedance (lower curve on the left plot of Fig. 4.11).

On the right side of Fig. 4.11, finally, the comparison between the geometric kick factors and the resistive wall ones, both for Carbon Fiber Composite (CFC) and Tungsten (W) made collimators' jaws, is reported, always as a function of the half gap. As a result, for W collimators geometrical impedance contribution dominates in almost the whole range of half gaps (from 1.5 mm onward), while only from about 8 mm onward for CFC collimators. Even considering the partial contribution in the case of CFC, it is evident that the geometrical impedance is not negligible with respect to resistive wall one.

Both the transverse and longitudinal impedances exhibit many resonant peaks at different frequencies. These higher order modes (HOM) are created in the collimator tank, trapped between the sliding contacts in the tapered transition etc., with parameters depending very much on the collimator gap. As an example, Fig. 3.6 shows the longitudinal impedance for two different collimator gaps. We found out that the HOM parameters obtained in our simulations, such as HOM frequency patterns, their strength and dependence on the gap width are very similar to those obtained in earlier works with simpler collimator model [47, 48, 49]. The modes shunt impedances are relatively small compared to typical HOMs in RF cavities. However, possible additional RF losses and related collimator structure heating due to these modes, in the conditions of higher circulating currents in High Luminosity LHC, still deserve a deeper investigation.

Finally, in order to allow beam dynamics studies by means of particle tracking codes, detailed longitudinal and transverse dipolar and quadrupolar wake fields calculations were carried out for 5 different collimator jaws' half gaps, namely 1 mm, 3 mm, 5 mm, 11.5 mm and 20 mm. For this purpose the bunch length was just 2 mm, instead of the 7.5 cm long LHC nominal bunch length, and the wake field was traced over 1 m. These wake potentials can approximate "point-like" wake functions for multi-particle tracking codes. In the following Fig. 3.7 and Fig. 3.9 the longitudinal and dipolar transverse wake potentials, computed by GdfidL, for 1 mm and 20 mm collimator jaws' half gaps is reported.

3.3 LHC impedance model update

The study described above contributed to the effort in updating the LHC impedance model, a process that took into account several improvements, namely the evaluation of the geometric impedance of the collimators as explained above, a full revision of

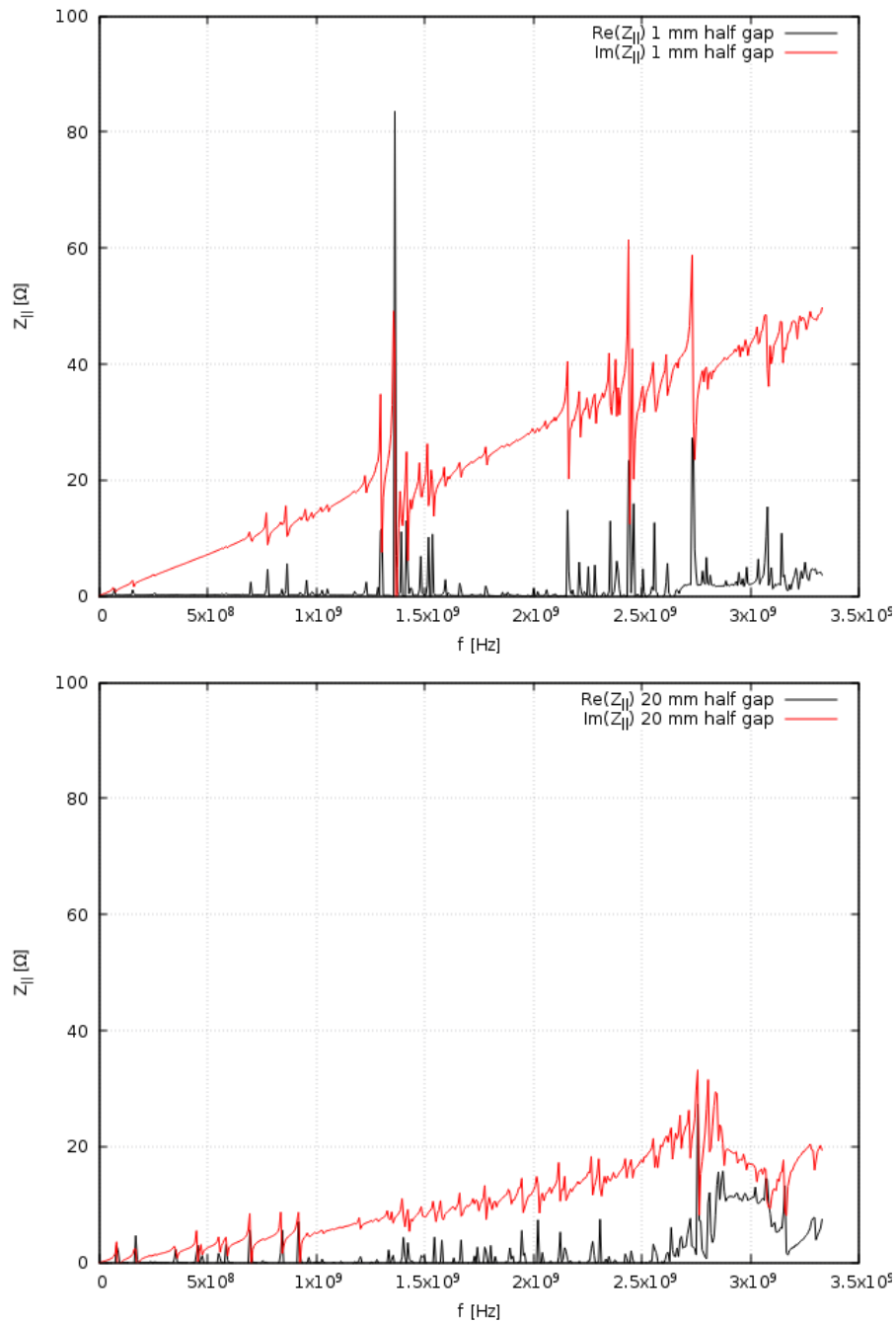


Figure 3.6. Real and imaginary parts of the longitudinal impedance for (left) 1 mm and (right) 20 mm half gaps.

the resistive wall model of the beam screens and the warm vacuum pipe, a theoretical re-evaluation of the impedance of the pumping holes, the inclusion of details of the triplet region (tapers and BPMs) and the broad-band and High Order Modes (HOMs) of the RF cavities, CMS, ALICE and LHCb experimental chambers [50].

Comparing the old and the updated models, a quite common impedance behaviour

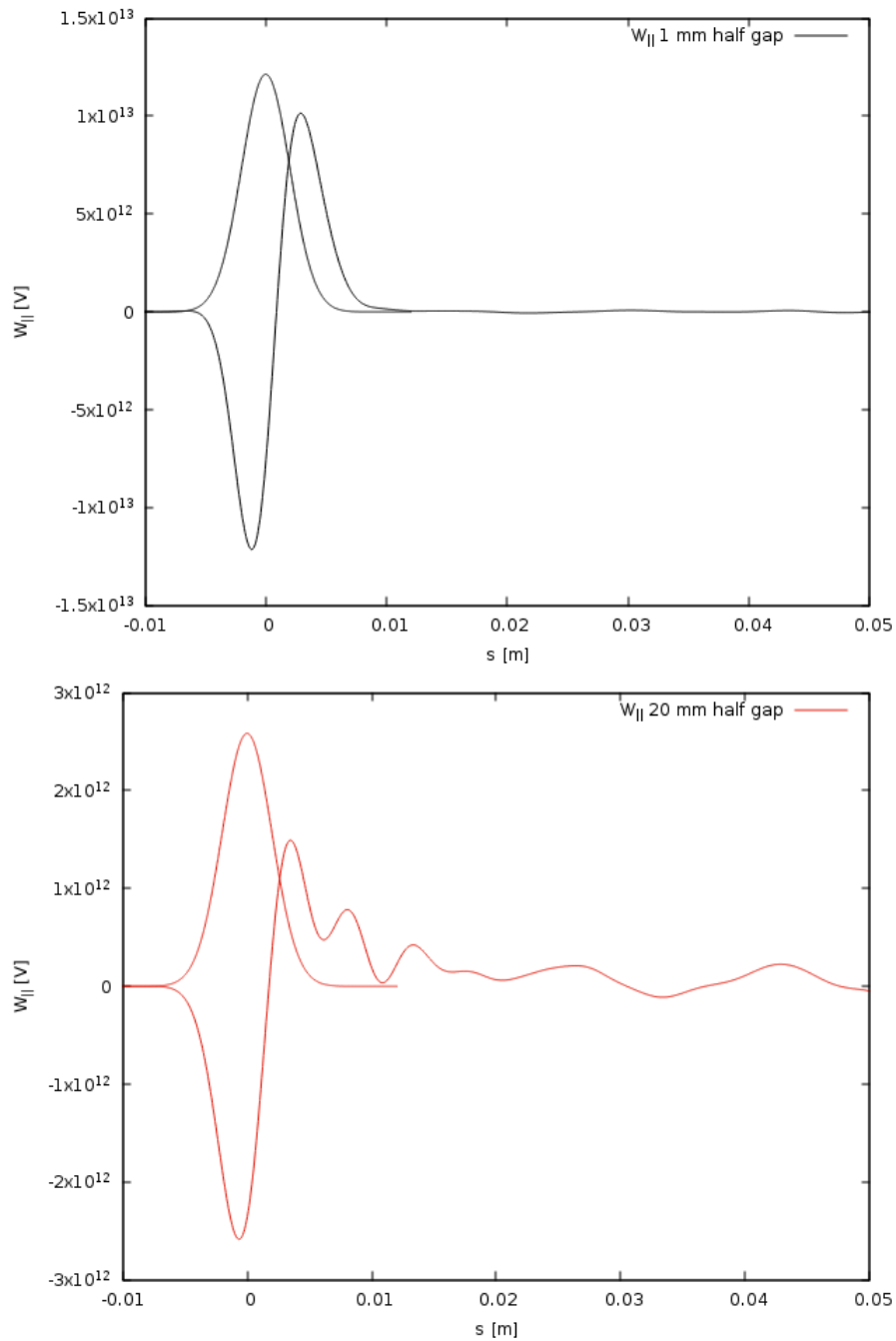


Figure 3.7. Longitudinal wake potentials for (left) 1 mm and (right) 20 mm half gaps, calculated for 2 mm bunch length. The wake is traced over 1 m length, as reported in the text, but here we focus the plots on the first 5 cm in order to highlight the main differences in wake trends.

at low frequency and a consistent increase ($\sim 30\%$) at frequencies close to 1 GHz for the latter, can be assessed [51, 52]. This should explain a part of the factor 2 discussed at the beginning of the chapter.

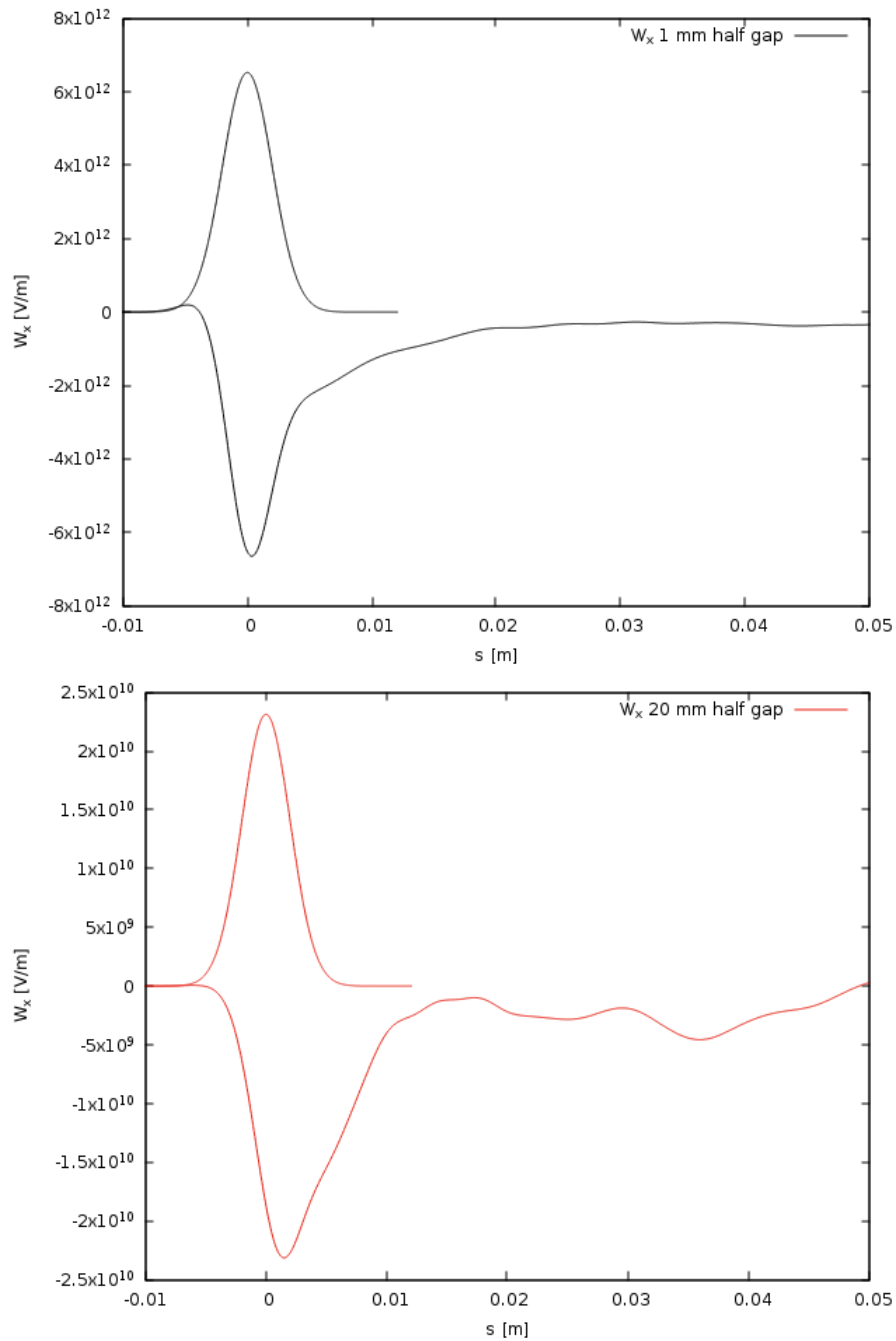


Figure 3.8. Dipolar transverse (down) wake potentials for (left) 1 mm and (right) 20 mm half gaps, calculated for 2 mm bunch length. The wake is traced over 1 m length, as reported in the text, but here we focus the plots on the first 5 cm in order to highlight the main differences in wake trends.

Since the equation 3.2 for the coherent mode tune shifts uses the impedance convolution over the bunch spectrum (all frequencies starting from 0), the contribution to the tune shift is expected to be smaller. The new DELPHI simulations performed

according to the new data for collimators [50], indeed, show an increase of at most $\sim 15\text{--}20\%$, as an effect of geometric impedance. However the impedance near 1 GHz may more strongly affect other beam dynamics aspects, e.g. TMCI threshold, since the different modes in the spectrum probe different frequencies in a different manner. The impact of the geometric impedance on the whole transverse dipolar impedance LHC model is clearly visible in Fig. 3.9, where the various percentile contributions are shown. A direct comparison between the previous and the updated impedance

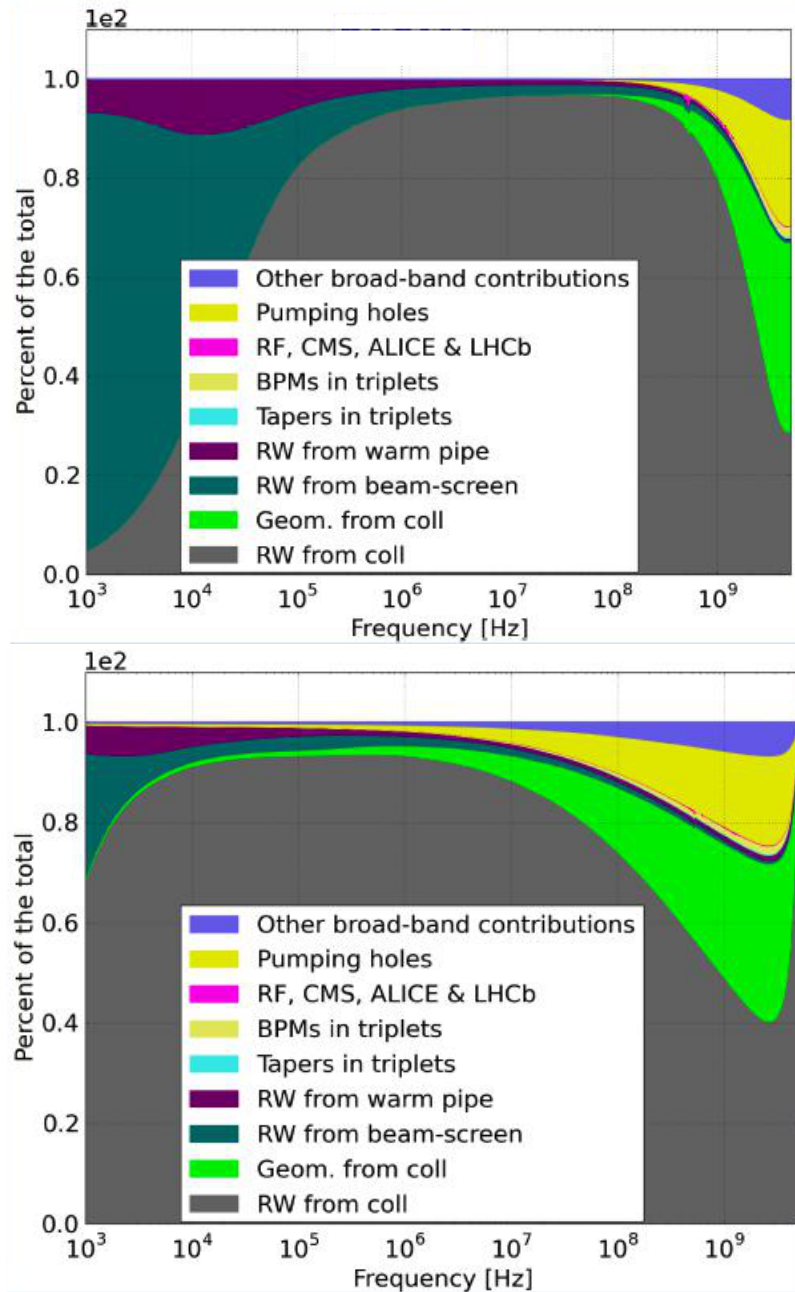


Figure 3.9. The updated LHC dipolar vertical impedance model real (left) and imaginary (right) parts.

models is reported in the plot of Fig. 5.7, for the vertical dipolar impedance. No differences are shown in the low frequency impedance up to ~ 100 MHz, whereas a visible increase occurs at high frequencies, up to ~ 20 GHz.

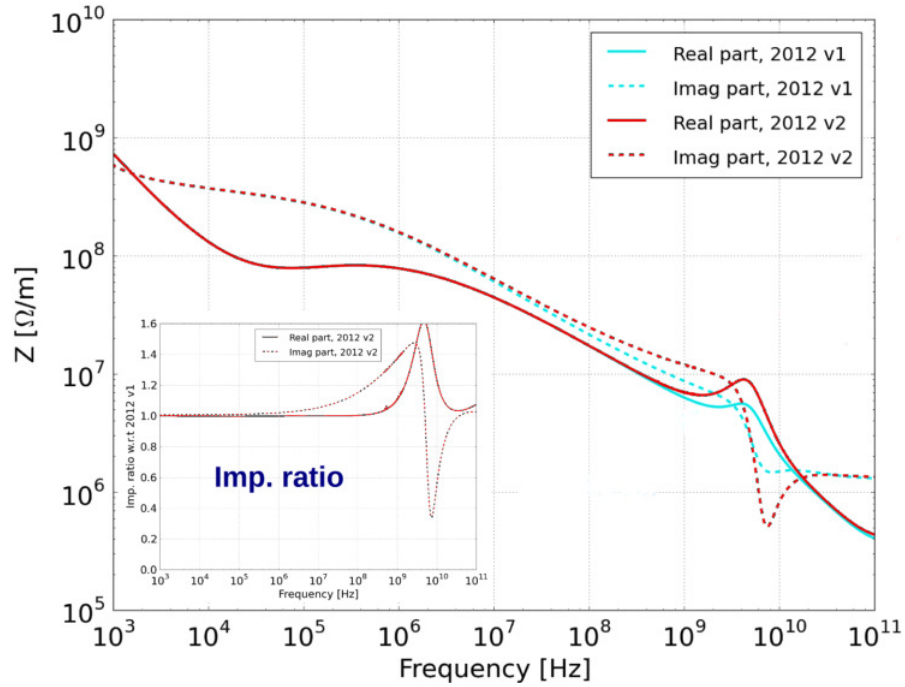


Figure 3.10

Chapter 4

Simulation tests of resistive and dispersive properties of materials in GdfidL

In view of LHC Run II and future high luminosity LHC upgrades, 2 old CFC TCS and 16 W TCT collimators were replaced, during the LSI, by new devices embedding BPMs in the jaws' tapering region and TT2-111R ferrite blocks in place of old transverse RF fingers (Fig. 5.7) [53]. This new collimator's design will be illustrated in detail in the next chapter, together with its impedance study. What is important to say here, is that in order to characterize the collimator in terms of impedance, to accurately predict its HOMs pattern and the effect of different materials in HOMs damping, a full reliability on the electromagnetic code computations of wake fields and impedances in presence of resistive and dispersive materials, must be assessed.

Several dedicated tests have been performed to verify correct simulations of lossy dispersive material properties, such as resistive wall and ferrites, benchmarking code results with analytical, semi-analytical and other numerical codes outcomes.

4.1 RW simulation tests

Only recently¹ a possibility to carry out simulations with resistive walls (RW), implementing the Impedance Boundary Conditions (IBCs), was made available in GdfidL. So it has been decided to perform numerical tests comparing the simulation results with known analytical formulas.

4.1.1 Resistive cylindrical pipe

As a first benchmark, the longitudinal wake of a very simple geometry, a cylindrical pipe with two different boundary material electrical conductivities, $5.8824 \cdot 10^7$ S/m for Cu and $1.7857 \cdot 10^7$ S/m for W, was simulated. Results were compared to well established theory for longitudinal RW of uniform cylindrical pipes [22], in which

¹The GdfidL version implementing IBC was first released on June 22nd, 2014.

the impedance function is written as:

$$Z(k) = -L \frac{Z_0}{2\pi b} \left[\frac{\nu}{k_0} + j \frac{k_0 b}{2} \right]^{-1}, \quad (4.1)$$

where $\nu = \sqrt{-j\omega\mu\sigma_c}$, $k_0 = \frac{\omega}{c}$, $b = R$, R being the pipe radius. In the case under study a geometry with $L = 50$ cm, $R = 2.8$ cm, with a mesh size of 0.5 mm and bunch length $\sigma_z = 3$ cm was chosen, as illustrated in Fig. 4.1. Those values for pipe and bunch lengths were set in order to avoid computation above the pipe cutoff frequency, for the fundamental TM_{01} mode, which in this case is ≈ 4.1 GHz.



Figure 4.1. The simulated pipe geometry.

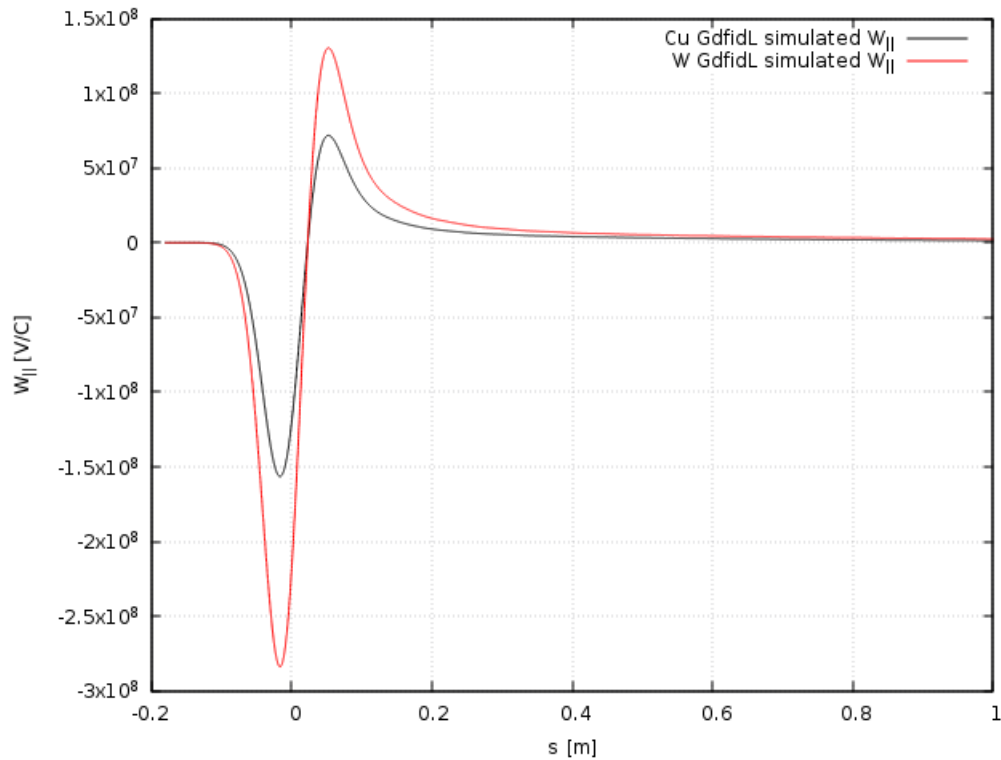


Figure 4.2. Longitudinal wake field for copper (black line) and tungsten (red line) pipe, as simulated with GdfidL.

In Fig. 4.2 the computed longitudinal wake field is plotted, for Cu and W. The lower electrical conductivity of W gives rise to a stronger RW wake field, with respect

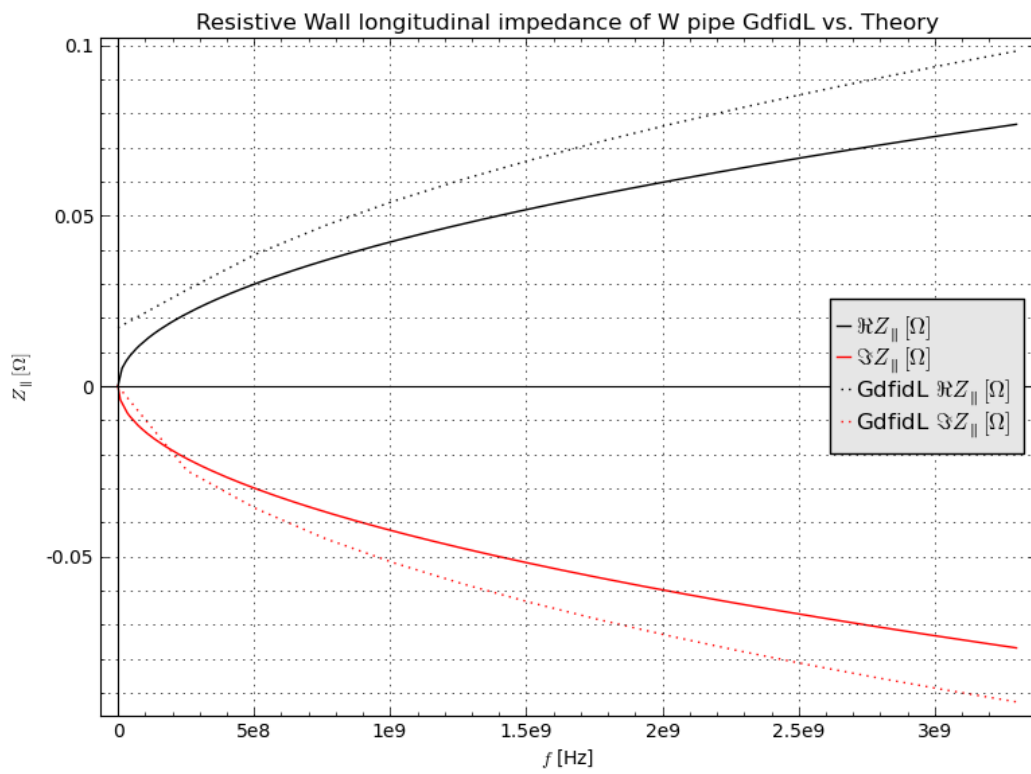
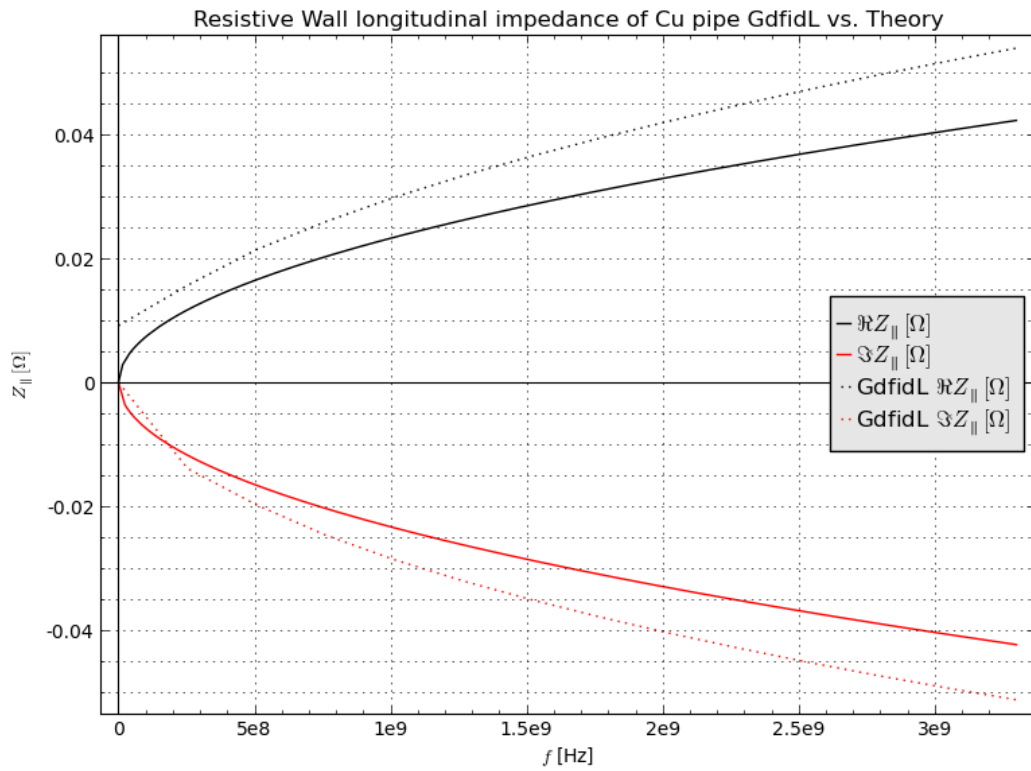


Figure 4.3. Comparison between analytical and GdfidL-simulated RW longitudinal impedance, for (a) copper and (b) tungsten pipes.

to that of Cu, as physically expected. This is obviously reflected in the longitudinal RW impedance also, as shown in Fig. 4.3(a) and Fig. 4.3(b), where the real and imaginary parts of the impedance are shown in black and red colours, respectively, and the numerical results in solid lines are compared to theoretical calculations based on eq. 4.1, in dotted lines.

In Table 4.1 a comparison between simulated and theoretical longitudinal impedance and loss factor values is reported. As a result of this benchmark it

	Cu Re $Z_{\parallel}(1 \text{ GHz})$	W Re $Z_{\parallel}(1 \text{ GHz})$	Cu $ k_{\parallel} $	W $ k_{\parallel} $
GdfidL	0.029 Ω	0.054 Ω	$72.4 \cdot 10^6 \text{ V/C}$	$131.5 \cdot 10^6$
Theory	0.024 Ω	0.043 Ω	$57.2 \cdot 10^6 \text{ V/C}$	$103.9 \cdot 10^6$

Table 4.1

can be concluded that, bringing together the plots of Fig. 4.3(a), Fig. 4.3(b) and the values in Table 4.1, an acceptable agreement between simulations' outcomes and analytical calculations has been achieved within about 20%, which is the discrepancy found between the numerical and theoretical impedance and loss factor values.

4.1.2 Beam pipe with thick resistive insert

The longitudinal and the transverse loss factors of a Gaussian bunch passing inside a round beam pipe, having an azimuthally symmetric thick resistive insert, was calculated. The insert was enough long in order to be able to neglect the contribution of the insert ends, as shown in Fig. 4.4.

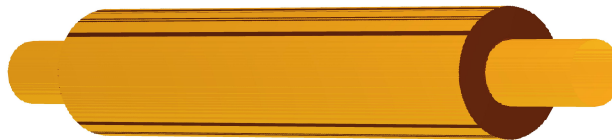


Figure 4.4. GdfidL model for the azimuthally symmetric beam pipe with resistive insert. The chosen length was $L = 30 \text{ cm}$, the insert thickness $a = 5 \text{ mm}$, the pipe radius plus the insert thickness $b = 10 \text{ mm}$, and the electrical conductivity $\sigma_c = 7.69 \cdot 10^5 \text{ S/m}$ for Carbon Fiber Composite (CFC).

In this case the loss factors can be found analytically [54, 55, 56]:

$$k_{\parallel} = \frac{cL}{4\pi b\sigma^{3/2}} \sqrt{\frac{Z_0\rho}{2}} \Gamma\left(\frac{3}{4}\right), \quad (4.2)$$

for the longitudinal one and

$$k_{\perp} = \frac{cL}{\pi^2 b^3} \sqrt{\frac{2Z_0\rho}{\sigma_z}} \Gamma\left(\frac{5}{4}\right) \quad (4.3)$$

for the transverse one, where $c = 2.997925 \times 10^8 \text{ m/s}$ is the speed of light, L is the length of the pipe, $\rho = \sigma_c$ is the electrical resistivity, σ_z the bunch length and Γ

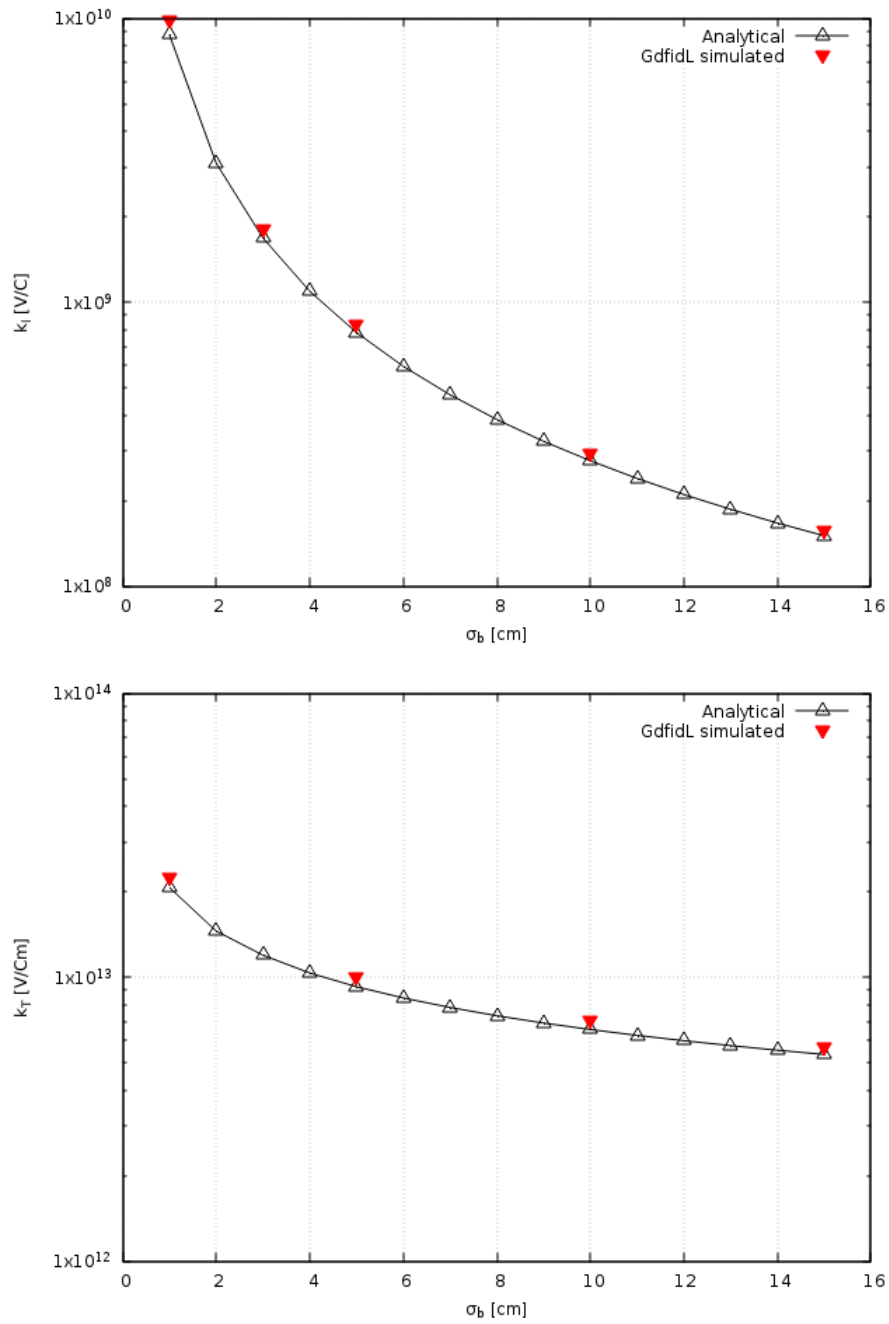


Figure 4.5. Loss and kick factors benchmark between GdfidL and analytical formulas Eq. (4.2) and Eq. (4.3).

the Euler gamma function. Figure 4.5 shows a comparison between the analytical formulas and the numerical data. As it is seen the agreement is quite satisfactory.

However, the loss factors are somewhat “averaged” values characterizing the beam impedance. In order to check the impedance frequency behavior the RW impedance of the insert has been calculated using the semi-analytical mode-matching

method (MMM) [57]. In turn, numerically the impedance till rather low frequencies has been obtained by performing a Fourier transform of a long wake behind a long bunch obtained by Gdfidl, and also by CST PS[58] for comparison. As it is seen in Fig. 4.6 also the impedance frequency behavior is reproduced well by Gdfidl.

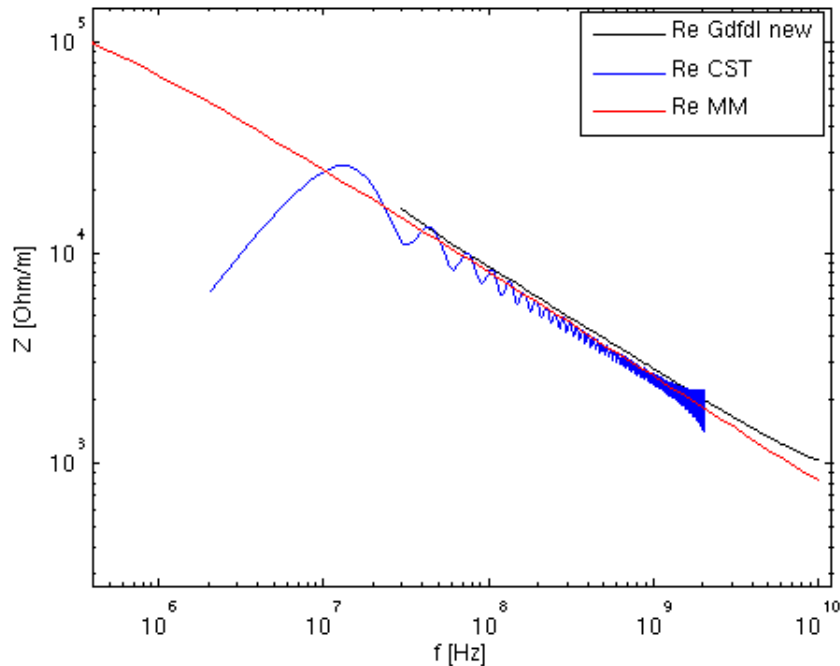


Figure 4.6. Outcomes of the benchmark between Gdfidl, CST and MMM on dipolar transverse impedance.

4.2 Ferrite Material Simulation Test

In order to damp parasitic higher order modes (HOMs) in the new collimators with embedded BPM pickup buttons, special blocks made of the TT2-111R lossy ferrite material are used. For this reason a comprehensive numerical study has been carried out, aimed at testing the ability of Gdfidl to reproduce frequency dependent properties of the lossy ferrite in calculations of wake fields, impedances and scattering matrix parameters [59].

For this purpose, it was a) simulated a typical coaxial-probe measurement of the ferrite scattering parameter S_{11} ; b) compared the computation results of CST MW, Gdfidl and MMM by calculating impedances of an azimuthally symmetric pill-box cavity filled with the TT2-111R ferrite in the toroidal region; c) benchmarked Gdfidl simulations against analytical Tsutsui model for a rectangular kicker with ferrite insert [60, 61] and CST simulations for the same device.

All the comparative studies have confirmed a good agreement between the results obtained by Gdfidl and the results provided by other numerical codes, by available analytical formulas and by the mode matching semi-analytical approach.

It must be pointed out that the dispersive properties of user-defined materials, namely the frequency-dependent permittivity $\epsilon_r(\omega) = \epsilon' + i\epsilon''$ and permeability $\mu_r(\omega) = \mu' + i\mu''$ [62], are specified by means of N^{th} order Lorentz functions, with resonant frequencies ω_n and damping frequencies γ_n , as follows:

$$\epsilon_r(\omega) = \epsilon_\infty + \epsilon_\infty^2 \sum_{n=1}^N \frac{A_n \omega_n^2}{\omega_n^2 - i\omega\gamma_n - \omega^2} \quad (4.4)$$

$$\mu_r(\omega) = \mu_\infty + \mu_\infty^2 \sum_{n=1}^N \frac{A_n \omega_n^2}{\omega_n^2 - i\omega\gamma_n - \omega^2}, \quad (4.5)$$

where A_n is the amplitude of the n^{th} resonance. So, in order to correctly simulate the behaviour in impedance of devices with dispersive materials with GdfidL, one has first to input an appropriate Lorentz function describing the available experimental data. It means that these latter have to be fitted with the Lorentz model with parameters A_n , ω_n , γ_n and ϵ_∞ or μ_∞ . Thus $(3N + 1)$ parameters must be set in the input file.

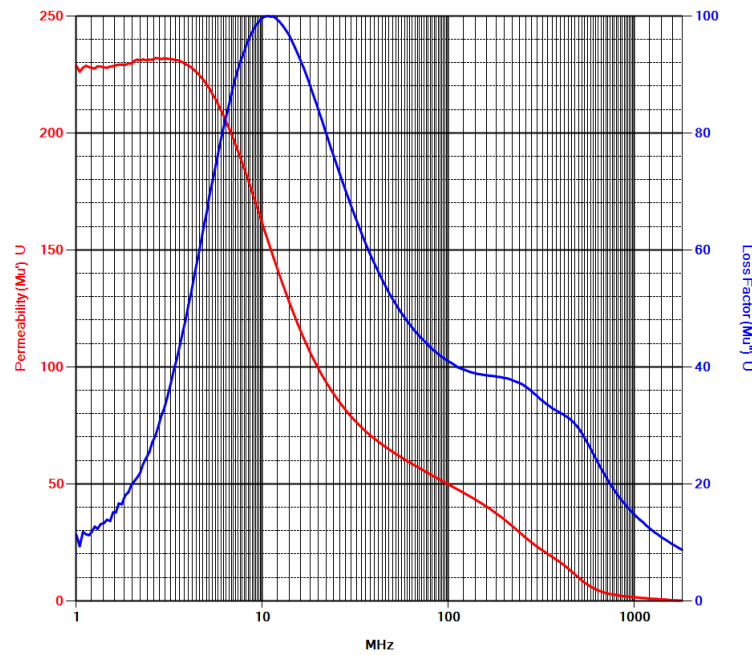


Figure 4.7. Experimental data for magnetic permeability of TT2-111R ferrite (Courtesy of B. Salvant, CERN).

The fitting procedure has been performed in Sage Mathematics Software (Version 6.8)[63], minimizing the χ^2 of the real and imaginary parts of first, second and third order permeability Lorentz functions, with the available experimental data for the real and imaginary parts of TT2-111R ferrite permeability, shown in Fig. 4.7. It resulted that the best fit was provided by a third order Lorentz function, as shown

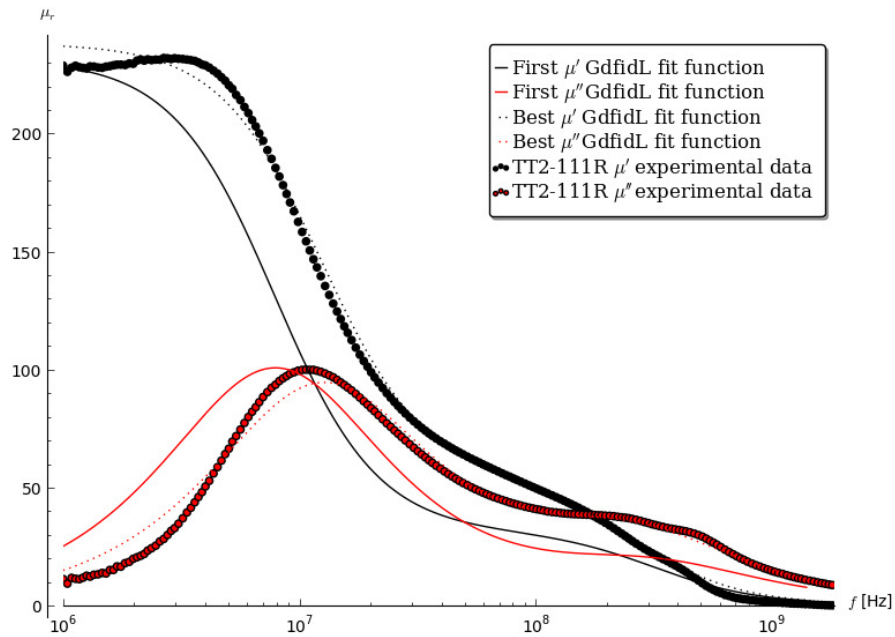


Figure 4.8. Fitting curves obtained from Sage Mathematics Software for the real and imaginary parts of the permeability experimental data of the TT2-111R ferrite, shown in solid circles. The solid lines are the result of the fit with a first order Lorentz function, whereas the dotted ones represent the fit with a third order Lorentz function. For the data and all the curves, the black and red colours indicate the real and imaginary parts, respectively.

in Fig.4.8, with the following parameter values:

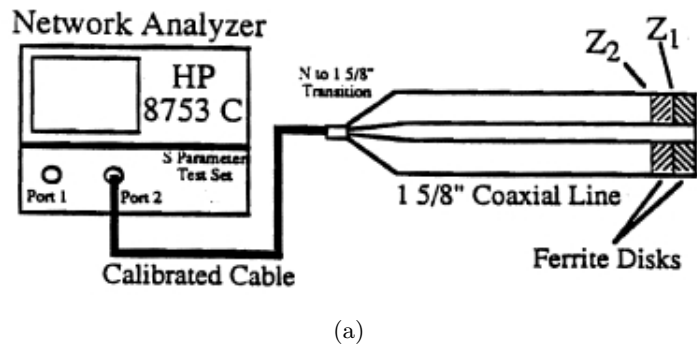
$$\begin{aligned}
 \mu_{\infty} &= 1.06286; & \omega_1 &= 2\pi 1.1575 \cdot 10^9; & A_1 &= 162.94; & \gamma_1 &= 6.7946 \cdot 10^{11} \\
 & & \omega_2 &= 2\pi 2.6911 \cdot 10^9; & A_2 &= 46.960; & \gamma_2 &= 1.7398 \cdot 10^{11} \\
 & & \omega_3 &= 2\pi 1.1154 \cdot 10^5; & A_3 &= 33.237; & \gamma_3 &= 6.1474 \cdot 10^9
 \end{aligned}$$

4.2.1 Scattering parameter S_{11} of a coaxial probe

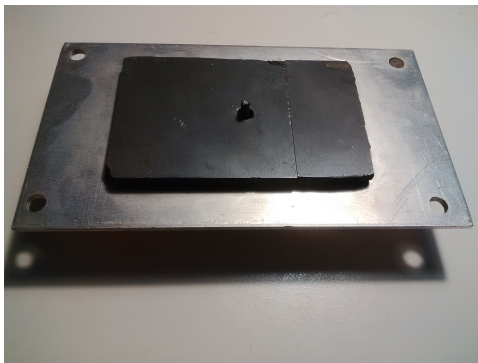
In order to test correct permeability implementation into GdfidL, a simple coaxial probe measurement simulation was arranged, according to a typical experimental setup as shown in Fig. 4.9 and documented elsewhere [64], checking for the numerically computed S-parameters [65] to be fully in agreement with theoretical prediction. Figure 4.10(a) shows a simplified sketch of a set-up for the ferrite material properties measurements: just a coaxial line filled with a ferrite material under test, while Fig. 4.10(b) its geometry reproduced by GdfidL. For such a simple structure the reflection coefficient S_{11} is easily measured and can be found analytically as [65]

$$S_{11} = \frac{\Delta \cdot \tanh(\gamma L) - 1}{\Delta \cdot \tanh(\gamma L) + 1}, \quad (4.6)$$

with $\gamma = j\omega\sqrt{\epsilon\mu}$ and $\Delta = \sqrt{\frac{\mu_r}{\epsilon_r}}$. Figure 4.11 shows the S_{11} coefficient calculated for the TT2-111R material in a very wide frequency range, from 10^6 to 10^{12} Hz. As it



(a)

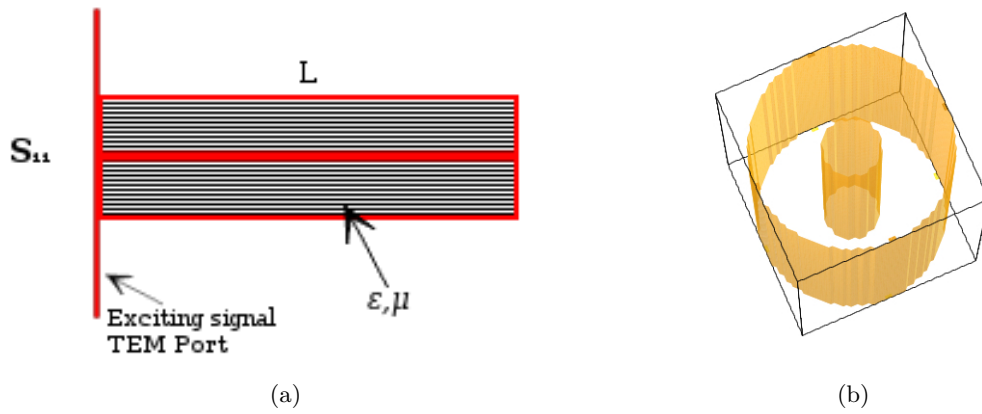


(b)



(c)

Figure 4.9. (a) measurement layout [64]. (b) and (c) ferrite plate and its adaptor to a coaxial probe.



(a)

(b)

Figure 4.10. Coaxial probe measurement sketch (a) and model (b) for GdfidL S_{11} simulations.

is seen, despite the complicated S_{11} frequency dependence the agreement between GdfidL, HFSS frequency domain code and the analytical formula is remarkable.

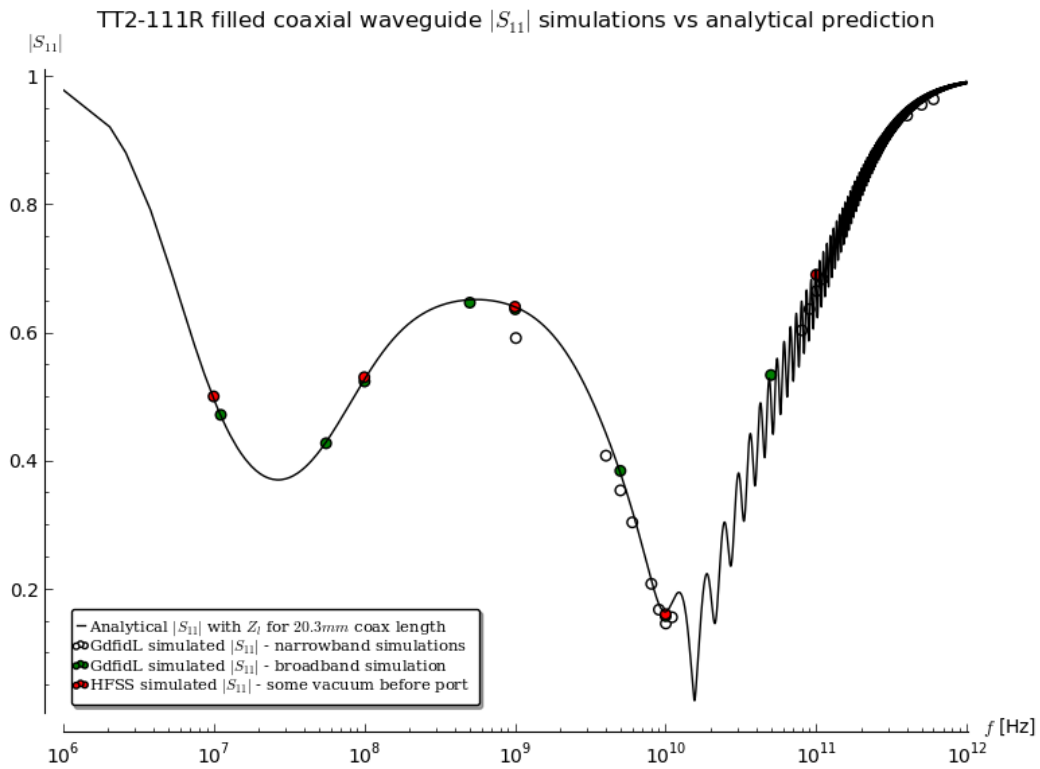


Figure 4.11. Reflection coefficient S_{11} results for the arranged simulation setup. The solid line is the analytical trend from Eq. (4.6).

4.2.2 Impedance of a ferrite filled pillbox

The impedance of a simple pillbox geometry, filled with the TT2-111R ferrite in its toroidal region, was calculated with GdfidL, CST PS and MMM codes, according to the model shown in Fig. 4.12. The benchmark concerned the longitudinal and

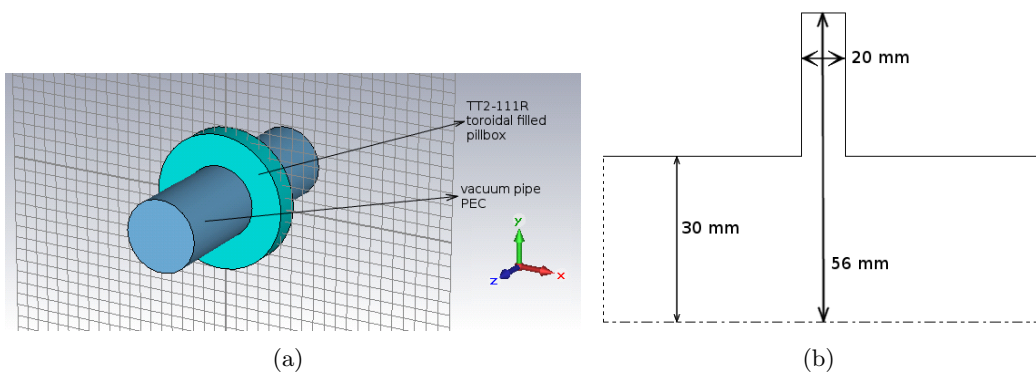


Figure 4.12. Geometry of the pillbox filled with TT2-111R in its toroidal region (a), as simulated by CST, GdfidL and MMM, and details of its dimensions (b).

transverse dipolar impedance. The results in Fig. 4.13 and Fig. 4.14 demonstrate that

the impedances computed by the three codes are in a very good agreement. There are, however, some tiny differences. While for the longitudinal impedance GdfidL results differ of about 10% from the MMM and CST results, in the frequency range $500 \text{ MHz} \lesssim f \lesssim 1 \text{ GHz}$, it is the MMM that computes a slightly different transverse dipolar impedance, with respect to CST and GdfidL, for $f \gtrsim 100 \text{ MHz}$, always of few percents. In the field of impedance numerical computations such differences may be meaningless, being ascribable to different computation algorithms, differences in the mesh sizes and mesh geometries (rectangular, hexaedral etc.) and, most importantly, the way in which the dispersive properties of materials are implemented in the different codes.

4.2.3 Tsutsui model for TT2-111R ferrite kicker

An extensive benchmark simulations' campaign rooted about a simplified model of ferrite kicker magnet, whose longitudinal and transverse impedances were analytically calculated by Tsutsui [60, 61]. The model is illustrated in Fig. 4.15(a) and is such that the ferrite is at $-a < x < a$, $b < |y| < d$. There is vacuum between two ferrite rectangular blocks ($-a < x < a$, $-b < y < b$) and the outside ($|x| > a$ or $|y| > d$) is filled with PEC material. The beam passes at $x = y = 0$ in the positive z direction, out of the page. It is found that for such a structure the following equations hold,

$$\frac{Z_{\parallel}}{L} = j \frac{Z_0}{2a} \sum_{n=0}^{\infty} \frac{1}{\left[\frac{k_{xn}}{k} (1 + \epsilon_r \mu_r) \text{shch} + \frac{k_{yn}}{k} (\mu_r \text{sh}^2 \text{tn} - \epsilon_r \text{ch}^2 \text{ct}) \right] / (\epsilon_r \mu_r - 1) - \frac{k}{k_{xn}} \text{shch}}, \quad (4.7)$$

$$\frac{Z_{\perp}^X}{L} = j \frac{Z_0}{2a} \sum_{n=0}^{\infty} \frac{k_{xn}^2}{k} \left[\frac{\frac{k_{xn}}{k} (1 + \epsilon_r \mu_r) \text{shch} + \frac{k_{yn}}{k} (\mu_r \text{sh}^2 \text{tn} - \epsilon_r \text{ch}^2 \text{ct})}{(\epsilon_r \mu_r - 1)} - \frac{k}{k_{xn}} \text{shch} \right]^{-1}, \quad (4.8)$$

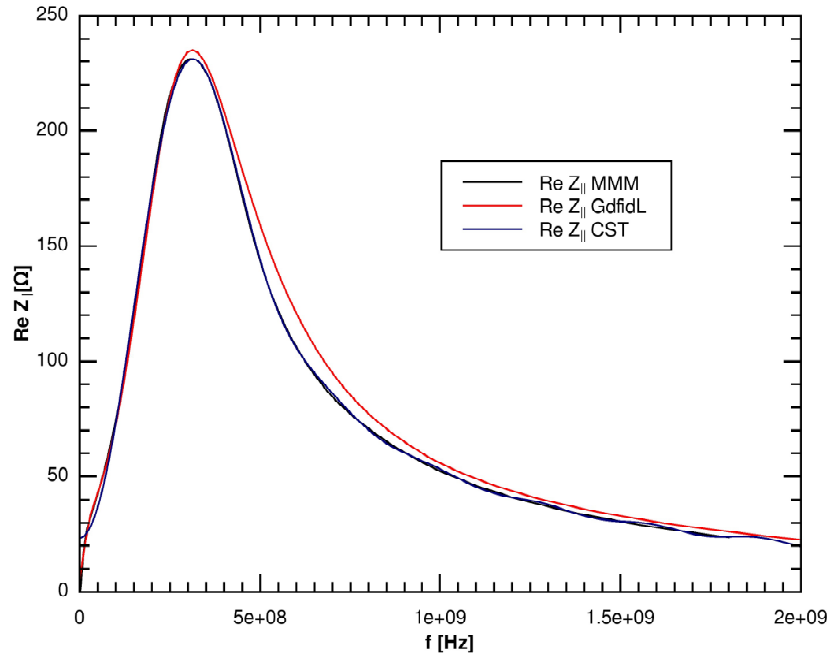
$$\frac{Z_{\perp}^Y}{L} = j \frac{Z_0}{2a} \sum_{n=0}^{\infty} \frac{k_{xn}^2}{k} \left[\frac{\frac{k_{xn}}{k} (1 + \epsilon_r \mu_r) \text{shch} + \frac{k_{yn}}{k} (\mu_r \text{ch}^2 \text{tn} - \epsilon_r \text{sh}^2 \text{ct})}{(\epsilon_r \mu_r - 1)} - \frac{k}{k_{xn}} \text{shch} \right]^{-1}, \quad (4.9)$$

where Z_0 is, as usual, the impedance of free space, L the device length, $k = \omega/c$ the wave number, $k_{xn} = 2(n+1)\pi/(2a)$, $n = 0, 1, 2, \dots$ are the expansion coefficients of the electromagnetic field in the vacuum region (as the sum of the source field and the waveguide modes), and $k_{yn} = \sqrt{(\epsilon_r \mu_r - 1)k^2 - k_{xn}^2}$. In all the equations above, the parameters $\text{sh} = \sinh(k_{xn}b)$, $\text{ch} = \cosh(k_{xn}b)$, $\text{tn} = \tan(k_{yn}(b-d))$, $\text{ct} = \cot(k_{yn}(b-d))$, $\epsilon_r = \epsilon_r' - j\epsilon_r'' + \frac{\sigma}{j\omega\epsilon_0}$ and $\mu_r = \mu_r' - j\mu_r''$ were defined.

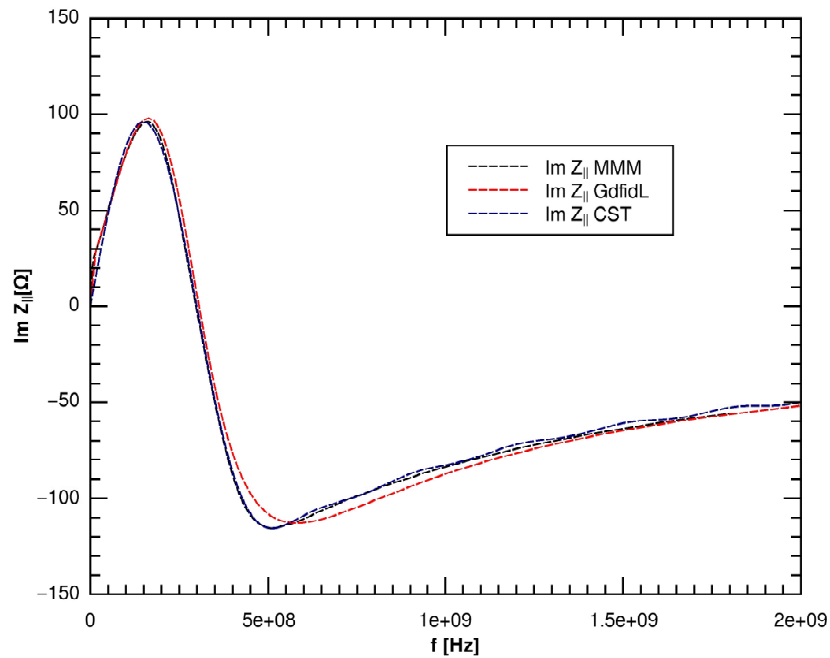
The kicker model geometries set into CST PS and GdfidL are shown in Fig. 4.15(b) and Fig. 4.15(c), respectively. The simulations' results for longitudinal, transverse dipolar and transverse quadrupolar impedances, compared with the analytical models, are shown in Fig. 4.16, Fig. 4.17 and Fig. 4.18 respectively, separated in their real and imaginary parts.

For the longitudinal case, the impedance calculated by GdfidL is closer to the analytical curve than that of CST at least for lower frequencies and up to $\approx 6 \text{ GHz}$. In this range GdfidL and analytical curves differ of $\approx 9\%$, whereas CST and analytical

curves of $\approx 15\%$, both for real and imaginary parts. At frequencies $\gtrsim 6GHz$, however, CST and analytical results seem to converge to the same values, while GdfidL ones start to diverge significantly (nearly 60%). However the low frequency

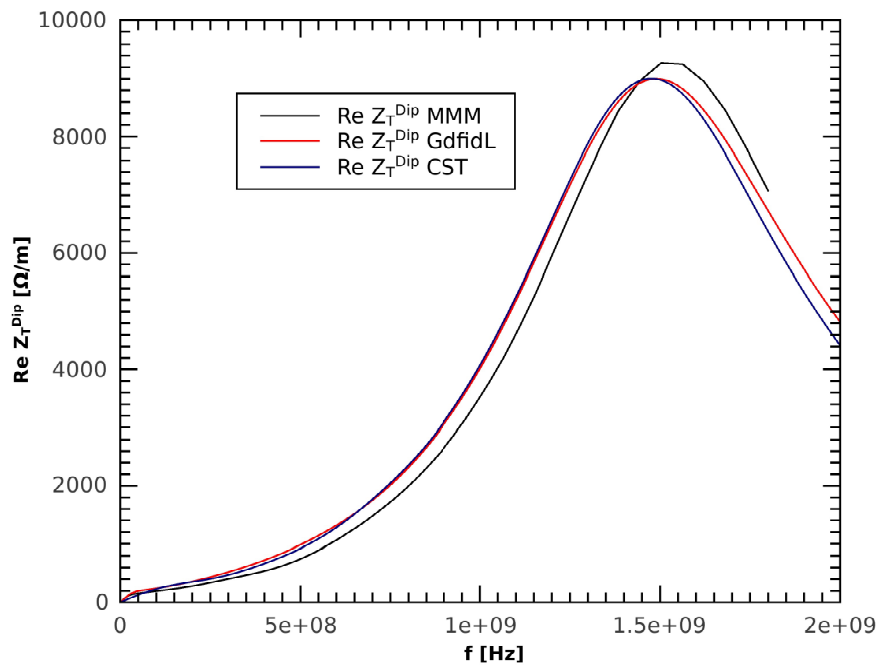


(a)

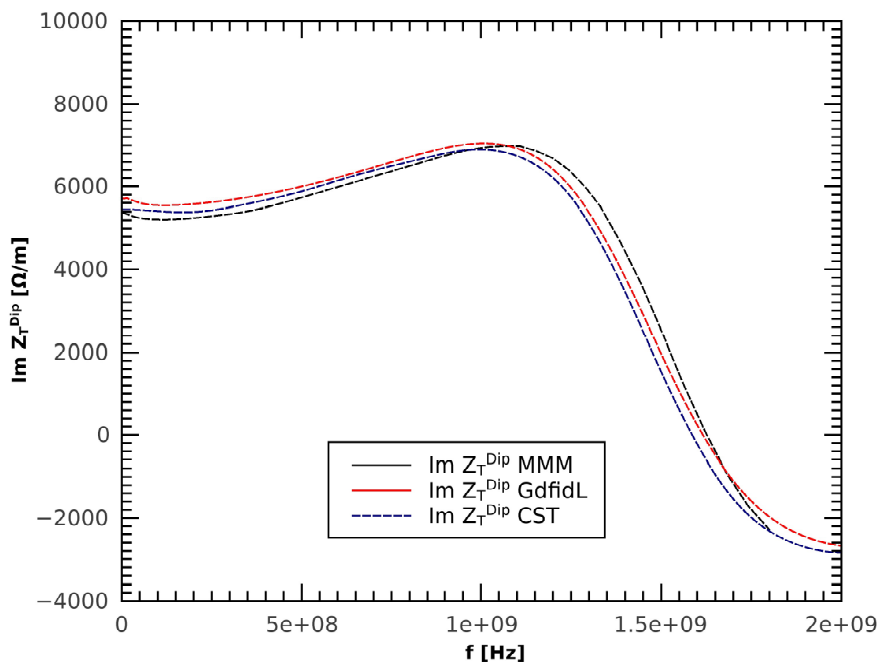


(b)

Figure 4.13. Real (a) and imaginary (b) parts of the transverse impedance for the pillbox cavity, as computed by MMM, GdfidL and CST.



(a)



(b)

Figure 4.14. Real (a) and imaginary (b) parts of the longitudinal impedance for the pillbox cavity, as computed by MMM, GdfidL and CST.

peak at around 1 GHz is computed at the same frequency both by CST and GdfidL.

For the transverse dipolar impedance, the only significant feature of the two EM codes' computations seems to be a broader and splitted peak at $f \approx 2$ GHz in the real

part, with respect to the analytical prediction. Both the real and imaginary parts of the simulated impedance agree within $\approx 10\%$ with the theory up to $f \approx 6$ GHz, while converging to the same values at higher frequencies. Finally, the transverse quadrupolar impedance simulated by GdfidL shows a similar behaviour with respect to theoretical and CST curves. This is particularly true for the imaginary part (apart from a divergence for very low frequencies below 100 MHz), whereas for the real part a broader curve with values differing from the theory of about 15%, is computed by GdfidL, still converging to the same values at higher frequencies. As a conclusion for this particular batch of simulations, it can be said that a reasonable agreement was found between GdfidL impedance computations for the ferrite loaded kicker structure, the Tsutsui analytical model and CST PS simulations.

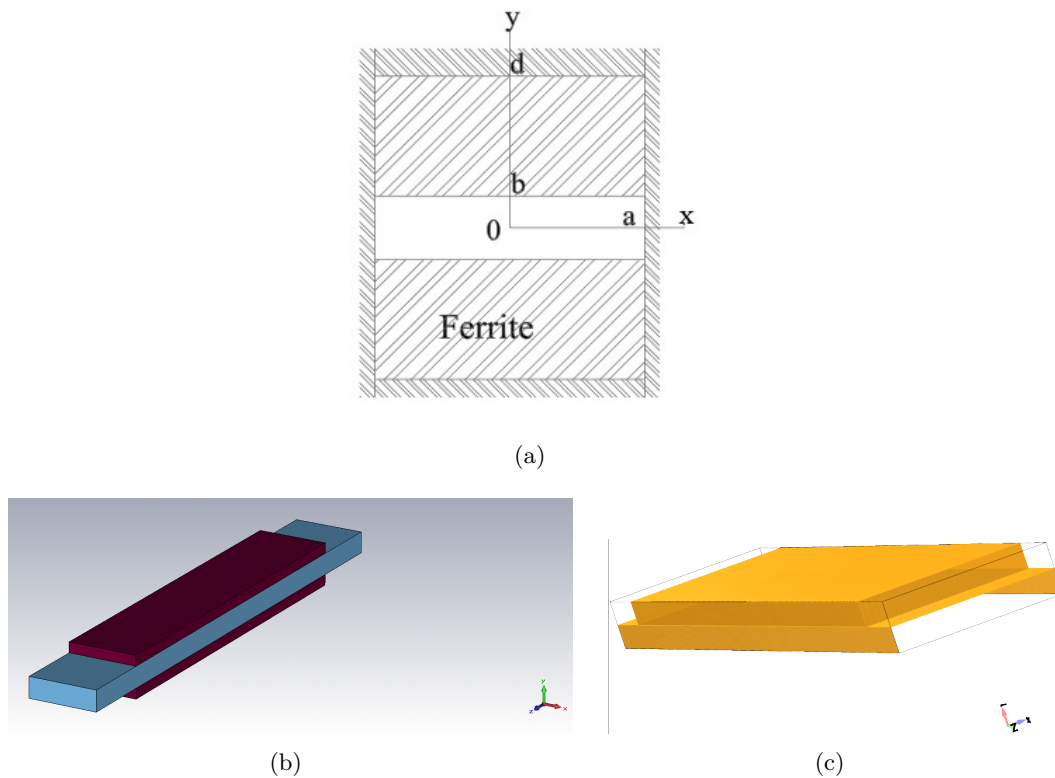


Figure 4.15. (a) ferrite kicker model as sketched in the original paper by Tsutsui [60], (b) and (c) the same model as reproduced in CST and GdfidL, respectively.

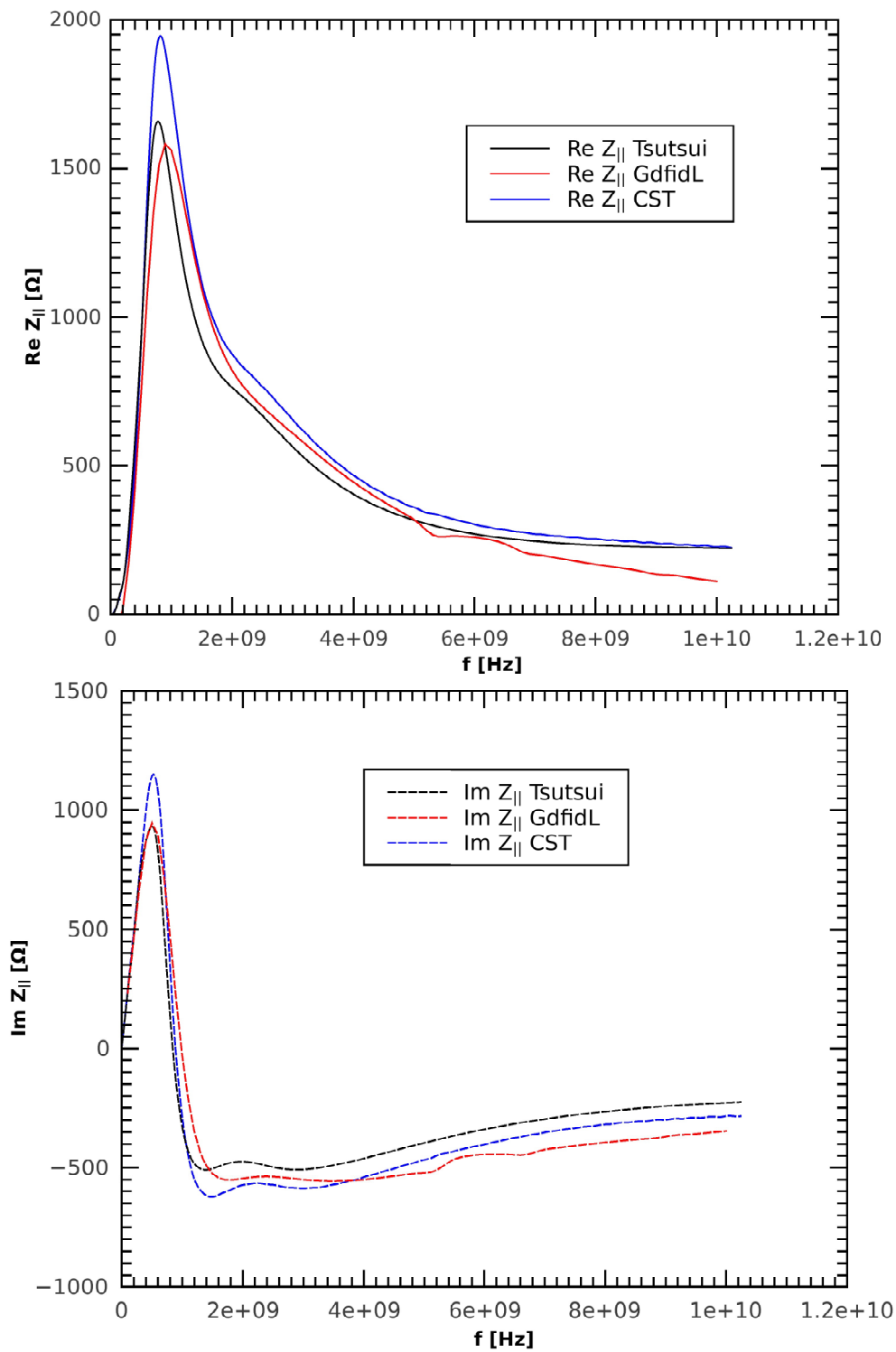


Figure 4.16. Real (up) and imaginary (down) parts of the longitudinal impedance as calculated from the Tsutsui analytical model and from simulations with GdfidL and CST PS.

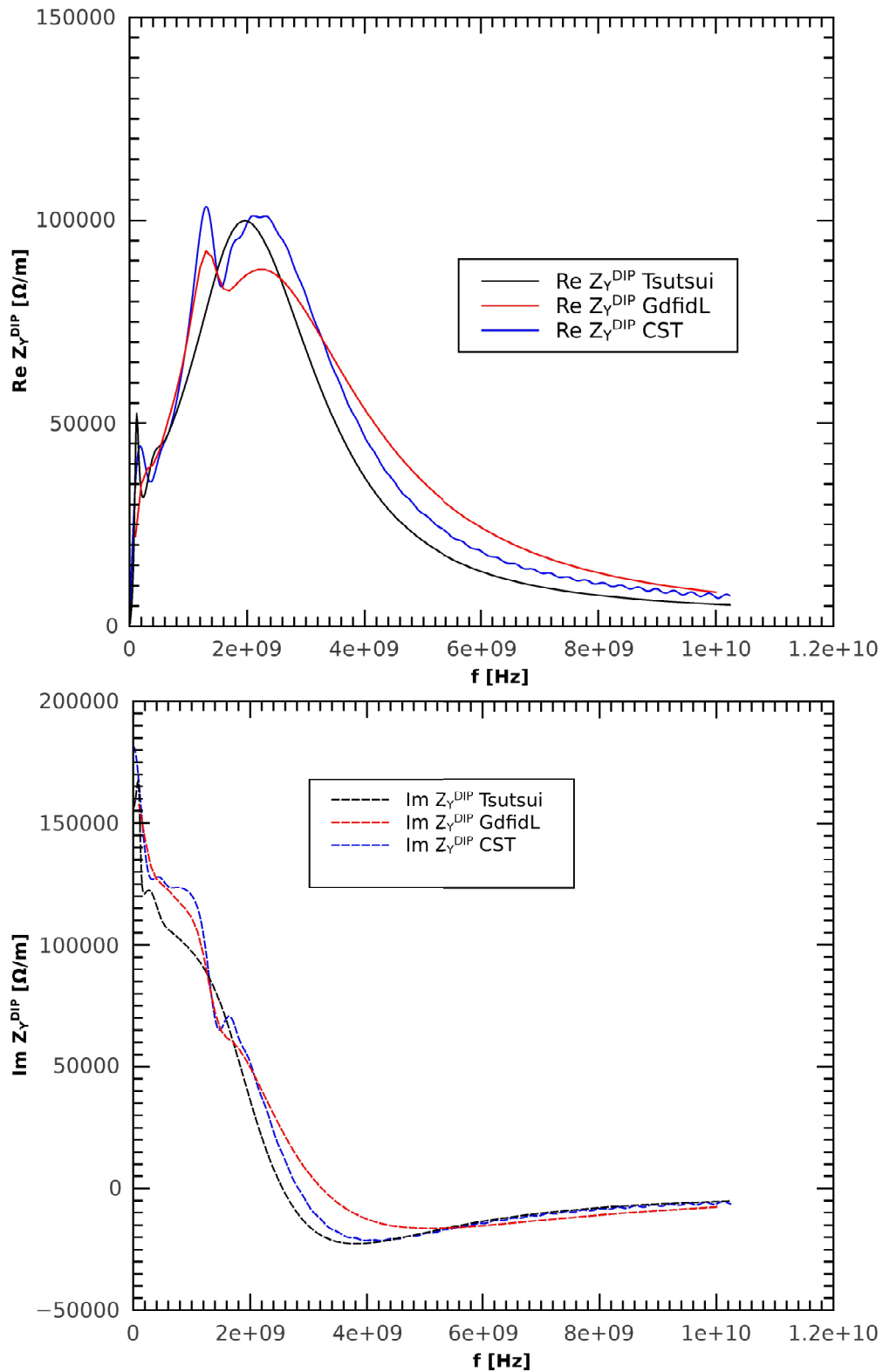


Figure 4.17. Real (up) and imaginary (down) parts of the transverse dipolar impedance as calculated from the Tsutsui analytical model and from simulations with GdfidL and CST PS.

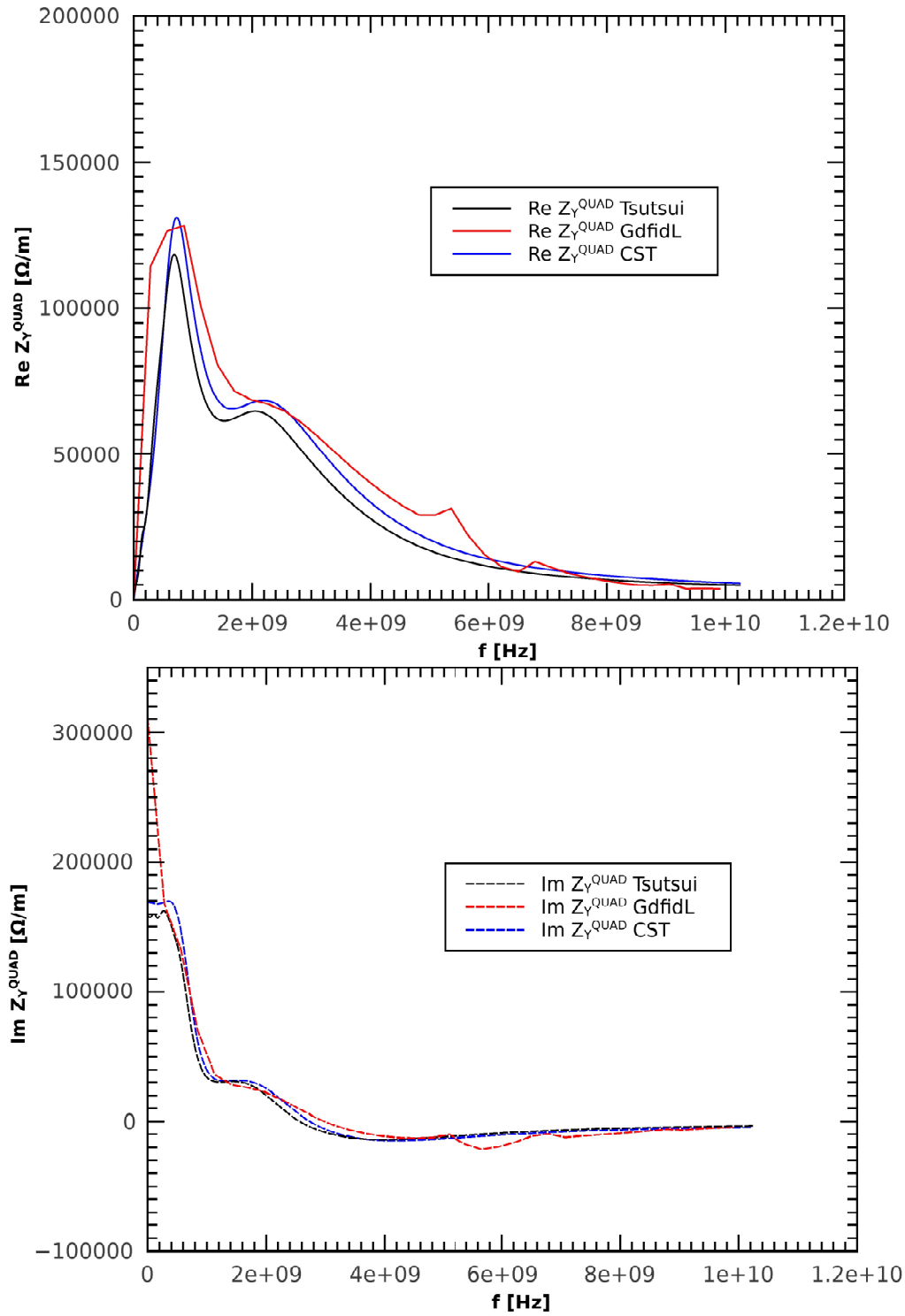


Figure 4.18. Real (up) and imaginary (down) parts of the transverse quadrupolar impedance as calculated from the Tsutsui analytical model and from simulations with GdfidL and CST PS.

Chapter 5

LHC Run II TCS/TCT collimators

As already mentioned in the previous chapter, 2 old CFC TCS and 16 W TCT collimators were replaced in the LHC, by new devices embedding BPMs in the jaws' tapering regions. The proposal and installation of these new collimators' structures was motivated by the fact that for optimal performances the collimators' jaws must be centered around the local orbit. The beam-based alignment, however, is performed by touching the beam halo with both jaws of each collimator. This method requires dedicated fills at low intensities that are done infrequently and makes the procedure very time consuming and does limit the operational flexibility [53]. In order to overcome these limitations, two BPM pickups are installed at the extremities of each jaw, to provide a measurement of the beam orbit at the upstream and downstream sides of the collimators, as shown in Fig. 5.1(a). The BPM pickups are hosted in an additional "ad-hoc" rectangular flat taper (the closest to the beam), adjacent to the round elliptical one (the farther away from the beam). At the request of the collimation project team and following the issues with RF contacts that occurred in 2011 for the LHC Run I collimators, the CERN impedance team has recommended to leave the gap between the jaws and the upper and lower plates open, without the RF contacts, and to install special ferrite (TT2-111R) blocks to suppress parasitic HOMs, as indicated in Fig. 5.1(b). In the spirit of the approach discussed in section 3.1, again calculations of the geometric broad band wakes of the old and new collimators were performed. At a first attempt, the aim was to gain a preliminary estimate of the new design contribution to impedance. Values

	w/ BPM cavity	w/o BPM cavity
Half gaps (<i>mm</i>)	k_T ($\frac{V}{C_m}$)	k_T ($\frac{V}{C_m}$)
1	$3.921 \cdot 10^{14}$	$3.340 \cdot 10^{14}$
3	$6.271 \cdot 10^{13}$	$5.322 \cdot 10^{13}$
5	$2.457 \cdot 10^{13}$	$2.124 \cdot 10^{13}$

Table 5.1. Geometric transverse kick factors due to the LHC Run I and Run II TCS/TCT geometries, calculated at different half gap values.

listed in Table 5.1, calculated for three different jaws' half gaps, clearly show that

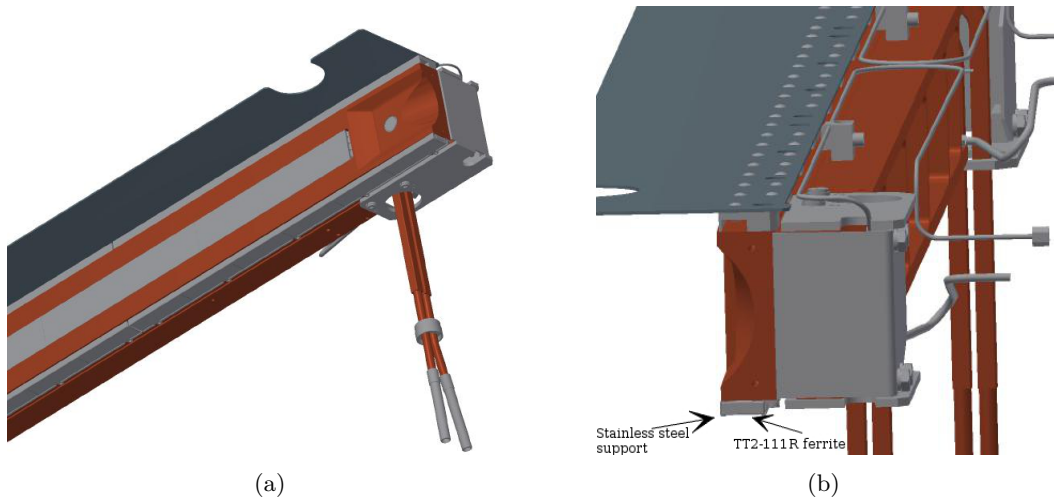


Figure 5.1. Detailed view of (a) BPM pickup position in the tapering region and (b) ferrite blocks positioning, in the gap between the jaws and the metallic plates.

the geometric transverse effective impedance of the new collimators was expected to increase of about 20% with respect to the old design, mainly due to the first tapers with a steeper angle.

5.1 New TCS/TCT's taper design optimization study

One of the possible way to reduce the impedance of collimators is to reduce the tapering angle. The LHC Run II secondary collimators' design consists of two tapers at different angles, separated by a longitudinal gap, and at different distance from the beam axis. The one closest to the beam contributes the most to the overall impedance. As already shown in Chapter 3, the best analytical approximation to the tapers' geometry is the Stupakov formula for flat taper [42, 66]. Thus writing down the impedance of the two tapers as a function of the first one's (the closest to the beam) angle and length, it is possible to find local minima and the best set of tapers' angles and lengths.

The total transverse impedance for two flat tapers, separated by a longitudinal gap g , as a function of first taper's length L_1 and angle α_1 , can be written as

$$Z_{\perp} = \frac{Z_0 h_1}{8} \left(\frac{1}{a^2} - \frac{1}{(L_1 \tan(\alpha_1) + a)^2} \right) \tan(\alpha_1) + \frac{(d - L_1 \tan(\alpha_1) - a) Z_0 h_2 \left(\frac{1}{(L_1 \tan(\alpha_1) + a)^2} - \frac{1}{d^2} \right)}{8(L - L_1 - g)}, \quad (5.1)$$

in which the fixed parameters are the collimator's half gap a , final height from the beam axis d , the gap g and total tapers' length $L = L_1 + L_2 + g$. The geometrical sketch of the problem is given in Fig. 5.2 For the case under study, the above parameters were allowed to assume the values $0^\circ \leq \alpha_1 \leq 45^\circ$, $18.7 \text{ mm} \leq L_1 \leq 97.4 \text{ mm}$, $a = 1, 5, 20 \text{ mm}$, $d - a = 18.7 \text{ mm}$ and $L = 147 \text{ mm}$, due to

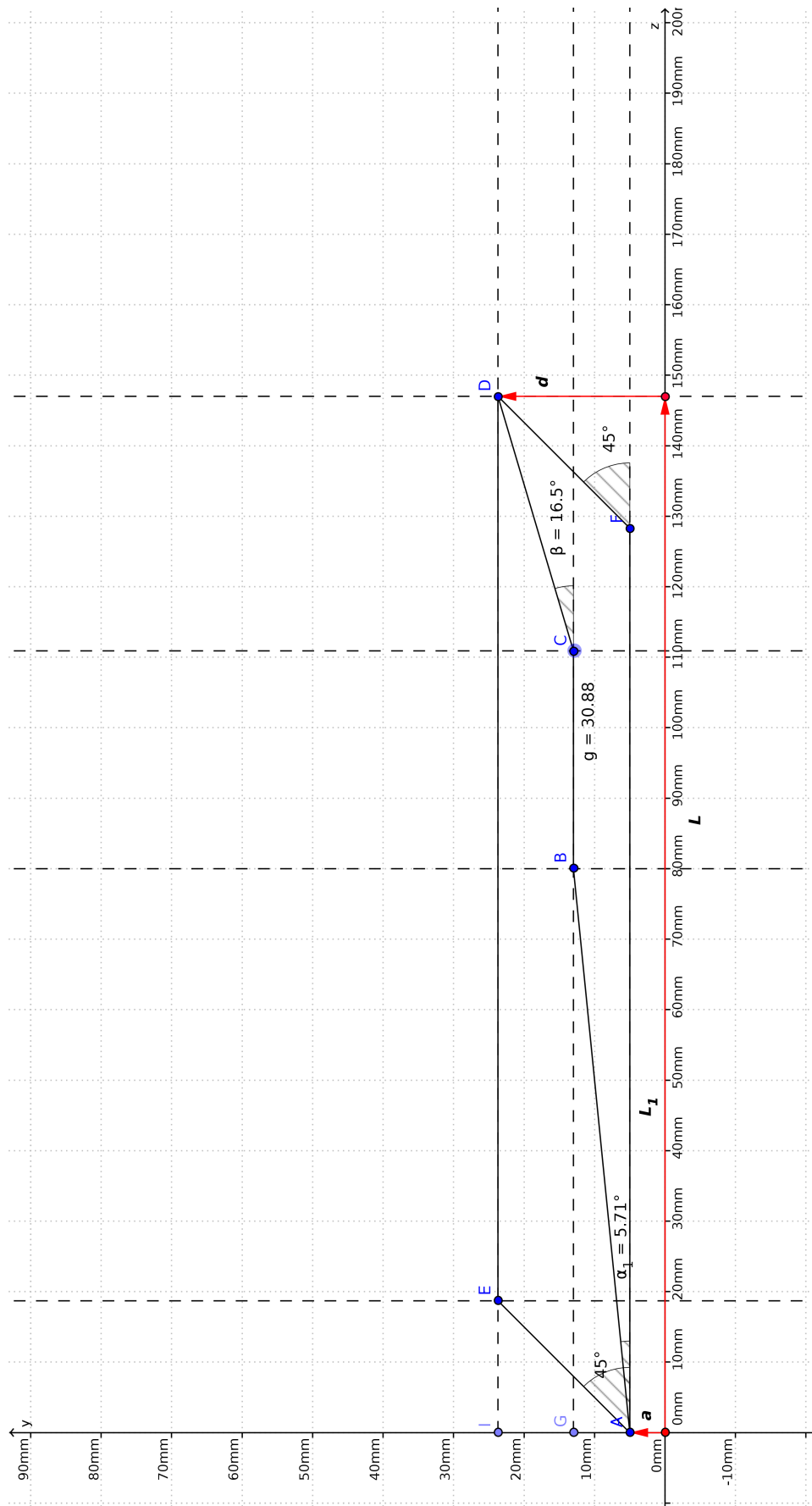


Figure 5.2. Geometrical sketch of the problem of impedance minimization by tapering angle optimization.

engineering constraints. The impedance surface in the three dimensional space L_1 [m], α_1 [rad], Z_{\perp} [Ω/m], for the three different half gaps a , is shown in Fig. 5.3. As expected, the half gap broadens the surface as it grows to higher values. Just as an example, in Fig. 5.4 the Z_{\perp} surface cross sections, for $a = 5$ mm, are reported in the two planes L_1 [m], Z_{\perp} [Ω/m] and α_1 [rad], Z_{\perp} [Ω/m]. As a result, the best set of values of lengths and angles for Z_{\perp} local minima was found for $a = 1$ mm and $a = 5$ mm, as reported in Table 5.2 The LHC Run II TCS/TCT collimators

	$Z_{\perp_{min}}$ [$\text{k}\Omega/\text{m}$]	L_1 [mm]	α_1 [$^{\circ}$]	L_2 [mm]	α_2 [$^{\circ}$]
$a = 1$ mm	105.382	70	2.29	46.12	19.02
$a = 5$ mm	7.848	64.4	4.7	51.7	14.5

Table 5.2. Best set of taper's lengths and angles for Z_{\perp} local minima.

have design values of $\alpha_1 = 17.74^{\circ}$, $L_1 = 25.78$ mm, $\alpha_2 = 16^{\circ}$, $L_2 = 37.32$ mm, with respect to which a substantial estimated gain in geometric transverse impedance was found, as reported in Table 5.3, where $Z_{\perp_{old}}$ [$\text{k}\Omega/\text{m}$] = 26.24. However, due to the

	$Z_{\perp_{old}}/Z_{\perp_{min}}$
$a = 1$ mm	5.2
$a = 5$ mm	2.64

Table 5.3. Estimated geometric impedance gain of the new tapers' lengths and angles set, with respect to the collimator's design values.

same engineering constraints mentioned before, it was possible to prototype the new collimators with the lengths and angles sketched in Fig. 5.5. With that parameters set of values, the transverse geometric impedance was found to be Z_{\perp} [$\text{k}\Omega/\text{m}$] = 11.74, which in any case represents a favorable improvement.

5.1.1 Resistive wall impedance contribution from the new angle set

The new (small) angles' set collimator can, in principle, be affected by a stronger RW contribution to the impedance, especially for small half gaps values. In order to estimate this contribution, again a kick factors comparison for the two geometries (design values vs. prototype values in Fig. 5.5) was carried out, performing simulations for two flat tapers, using the new GdfidL version with implemented IBCs, as shown in Fig. 5.6. Taking $\sigma_c = 1.4 \cdot 10^5$ S/m as the electrical conductivity for the CFC jaws, a wake length of $s = 75$ cm was traced for a bunch length $\sigma_b = 7.5$ cm, whose results in terms of kick factors are listed in Table 5.4 for $a = 1$ mm and in Table 5.5 for $a = 5$ mm, where "old" and "new" stay for design and prototype kick factors, respectively.

As it is evident from Table 5.6, also in the case of RW impedance, the new collimator's tapering region structure results to be favorable with respect to the old one, giving an estimated reduction of a factor ≈ 3 in impedance and an almost similar kick for 1 mm of half gap, and of a factor ≈ 2.6 in impedance and ≈ 2.1 in the kick for 5 mm of half gap.

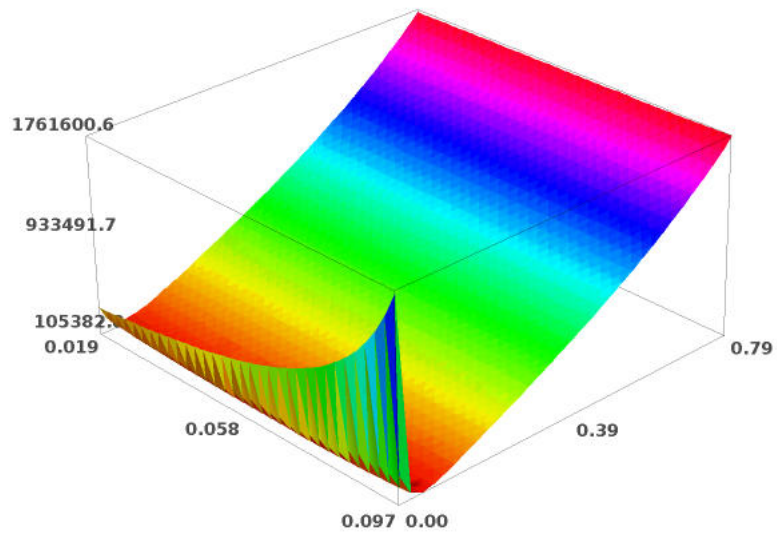
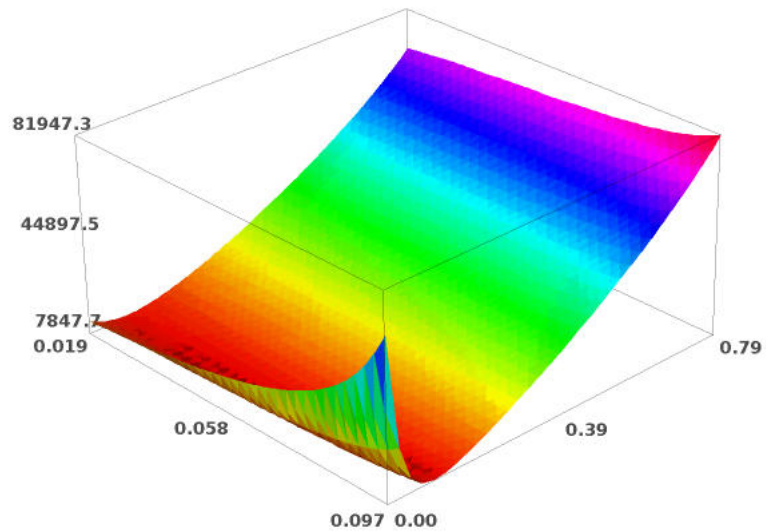
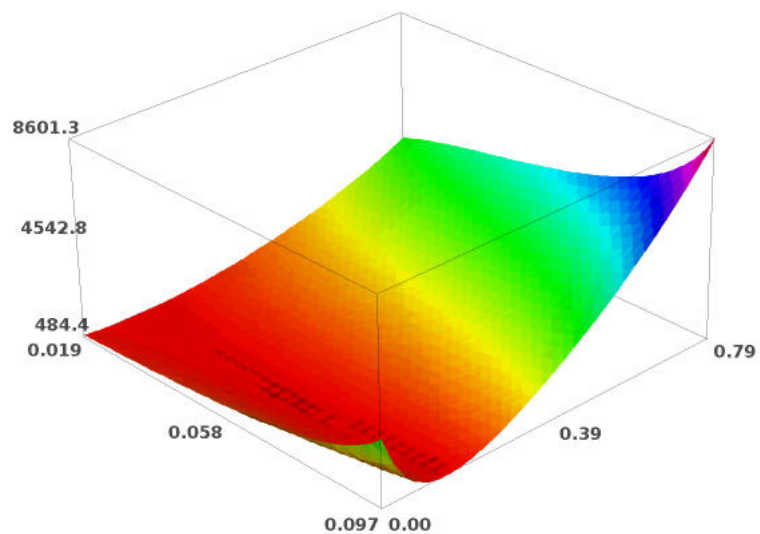
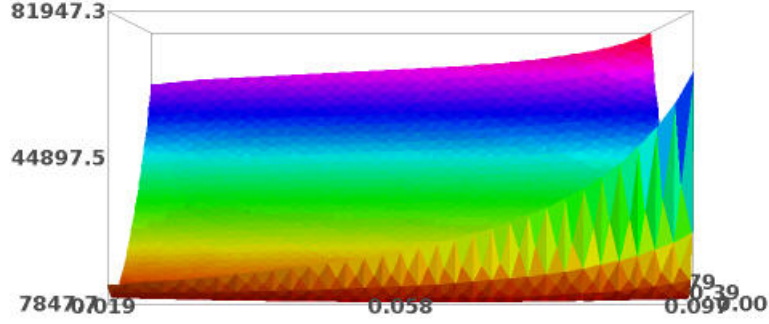
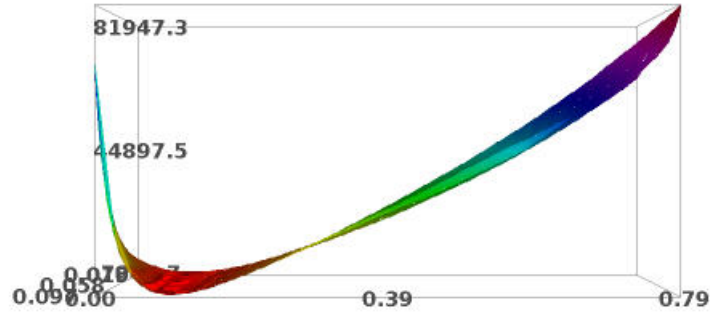
(a) $a = 1$ mm(b) $a = 5$ mm(c) $a = 20$ mm

Figure 5.3. Transverse impedance surface, from eq. 5.1, as a function of L_1 [m] and α_1 [rad], for fixed a values.

(a) View in the L_1 [m], Z_{\perp} [Ω/m] plane(b) View in the α_1 [rad], Z_{\perp} [Ω/m] plane**Figure 5.4.** Transverse impedance cross sections for $a = 5$ mm.

1 mm half gap	PEC	CFC
k_{\perp}^{old} [V/Cm]	$9.31 \cdot 10^{14}$	$1.29 \cdot 10^{15}$
k_{\perp}^{new} [V/Cm]	$7.20 \cdot 10^{14}$	$1.15 \cdot 10^{15}$

Table 5.4. Kick factors results from GdfidL simulations of the double flat taper structure, for PEC and CFC materials, “old” and “new” angle set and 1 mm of half gap.

5 mm half gap	PEC	CFC
k_{\perp}^{old} [V/Cm]	$4.47 \cdot 10^{13}$	$4.87 \cdot 10^{13}$
k_{\perp}^{new} [V/Cm]	$2.17 \cdot 10^{13}$	$2.85 \cdot 10^{13}$

Table 5.5. Kick factors results from GdfidL simulations of the double flat taper structure, for PEC and CFC materials, “old” and “new” angle set and 5 mm of half gap.

5.2 TCS/TCT impedance study

In order to study the impedance behaviour of the new collimators and the effect of the ferrite blocks on HOMs, we performed detailed GdfidL wake fields simulations of the whole real structures. From the computational point of view, apart the introduction

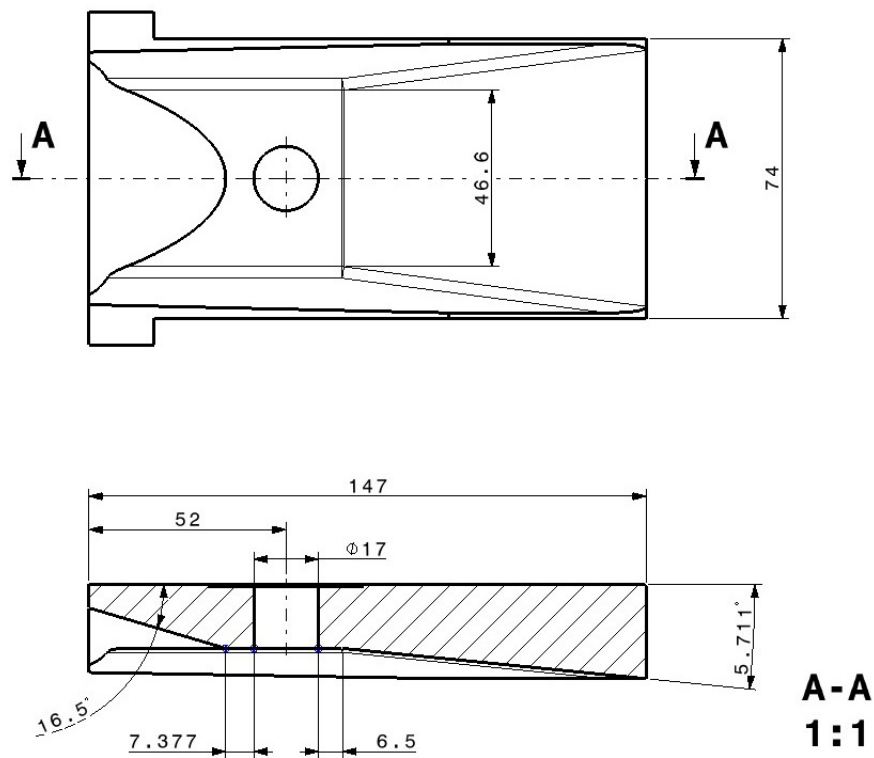


Figure 5.5. Mechanical drawing of the TCS/TCT prototype tapering region (courtesy of Luca Gentini, CERN).



Figure 5.6. The geometric model of the double flat taper as simulated into GdfidL.

of resistive and dispersive materials discussed so far, the most significant difference with the simulations of the LHC Run I collimators' structures was that no more symmetry planes were applicable, because of the asymmetric positioning of the ferrite blocks in the gaps between the jaws and the upper or lower plates (Fig. 5.1(a),

half gap [mm]	$Z_{\perp}^{old}/Z_{\perp}^{new}$	$ k_{\perp}^{old} / k_{\perp}^{new} $
1	≈ 3	≈ 1.3
5	≈ 2.6	≈ 2.1

Table 5.6. Estimated gain in RW transverse impedance and kick factor for the new collimator's tapering region, with respect to the old one.

Fig. 5.1(b) and Fig. 5.7). This fact implied the need to simulate the whole structure, thus in more simulation time needed.

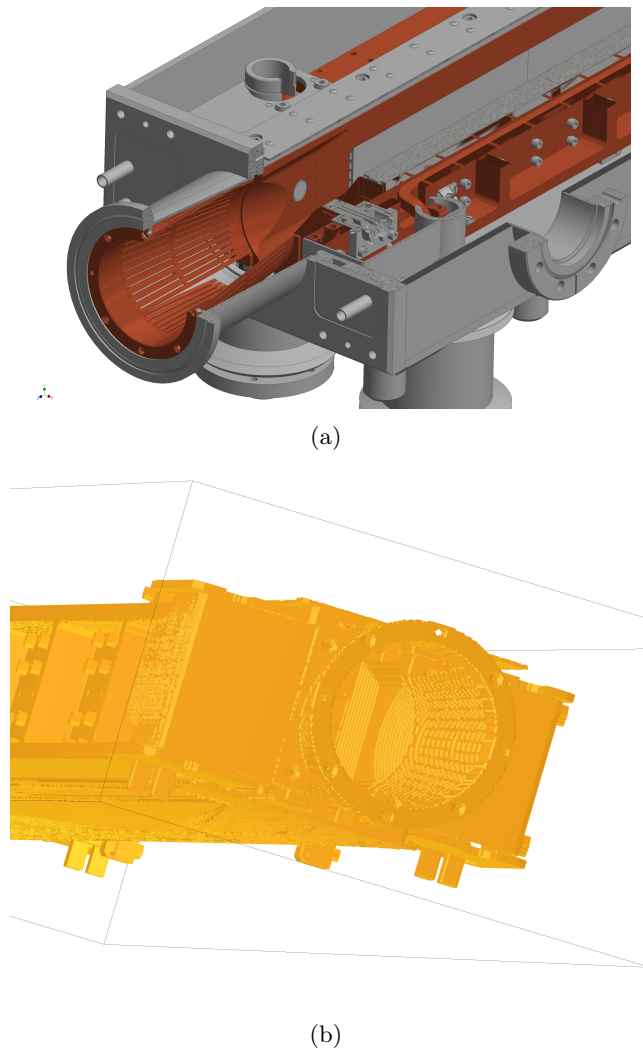


Figure 5.7. (a) the new BPM embedded TCS/TCT collimator CAD drawing for LHC Run II and (b) its elaboration into GdfidL.

The finite conductivity of W and the frequency-dependent permeability of TT2-111R were inserted into GdfidL input file. As a first result, an overall HOMs damping feature was demonstrated for the structure with resistive W jaws plus ferrite blocks at all frequencies [67]. This is clearly visible from the plot in Fig. 5.8 for the

longitudinal impedance. There, the red curve represents the collimator simulated as a whole with PEC material, without any resistive and dispersive material, while the black one represents the real collimator with W jaws and ferrite blocks. The

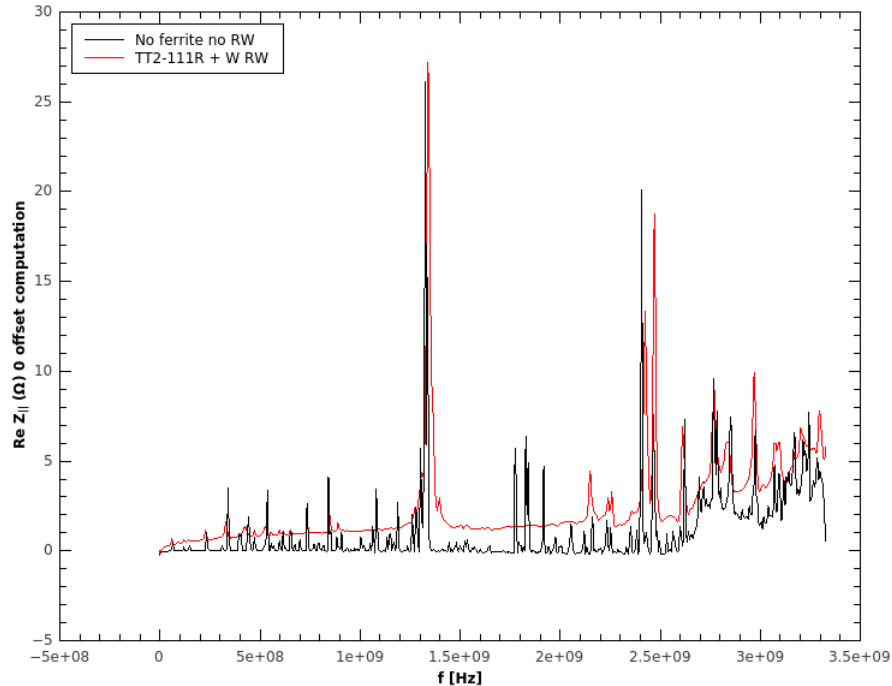


Figure 5.8. Longitudinal impedance for the new collimator as computed by GdfidL, with (red curve) and without (black curve) ferrite and resistive W.

results of Fig. 5.8 show that the longitudinal higher order modes till 1.2 GHz are heavily damped by the TT2-111R ferrite blocks and by the resistive contribution of the jaws. This is very important for the heating reduction of the collimators in the multibunch regime (for the nominal LHC bunches 7.5 cm long).

In order to discriminate the longitudinal or transverse nature of the measured HOMs that will be discussed below, the longitudinal impedance was computed by means of two GdfidL simulations, one with a zero beam transverse offset and the other with a non zero beam transverse offset. The results shown in the plot of Fig. 5.9 clearly demonstrate that the low frequency modes grow with the offset, thus clearly corresponding to transverse modes.

5.2.1 S_{1x} parameters simulations vs loop measurements

Before facing on the task of collimators detailed characterization in impedance, a wire impedance measurement simulation was performed with GdfidL. In addition to the collimator structure, a metallic (PEC) wire 0.25 mm in radius was modeled at the center axis of the collimator, between the jaws, performing a scattering parameters (reflection and transmission coefficients S_{11} and S_{12}) computation analogous to that of Chapter 4, for the simple coaxial probe. The computation involved collimator jaws at 3 mm of half gap, 1 mm mesh size and 4358 Million cells, ferrite blocks,

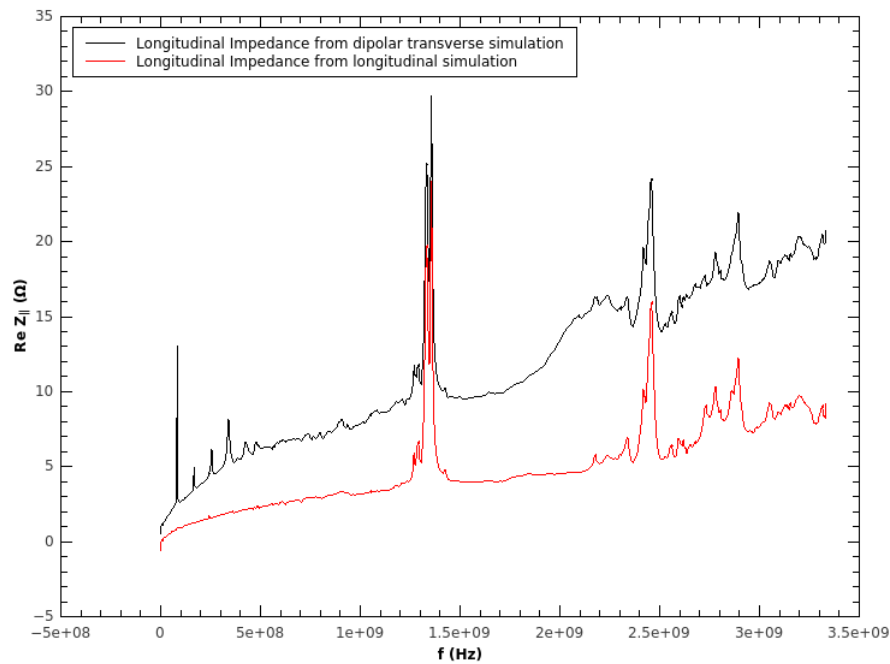


Figure 5.9. Longitudinal impedance for the new collimator, from longitudinal (zero beam offset) simulation and from transverse dipolar (non zero beam offset) simulation.

W IBC on all metallic surfaces and took 30 days on a 190 GB RAM, 32 cores, 4 Socket Opteron 6370P Server (courtesy of W. Bruns). The results are shown in Fig. 5.10(a), Fig. 5.10(b) and Table 5.7. While not resolved in the S_{12} spectrum

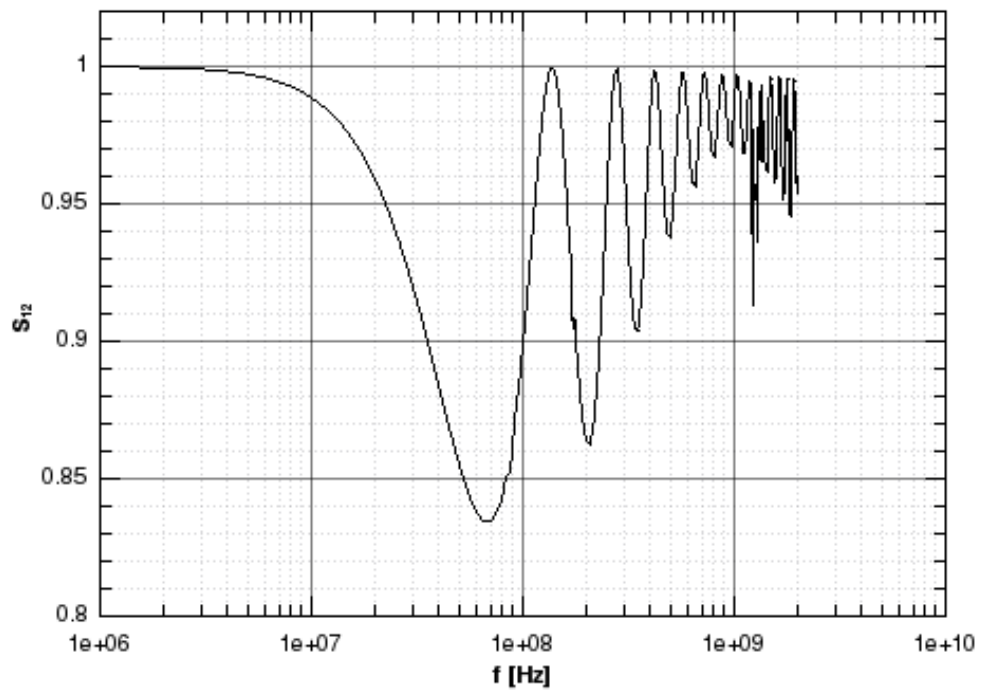
GdfidL computed modes	
i	f [MHz]
1	87.0
2	173.0
3	258.0

Table 5.7. Computed frequencies of the first three HOMs.

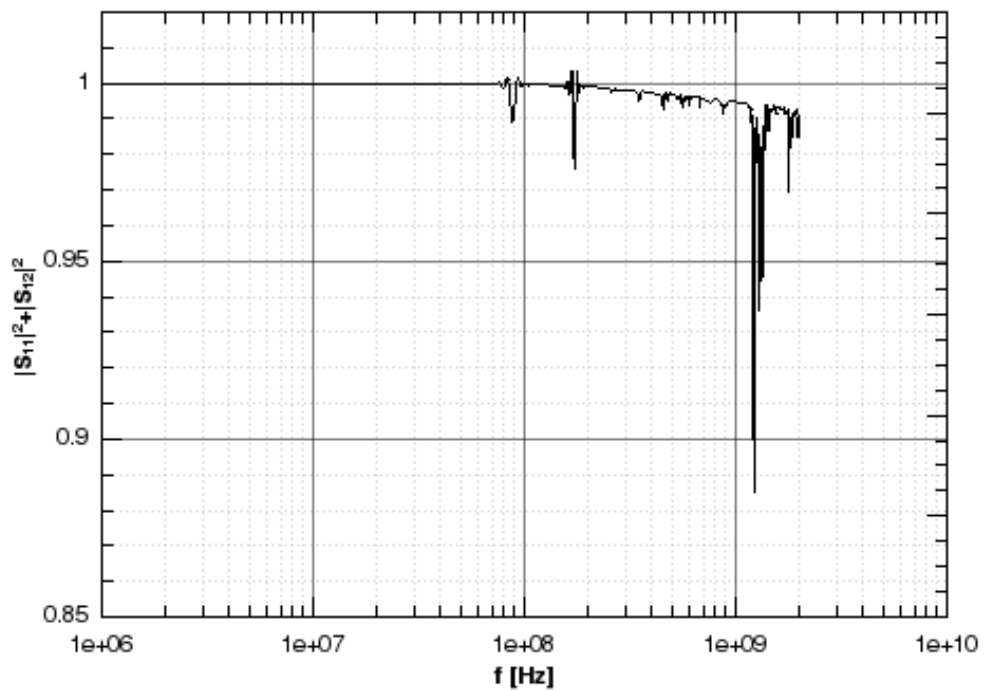
alone (Fig. 5.10(a)), the HOMs are clearly distinguished in the power sum spectrum (Fig. 5.10(b)), the first three laying at the frequencies listed in Table 5.7. Comparing these latter with the frequencies of the HOMs measured at CERN with loop technique [68], it came out already at this stage a very good agreement between the numerical calculations of the HOMs frequency spectrum and the measurements, assessing GdfidL simulations as a very reliable tool for further detailed impedance investigations.

5.2.2 Z_{\perp} simulations versus wire measurements

The transverse dipolar wakes and impedances of the LHC Run II TCS/TCT collimators' real structures were finally calculated by means of GdfidL simulations, for 3 mm and 8 mm of jaws' half gaps. Bearing in mind the aim at estimating the damping



(a)



(b)

Figure 5.10. (a) transmission coefficient and (b) power sum of reflection and transmission coefficients computed by means of the wire measurement GdfidL simulation.

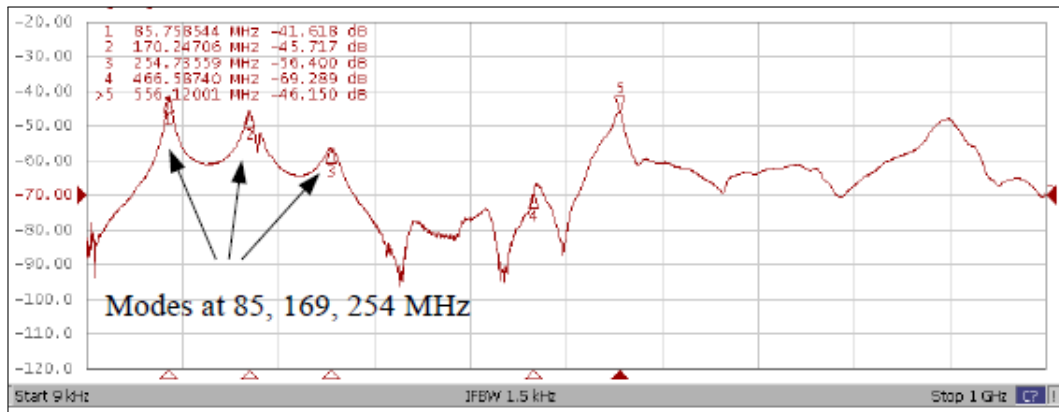


Figure 5.11. HOMs spectrum of the Run II collimator, measured with the loop technique (courtesy of N. Biancacci, CERN).

features of the ferrite blocks on HOMs, both structures with and without dispersive and properties of TT2-111R, but together with resistive W jaws, were considered. The results of such an extensive simulation campaign are shown in Fig. 5.12 and Fig. 5.13.

The wake field was traced up to $s = 200$ m. It came out that in the case of 3 mm half gap collimator, the wake with only W exhibited a worst decay over the traced wake length, with respect to the same computation for the case of 8 mm half gap (Fig. 5.12(a) and Fig. 5.13(a), respectively). In any case, a better wake decay was assured by the ferrite blocks for both geometries, as theoretically expected.

The TT2-111R ferrite resulted to be very effective in damping the transverse parasitic modes also, for frequencies above 500 MHz. The modes at lower frequencies are less damped, residual transverse HOMs at frequencies around 100 MHz and 200 MHz, with non-negligible shunt impedances still existing. This is clearly visible in the plots of Fig. 5.12(b) and Fig. 5.13(b). The confidence in GdfidL HOMs spectrum computation reliability, first dealt with in the previous section, was complied in this case also, with the calculated frequencies of the modes being in reasonable agreement with the loop measurements. The results are reported in Table 5.8. The effect

half-gap [mm]	HOMs			
	w/ TT2-111R		w/o TT2-111R	
	f [MHz]	R_s [M Ω /m]	f [MHz]	R_s [M Ω /m]
3	82.6	2.913	93.4	4.370
	167.2	0.485	181.1	0.797
8	84.7	0.239	95.7	0.340
	169	0.029	193.9	0.170

Table 5.8

of ferrite results also in the shift of HOMs characteristic frequencies toward lower ones. As an example, for 8 mm half gap, the first HOM frequency shifts from ≈ 95 MHz to ≈ 84.5 MHz, at exactly the same frequency measured experimentally at CERN with loop technique [68]. It is clear that the computed impedance spectrum

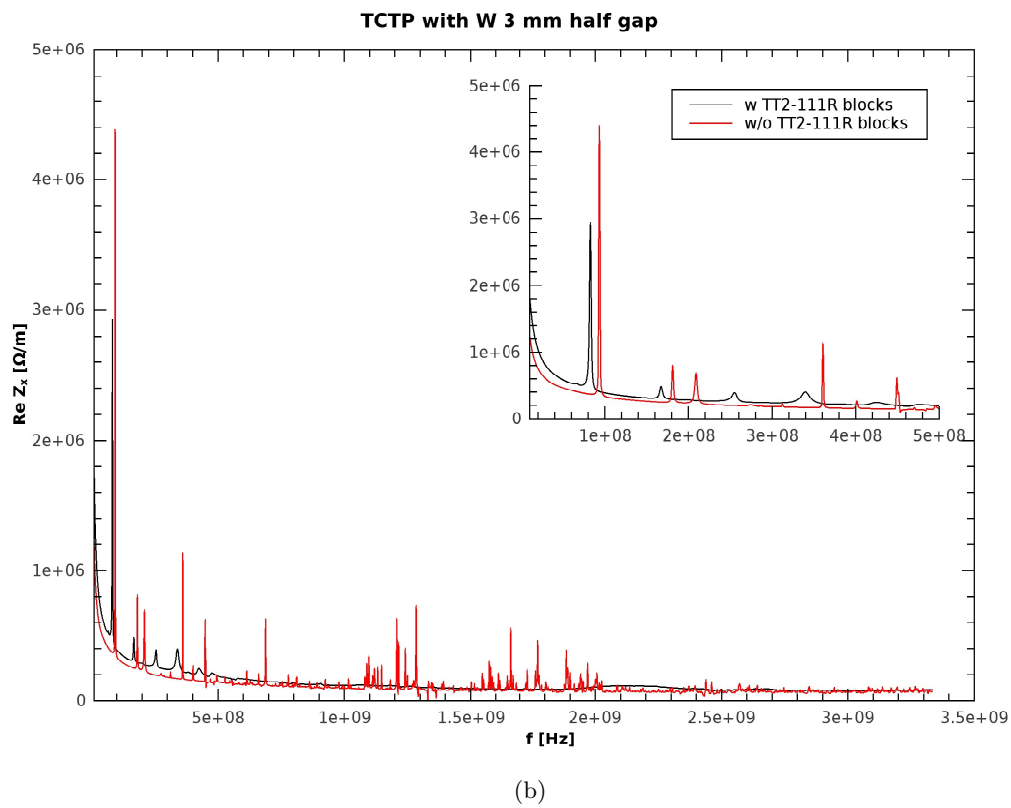
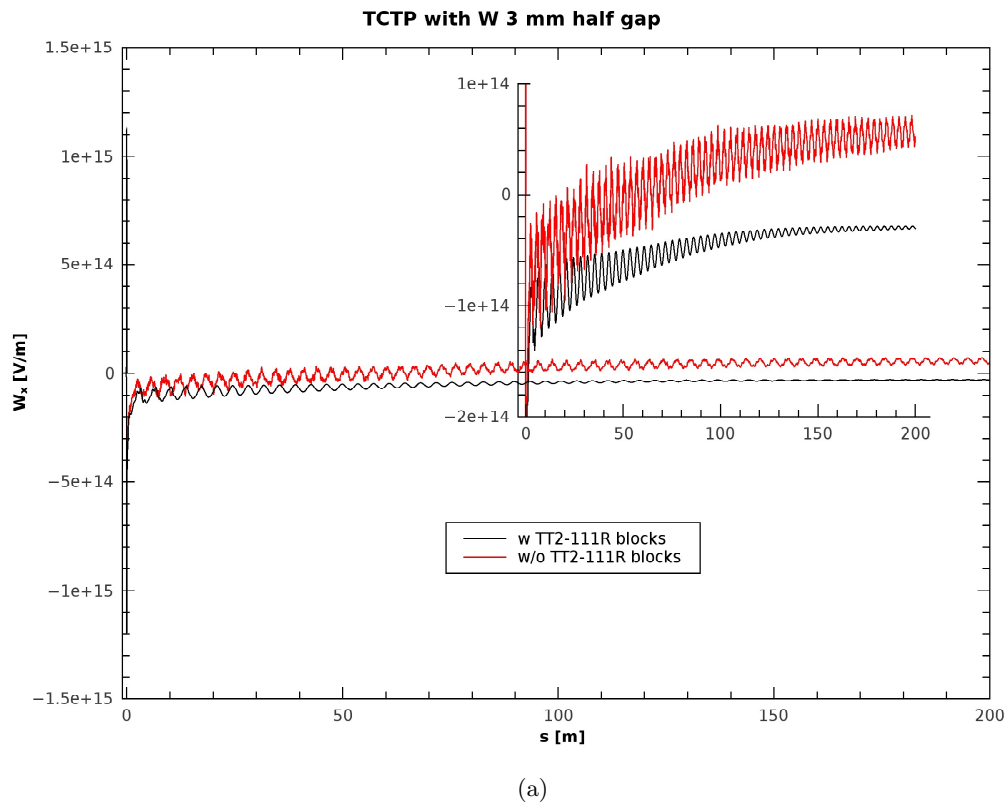


Figure 5.12. Transverse dipolar (a) wake and (b) real part of impedance spectrum of LHC Run II TCS/TCT collimators, with 3 mm of jaws' half gap. The impedance plot inset layer focuses on low frequency HOMs.

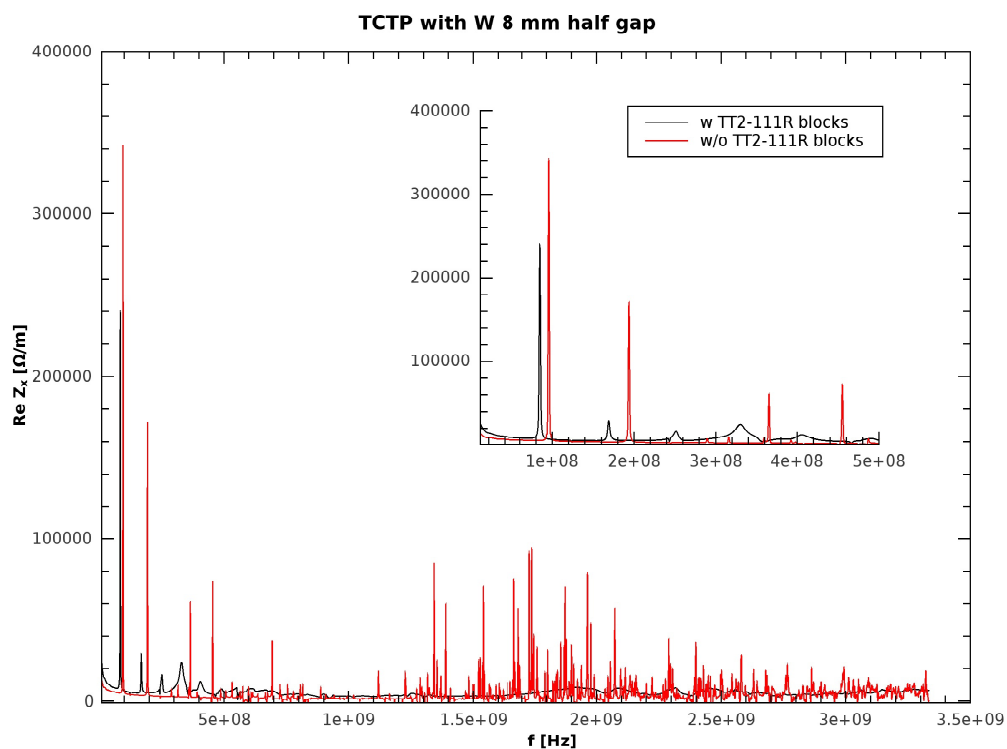
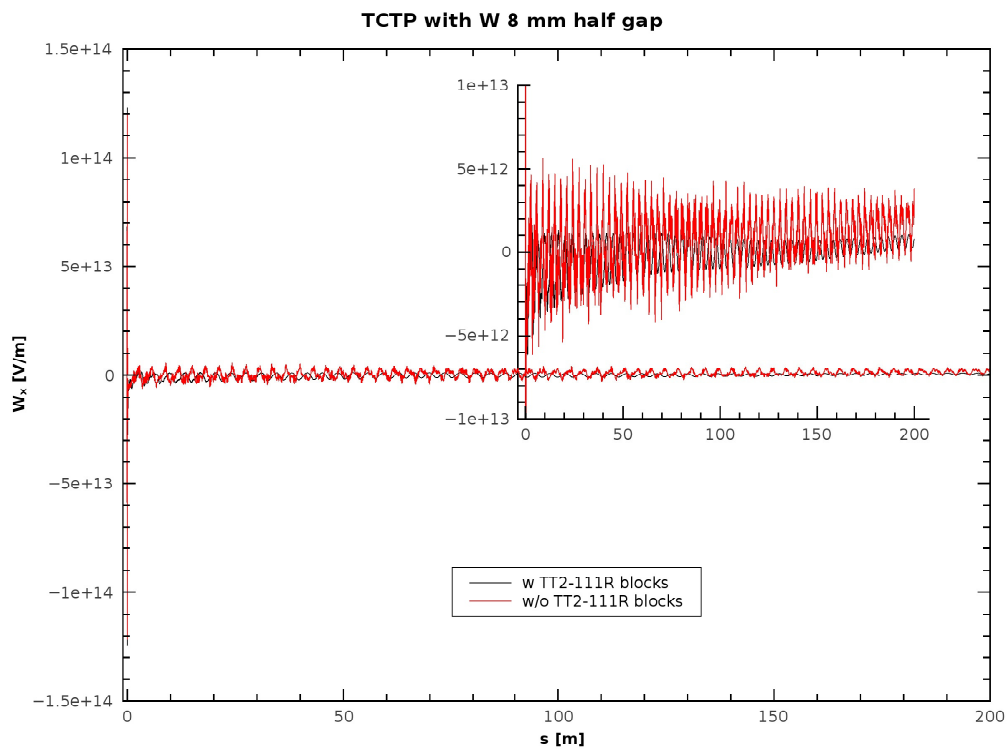


Figure 5.13. Transverse dipolar (a) wake and (b) real part of impedance spectrum of LHC Run II TCS/TCT collimators, with 8 mm of jaws' half gap. The impedance plot inset layer focuses on low frequency HOMs.

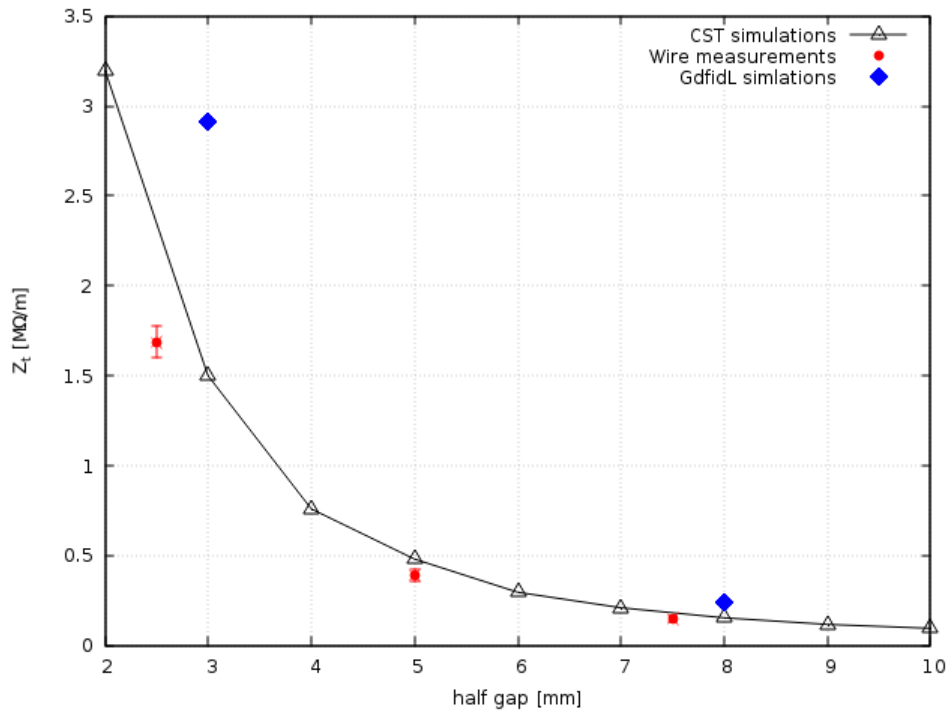


Figure 5.14. 1st HOM R_S as a function of jaws' half gap, as measured with wire technique and simulated in CST PS and GdfidL.

resolved very well the low frequency HOMs, whose characteristic frequencies are in excellent agreement with those found experimentally. Moreover, under these simulation circumstances, the computed shunt resistances of the first HOM at ≈ 84 MHz, for the two considered jaws' half gaps, is in remarkably agreement, within a factor of 2, with those measured experimentally with the wire technique at CERN [69]. This can be easily stated from Fig. 5.14, where the results from first HOM measurements, from CST PS and GdfidL simulations are plotted as a function of the jaws' half gap. For instance, in the case of 8 mm half gap $R_s^{sim} \approx 237 \text{ k}\Omega/\text{m}$ and $R_s^{meas} \approx 152 \text{ k}\Omega/\text{m}$ [70]. It is noteworthy to say that these small discrepancies may depend on several collimator design constraints, namely the gap between the plate where ferrite blocks are installed (HOMs' frequencies can shift of the order of tens percents), the gap between collimator jaws and external tank (which can affect the HOMs' R_s) and also on the mesh and computed wake length. There are good margins to be confident, however, that the results coming out from the GdfidL simulations presented so far could be more accurate, i.e. closer to the physical reality, with respect to both measurements and CST simulations. This is because it is well known that wire measurements perturb the field pattern inside a cavity like structure, leading to a broadening of the modes, in frequency, and to a lowering in R_s . The CST simulations, moreover, were performed with simplified models of the collimators, whereas the GdfidL ones with real models coming from CAD drawings, including all the structures' details, as it was already stressed several times in this thesis.

Chapter 6

LHC TDI collimators

The LHC injection protection system consists of a number of absorbers, aimed at intercepting the beam in case of failures of the LHC injection kicker magnets (MKI) [71]. It is going to be upgraded to prepare the higher intensity proton beam for the HL-LHC, process foreseen to be finished in the LHC LS II (2018-2019). In the case of MKI failures, the injection absorbers (TDIS) must be able to withstand the impact of a full injection train consisting of 288 bunches. Several materials for the absorber blocks are presently being considered, including different grades of boron nitride, graphite and carbon-reinforced-carbon, all having a low density, a low coefficient of thermal expansion, a high strength and a low Young's modulus [72]. Up to now, graphite R4550 seems to be a good compromise in terms of availability of shapes, machinability, costs and performances.

The preliminary TDIS design, shown in Fig. 6.1, is composed of three modules of equal length, containing different absorber materials, the first two of low Z absorber blocks (graphite R4550) and the third one of higher Z materials. The transverse

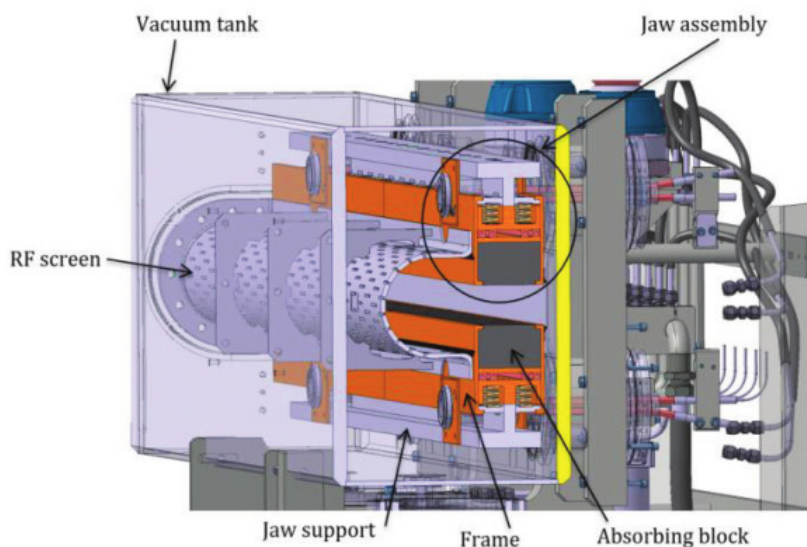


Figure 6.1. Preliminary design of one TDIS module [72].

dimensions of the absorber blocks are reported in Table 6.1, specifying the length

of a single module with and without tapering. The taper dimensions on either side depend on impedance calculations. The two TDI presently installed in LHC,

Parameter	Value
Block height	54 mm
Block width	58 mm
Active absorber length	1500 mm
Tapering length	100 mm
Tapering angle	10°
Total absorber length	1700 mm

Table 6.1. Dimensions of TDIS absorbers.

indeed, contribute significantly to both longitudinal and transverse impedances. It was indeed experimentally observed, by means of dedicated measurements during Run I [73, 74], beam induced heating causing high vacuum pressures that affected the background of the experiments. Thus a special care in the TDI design stage is needed, to minimize their impedances in view of the higher intensities planned for the LHC Run III and HL-LHC. This requires an impedance optimization study aimed at reducing geometric and resistive contributions. Such a study is still an ongoing work, even if several interesting results were obtained up to now, from a dedicated impedance simulations' campaign with GdfidL code.

6.1 TDI taper optimization study

The TDI's jaws presently installed in the LHC consist of one linear taper plus a sharp discontinuity, as shown in Fig. 6.2, where the GdfidL model is reported. In view of

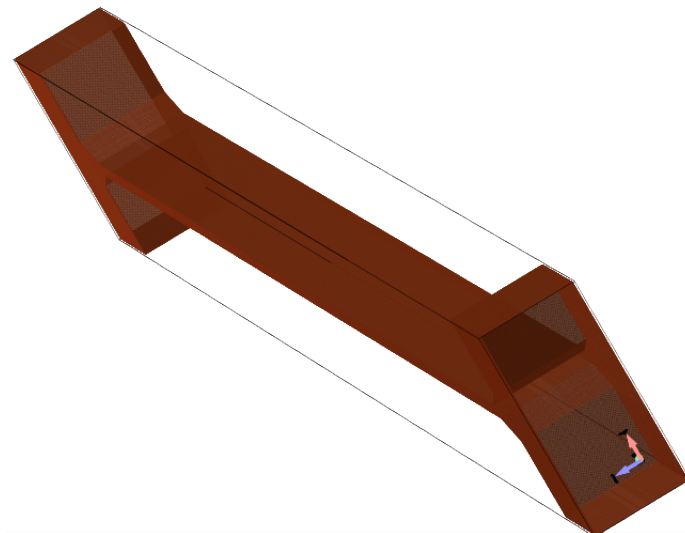


Figure 6.2. Jaw's geometry of the TDI presently installed in the LHC, as modeled into GdfidL.

the needed upgrade discussed at the beginning of the chapter, the LHC collimation

team proposed a new taper geometry consisting of a simple linear flat taper, as shown in Fig. 6.3 for the GdfidL model, in order to avoid the strong impedance of the type step in - step out [29, 27] due to the sharp discontinuity. The possibility to

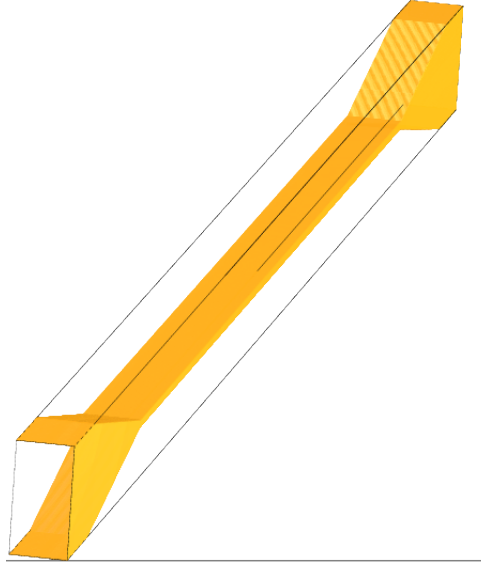


Figure 6.3. Linear jaw's geometry of the TDI, as modeled into GdfidL.

minimize the impedance of a taper was studied in 2007 [75], by a nonlinear geometry described by a function of the type

$$h(z) = \frac{h_{min}}{[1 + zL(\beta^{-\frac{1}{2}} - 1)]^2}, \quad (6.1)$$

where $h(z)$ is the varying half height, z the longitudinal variable, h_{min} and h_{max} the lower and upper height limits, L the taper length and $\beta \equiv \frac{h_{max}}{h_{min}}$. Such a geometry was modeled into GdfidL, as shown in Fig. 6.4, and proposed as a substitute of both the sharp and linear taper geometry for the TDI design upgrade. In all the above

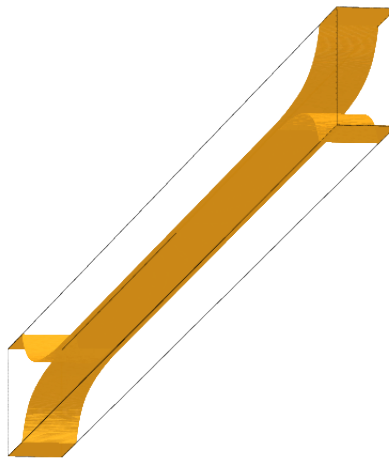


Figure 6.4. Nonlinear jaw's geometry of the TDI, as modeled into GdfidL.

taper GdfidL models, additional 10 cm in and out tubes were placed “ad-hoc”, to guarantee numerical stability of the computation.

Thus GdfidL simulations of geometric and RW transverse broad-band impedances, longitudinal and transverse loss factors, of the above TDI jaws were carried out, tracing the wake field over a length $s = 75$ cm, driving a beam with a bunch length $\sigma_z = 7.5$ cm. The RW contributions were computed for the R4550 graphite. Simulations' results are listed in Table 6.2, where the “NEW geometry” refers to the linear one proposed by the LHC collimation team and the “Alternative geometry” to the nonlinear one, whose proposal originated from the study being described here. It is evident that, from the impedance point of view only, the best geometry

PRESENT geometry (linear flat taper + sharp discontinuity)		
	PEC	R4550 graphite ($\sigma_\infty = 7.64 \cdot 10^4$ S/m)
k_{\parallel} [V/C]	$1.73 \cdot 10^9$	$2.59 \cdot 10^9$
$Z_{\perp}(0)$ [k Ω /m]	49.4	123.1
k_{\perp} [V/Cm]	$5.32 \cdot 10^{13}$	$1.37 \cdot 10^{14}$
NEW geometry (only longer and higher linear flat taper)		
	PEC	R4550 graphite ($\sigma_\infty = 7.64 \cdot 10^4$ S/m)
k_{\parallel} [V/C]	$1.59 \cdot 10^9$	$2.69 \cdot 10^9$
$Z_{\perp}(0)$ [k Ω /m]	31.9	109.6
k_{\perp} [V/Cm]	$3.46 \cdot 10^{13}$	$1.21 \cdot 10^{14}$
Alternative geometry (non linear taper)		
	PEC	R4550 graphite ($\sigma_\infty = 7.64 \cdot 10^4$ S/m)
k_{\parallel} [V/C]	$1.61 \cdot 10^9$	$2.82 \cdot 10^9$
$Z_{\perp}(0)$ [k Ω /m]	19.98	102
k_{\perp} [V/Cm]	$2.09 \cdot 10^{13}$	$1.11 \cdot 10^{14}$

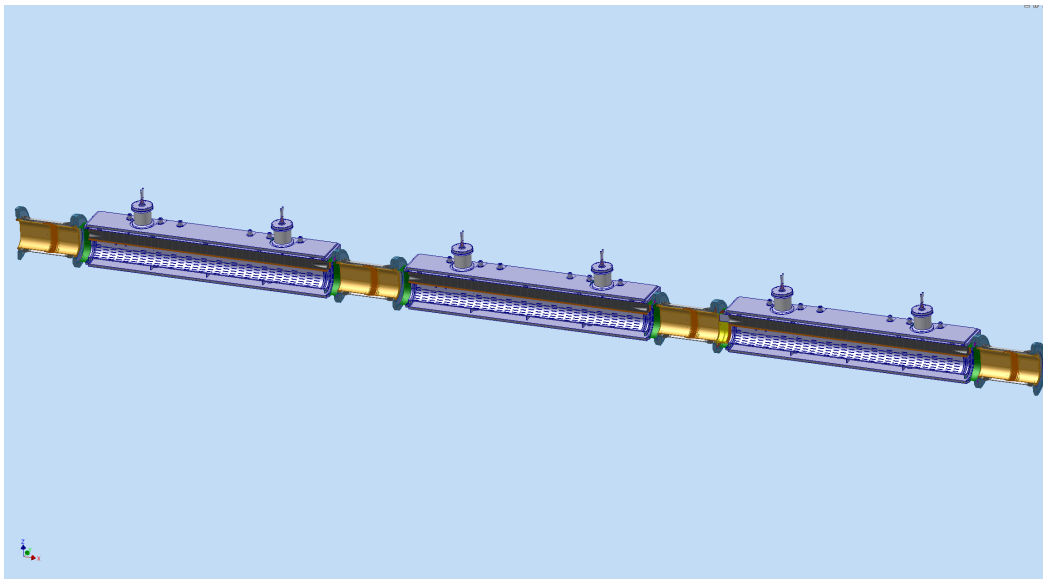
Table 6.2. Resulting transverse impedance, longitudinal and transverse loss factors from GdfidL simulations of the three jaws' tapers geometries.

for TDI collimator taper is the non linear one. A significant reduction, indeed, of a factor ≈ 2.5 in both zero frequency impedance and kick factor, with respect to the present TDI geometry, is estimated for the geometric contributions. For the RW contribution, instead, the reduction accounts only for a factor ≈ 1.2 . The geometrical longitudinal loss factor is observed to not change significantly, although a very tiny increase of the longitudinal loss factor, of about 9%, is expected.

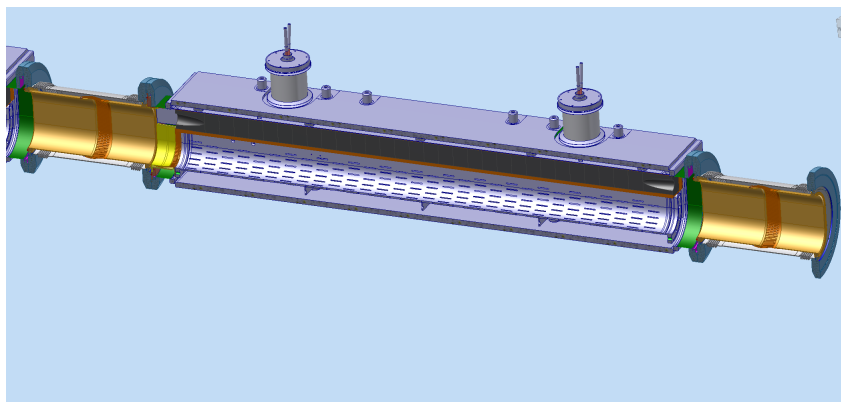
6.2 TDIS' real structures impedance study

The impedance study for the TDIS' real structures is still an ongoing work. Nevertheless, several interesting preliminary results have been obtained so far.

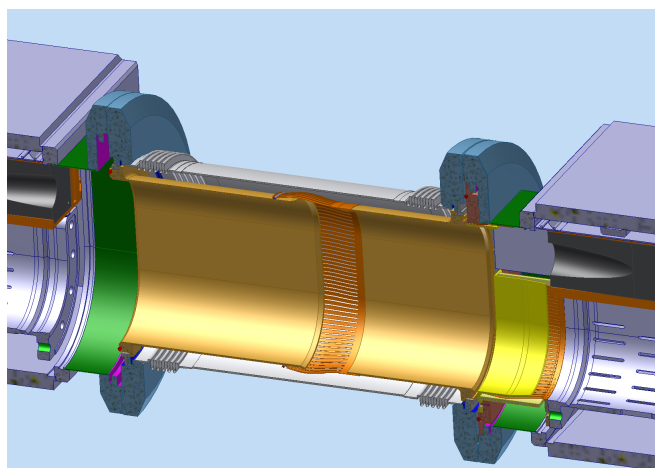
A first upgraded TDIS model was conceived by the CERN EN-MME department [76], whose CAD drawings are shown in Fig. 6.5. They represent a very complicated structure of about 3 m length, in which the jaws' tapers have an elliptical round geometry. The reproduction of the corresponding STL files, again without any simplification, into GdfidL is shown in Fig. 6.6. Any structural detail is very well



(a)



(b)



(c)

Figure 6.5. CAD drawings for the first upgraded model of the TDIS collimator.

resolved, even if a less fine mesh, with respect to the collimators simulated so far, of 1 mm in x, y directions and 0.5 mm in z was used. Due to the very long design, with

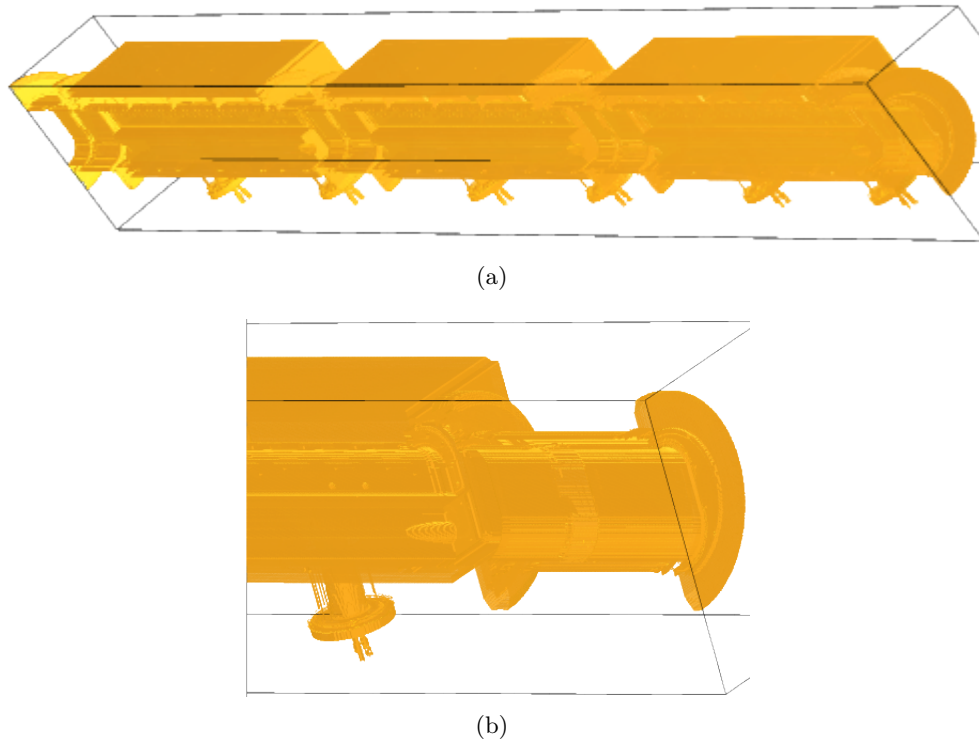
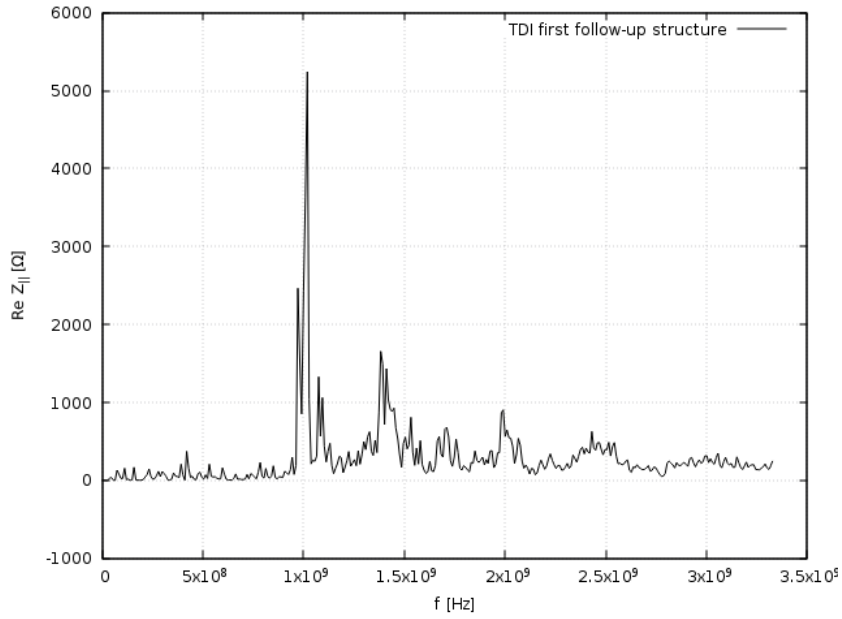


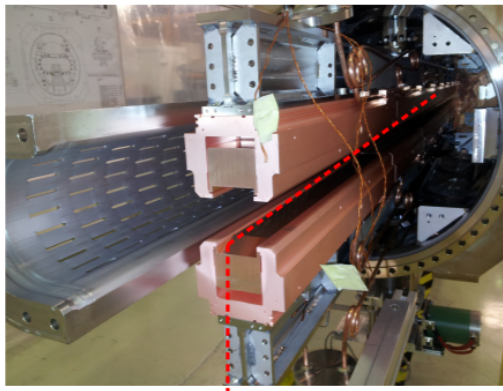
Figure 6.6. GdfidL elaboration of the first upgraded CAD model of the TDIS collimator.

many gaps, flanges, pumps and pipe interconnections, it was possible up to now to compute the geometric longitudinal impedance only, with the available computing resources of *EngPara*, truncating the wake at most over a length $s = 50$ m. The results for the real part of the longitudinal impedance are plotted in Fig. 6.7(a), for the TDI with 25 mm of jaws' half gap. They were quite encouraging already at this stage. Dedicated impedance measurements with wire technique, performed at CERN, revealed indeed the presence of many harmful trapped modes [77].

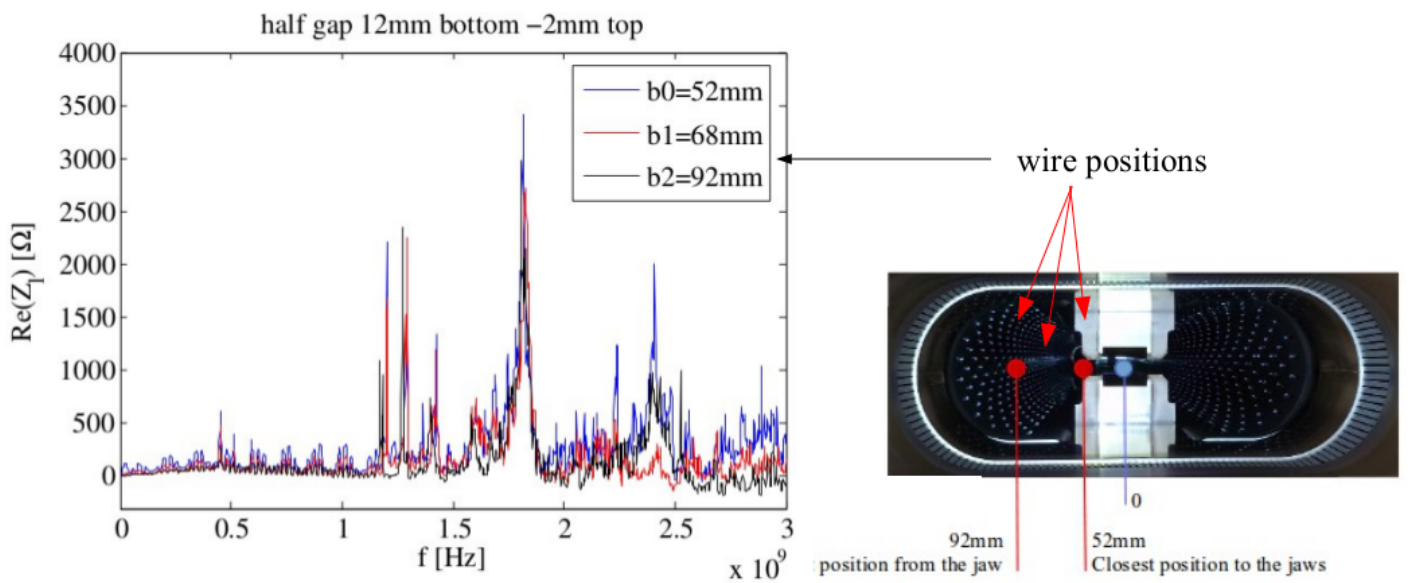
A comparison of the simulated impedance with the experimental one shown in Fig. 6.7, exhibit qualitatively a very similar impedance pattern. The measurements were done on the whole TDI structure, including Hexagona Boron Nitride (hBN) coated blocks and the two Al+Cu and Cu blocks. The upper jaw was moved to -2 mm below the geometrical center and the lower jaw to 12 mm, thus with a full gap of 10 mm. The simulated structure, on the other side, had an half gap of ± 25 mm, thus a full gap of 50 mm. What is observed from the comparison in Fig. 6.7, is that a small impedance peak is computed at $f \approx 0.5$ GHz, high narrow peaks in the range $1 \text{ GHz} \lesssim f \lesssim 1.1 \text{ GHz}$, a wider peak at $f \approx 1.5$ GHz and broader peaks with smaller amplitudes at higher frequencies. This is an important result, given that a) the simulations were performed for the geometric impedance only, while measurements were done on the real collimator with all resistive and dispersive materials, b) the measurements with wire technique can lead to HOMs frequencies shift toward higher values and c) the HOMs tend to have lower frequencies for wider gaps.



(a)



(b)



(c)

Figure 6.7. (a) TDIS geometric longitudinal impedance from GdfidL simulation, for 25 mm half gap, (b) TDIS longitudinal measurement experimental setup and (c) measurement results.

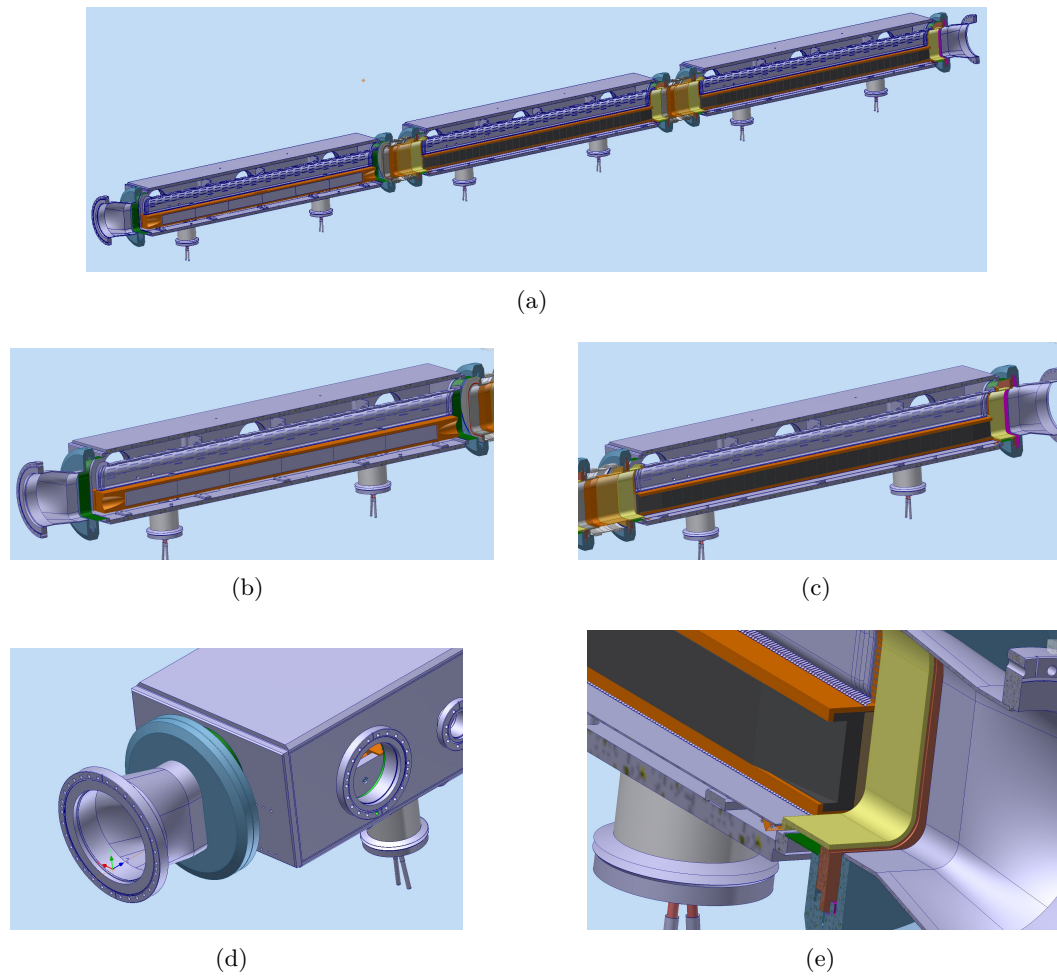


Figure 6.8. CAD drawings for the second upgraded model of the TDIS collimator.

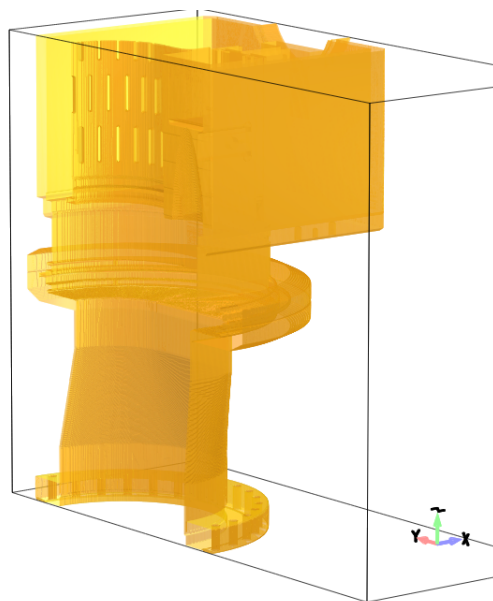


Figure 6.9. GdfidL elaboration of the second upgraded CAD model of the TDIS collimator.

A second upgraded TDIS design [76] was simulated, whose CAD drawings are shown in Fig. 6.8. The whole structure (Fig. 6.8(a)) was revised with respect to the previous one, changing the jaws' material of the first block only and leaving the other two blocks the same (Fig. 6.8(b) and Fig. 6.8(c)), modeling asymmetrically the input and output pipes (Fig. 6.8(d)) and leaving the jaws' elliptical round taper on the first block only, modifying the other two blocks with flat rectangular taper jaws (Fig. 6.8(e)). Moreover, the modules interconnections were not oval anymore, but it was cut on one side due to specific request of the team computing the radiation to equipment and resulting potential damage [78]. A detailed view of the tapering region, of the GdfidL simulated geometry, is shown in Fig. 6.9.

The geometric longitudinal wake field traced over a length of about 30 m and the corresponding real and imaginary parts of the impedance are shown in Fig. 6.10 and Fig. 6.11, respectively, together with the corresponding results for the first model discussed before.

As a first comment, it is seen from Fig. 6.10 that in this second case it was possible to obtain the wake field computed up to $s \approx 25$ m only. This can probably explain the impedance HOMs splitting appearing at around 750 MHz. Both from real and imaginary parts of the impedance plotted in Fig. 6.11(a) and Fig. 6.11(b), however, it can be concluded that a significant improvement was achieved, from the geometric longitudinal impedance point of view, with the new upgraded TDIS model. A loss factor reduction of $\sim 29\%$ has been achieved in this case, as it resulted from computations to be $7.14 \cdot 10^{11}$ V/C for the first model and $5.04 \cdot 10^{11}$ V/C for the new one. Moreover, the strong modes at around 1 GHz are heavily damped, but HOMs appear to be strongly damped at almost all frequencies, what is the most critical goal in view of the beam induced overheating reduction efforts. Its overcoming by means of careful TDIS design, minimizing the impedance characterizing it in detail, still deserves further investigations and dedicated extensive simulation campaigns.

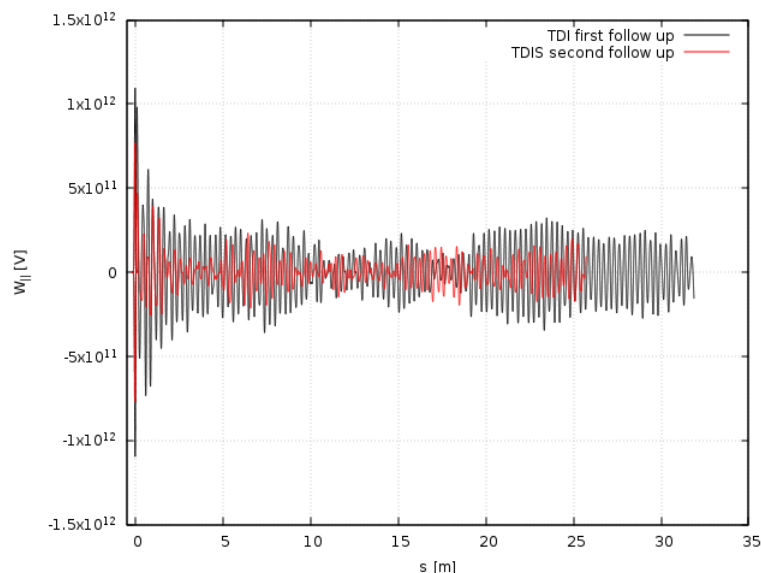


Figure 6.10. Longitudinal wake field comparison for the first and second TDIS upgraded models.

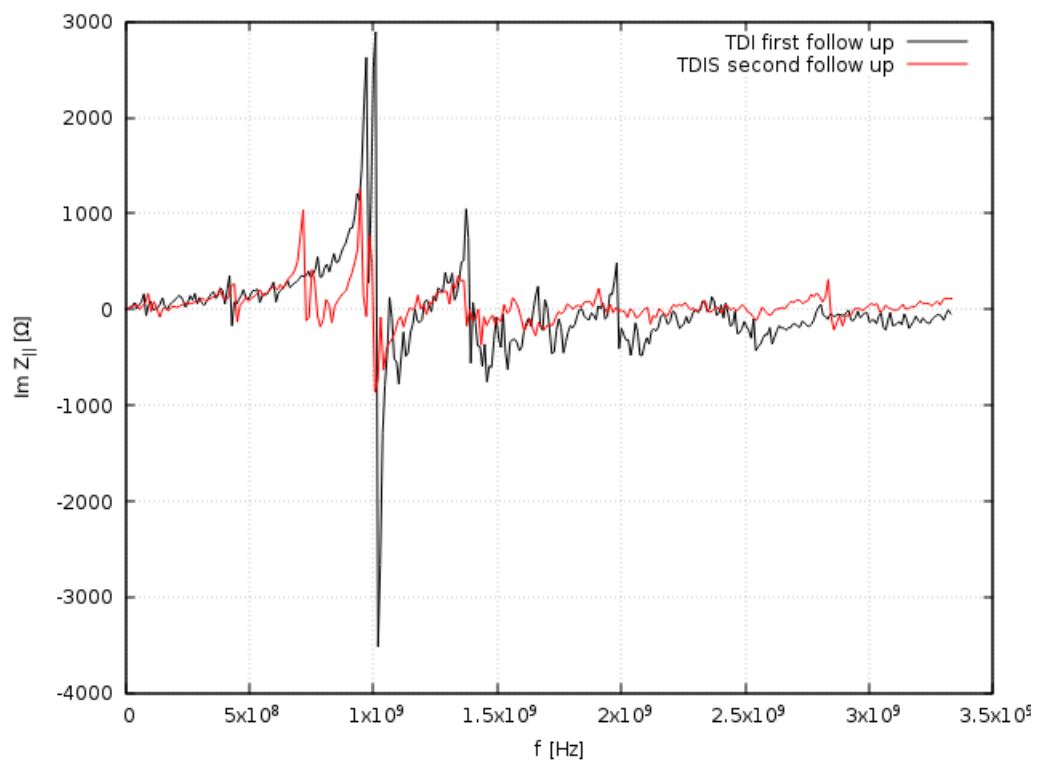
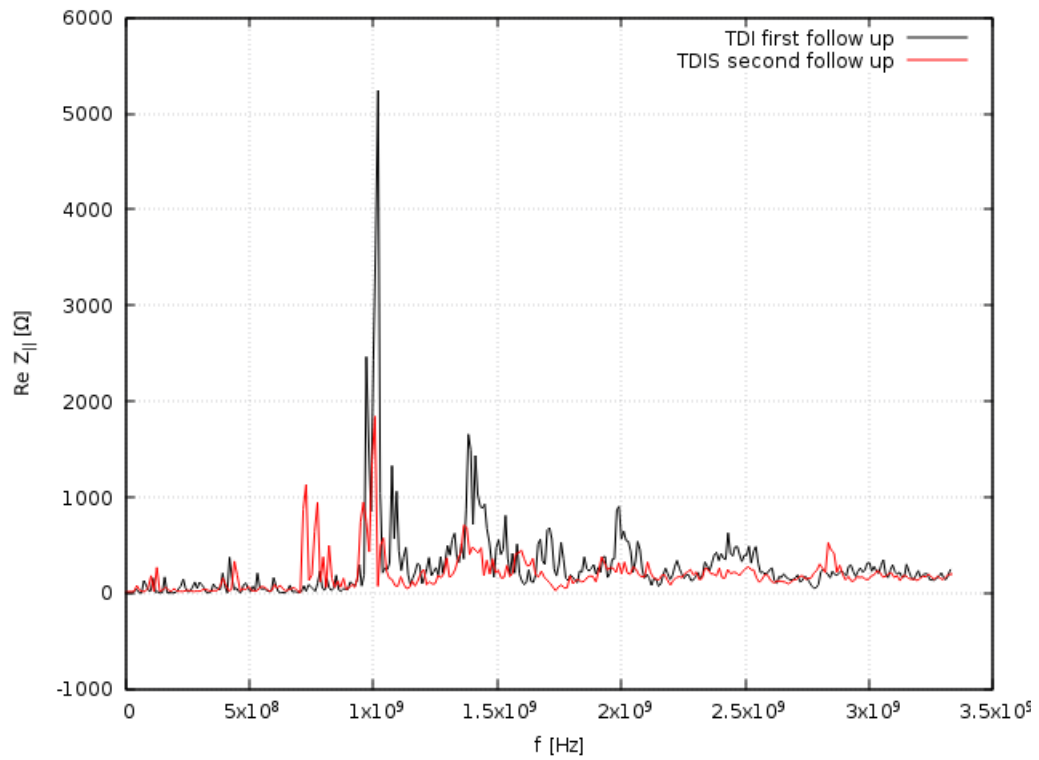


Figure 6.11. Comparison between the longitudinal (a) real and (b) imaginary parts of the impedance, for the first and second TDIS upgraded models.

Chapter 7

Conclusions

Numerical simulations of wake fields and impedances were carried out for 3 different kinds of LHC collimators: LHC Run I TCS/TCT collimators without BPM pickup buttons, LHC Run II TCS/TCT collimators with BPMs and TDI injection collimators, by means of GdfidL electromagnetic code. For the first time in the field of impedance computations, a complete and detailed simulation campaign of collimators' real structures, including the properties of real and lossy dissipative materials (CFC and W resistive walls, TT2-111R ferrite). This task was accomplished using huge real CAD (STL) designs and the GdfidL parallelization on the CERN *Engpara* dedicated cluster. For this purpose several benchmark numerical tests were performed for resistive walls and TT2-111R ferrite, using parallel computing with GdfidL code engaging billions of mesh points. The performed numerical tests have confirmed that GdfidL reproduces very well the properties of the lossy dispersive materials. The simulation test results for the resistive walls and the lossy ferrites are in a good agreement with available analytical formulae and the results of other numerical codes and semi-analytical models.

For LHC Run I TCS/TCT collimators, the comparison of the transverse kick factors calculated for five different jaws' half gaps, has shown that the geometric impedance contribution is not negligible with respect to the resistive wall one. The study has contributed to the refinement of the LHC impedance model, as a result of the geometrical collimator impedance accounting for approximately 30% of the total LHC impedance budget, at frequencies close to 1 GHz.

For the LHC Run II TCS/TCT collimators, the numerical studies of the impedance have shown that the longitudinal higher order modes till 1.2 GHz are heavily damped by the TT2-111R ferrite blocks and by the resistive contribution of the jaws. This is very important for the heating reduction of the collimators in the multibunch regime (for the nominal LHC bunches 7.5 cm long). The transverse modes at low frequencies are less damped, there are still residual transverse HOMs at frequencies around 100 MHz and 200 MHz with non-negligible shunt impedances. The calculated frequencies of the modes are in remarkable agreement with the loop measurements. The shunt impedances of the modes obtained numerically agree within a factor of 2 with the experimental data of the wire measurements performed by the CERN impedance group. Moreover, the broad-band transverse impedance of the new double taper collimators are evaluated to be approximately by 20% higher

with respect to that of the single taper secondary collimators.

The taper's shape of the TDI collimator jaws was optimized, including the geometric impedance and resistive walls. It was shown that, from the impedance point of view, the best geometry is the non linear one. A significant reduction in both zero frequency impedance and kick factor, with respect to the present TDI geometry, was calculated for both the geometric and resistive wall contributions, although a tiny increase of the longitudinal loss factor is expected.

Detailed TDI's real structure impedance study is still an ongoing work. However good and encouraging preliminary results were gained already at this stage. For instance, computed HOMs' pattern in geometrical longitudinal impedance is very similar to that found experimentally by means of wire measurements performed at CERN, taking into account the different conditions between simulations and measurements. This is very important in view of the next detailed HOMs characterization like that performed for Run II TCS/TCT collimators. For the second follow up TDI model the simulations results show an estimated reduction of about 29% in the loss factor, and a significantly reduced longitudinal impedance.

Appendix A

The linear accelerator model

A circular accelerator can be modeled as in Fig. 2.1, with the beam circulating inside a metallic vacuum chamber, of varying cross section, on a trajectory of circumference $2\pi R$. Given the simple harmonic oscillators describing the unperturbed single particle motion, in the x , y , z directions with angular frequencies ω_{x0} , ω_{y0} and ω_{z0} , the tunes ν_{x0} , ν_{y0} and ν_{z0} can be defined as these frequencies divided by the synchronous particle¹ revolution frequency ω_0 . It results, in general, $\nu_{x0}, \nu_{y0} \gg 1$ and $\nu_{z0} \ll 1$.

All other particles' motion is described in a six dimensional phase space, whose coordinates are $(x, x', y, y', z, \delta)$. The coordinates $x' = dx / ds$ and $y' = dy / ds$ are the slopes of the horizontal and vertical coordinates of the particle with respect to the reference orbit, whereas $\delta = \Delta P / P$ is the relative momentum error of the particle. The unperturbed equation of motions for single particles are

$$x'' + \left(\frac{\nu_{x0}}{R}\right)^2 x = 0, \quad (\text{A.1})$$

$$y'' + \left(\frac{\nu_{y0}}{R}\right)^2 y = 0, \quad (\text{A.2})$$

$$z' = -\eta\delta, \quad (\text{A.3})$$

$$\delta' = 0, \text{ for unbunched beams,} \quad (\text{A.4})$$

$$\delta' = \frac{1}{\eta} \left(\frac{\nu_{s0}}{R}\right)^2 z, \text{ for bunched beams,} \quad (\text{A.5})$$

where a prime indicates the derivative with respect to s . In the above equations the slippage factor has been defined as

$$\eta = \alpha - \frac{1}{\gamma^2}, \quad (\text{A.6})$$

where α is the momentum compaction factor, usually positive in accelerator rings²,

¹With synchronous particle the reference particle O of Fig. 2.1 is concerned, which has exactly the design energy and stays on the design orbit in the accelerator. Its trajectory is designated by the coordinate s , which is a time variable.

²There are also rings for which $\alpha < 0$, e.g. the Low Energy Antiproton Ring (LEAR) at CERN, where lower momentum particles have longer closed orbits or larger radial excursions than higher momentum particles. A negative momentum compaction factor does imply an imaginary transition energy, thus an always negative slippage factor and a ring always below transition.

and γ the relativistic Lorentz factor. The first two eqs. A.1 and A.2 describe the simple harmonic property of the transverse betatron oscillations of the particles. Usually the transverse tunes are related to the transverse β functions of the machine optics [28] as

$$\nu_{x0} = \frac{R}{\beta_x} \text{ and } \nu_{y0} = \frac{R}{\beta_y}, \quad (\text{A.7})$$

where $2\pi\beta_{x,y}$ are the betatron oscillation wavelengths.

For $\gamma \rightarrow \infty$, the slippage factor $\eta \approx \alpha$ and $\eta > 0$. For $\gamma < \gamma_{tr} \equiv 1/\sqrt{\alpha}$, known as transition energy, η becomes negative. The above condition is commonly referred to as “below transition” and is usually a property of low energy hadron rings, while the opposite one $\gamma > \gamma_{tr}$ as “above transition”, mostly encountered in electron rings and high energy proton rings, in which the particle velocity $v \approx c$. At transition, $\eta = 0$, the particles’ dynamics in the longitudinal phase space freezes; under this circumstances the beam is most vulnerable to perturbations. When an accelerator is operated below transition, any particle with an energy slightly higher than the reference one ($\delta > 0$) will have its longitudinal coordinate increasing with time, i.e. $z' > 0$. Above transition, instead, any particle with an energy higher than the reference one will slow down, with $z' < 0$, even if its velocity is higher than that of the synchronous particle. This phenomenon is called the negative mass effect and relies on the fact that particles with higher energies, with respect to the synchronous particle, must circulate in the accelerator on larger orbits.

The longitudinal synchrotron oscillation can be obtained combining eqs. A.3 and A.5 for bunched beams,

$$z'' + \left(\frac{\nu_{s0}}{R}\right)^2 z = 0, \quad (\text{A.8})$$

whereas it is trivial to mention that for unbunched beams no longitudinal focusing does occur.

Equations A.1-A.5 describe the linear accelerator model and the unperturbed motions of beam particles. Let a perturbation affect, for example, the focusing in the y direction, being the perturbation linear in y :

$$y'' + \left(\frac{\nu_{y0}}{R}\right)^2 y = Ky. \quad (\text{A.9})$$

The perturbed motion can be described by a perturbed tune

$$\nu_y^2 = \nu_{y0}^2 - KR^2, \quad (\text{A.10})$$

from which it can be deduced that for small perturbation, $|KR^2| \ll \nu_{y0}^2$, the tune has shifted by an amount

$$\Delta\nu_y = \nu_y - \nu_{y0} = -\frac{KR^2}{2\nu_{y0}}. \quad (\text{A.11})$$

This result would have been identical in the case of a linear perturbation in x . The quantity $\Delta\nu$ is known as *tune shift* and plays a crucial role in the study of collective effects. For perturbations driven by collective electromagnetic fields, the tune shifts are generally complex.

Appendix B

The GdfidL Finite Difference code

GdfidL is a Finite Difference Time Domain (FDTD) code that solves approximately Maxwell's equations by means of the curl operators discretization. For homogeneous materials the process follows the Yee's algorithm [79]. For non homogeneous dielectric or permeable materials, the discretization is performed based on the Weiland method [80]. The program is composed of two field solvers, one that computes resonant fields in loss-free structures and the other that computes time dependent fields, scattering parameters and wake potentials in lossy or loss-free structures [81]. Its main advantage is the grid cells being needed only in regions which are not filled with electric or magnetic conducting materials, what has as a consequence a reduction in memory and CPU usage.

The discretization of the curl operators allows to compute the time derivative of a field component in a grid, from the values of the four surrounding dual components. Let each field component in the computational volume have a triple index i, j, k , the resulting difference equations in loss-free regions are approximated as (here the $\frac{d}{dt}H_z$ component is taken as an example)

$$\frac{d}{dt}H_z^{i,j,k} \approx \frac{\Delta_x(E_x^{i+1,j,k} - E_x^{i,j,k}) + \Delta_y(E_y^{i+1,j,k} - E_y^{i,j,k})}{\Delta_x\Delta_y}. \quad (\text{B.1})$$

Despite of being quite simple to implement in a computer code, this difference equation has the disadvantage of assigning grid cells also to regions where the material is ideal conducting, what makes managing computational volumes, in which many geometries are present, particularly resource demanding.

The approach of GdfidL is quite different. Instead of using a triple index to identify a field component in the computational volume, the indices $n_x^+(l)$ and $n_y^+(l)$ are introduced, for the neighbour cell in the positive x or y directions of the l -th cell, as in Fig. B.1. Thus the equation for the $\frac{d}{dt}H_z$ field component now reads

$$\frac{d}{dt}H_z^l \approx \frac{\Delta_x(E_x^{n_x^+(l)} - E_x^l) + \Delta_y(E_y^{n_y^+(l)} - E_y^l)}{\Delta_x\Delta_y}. \quad (\text{B.2})$$

Let \vec{h} and \vec{e} be arithmetic vectors denoting the discrete electromagnetic degrees of freedom (i.e. all the field components of \vec{E} and \vec{H}), then the equations for all the

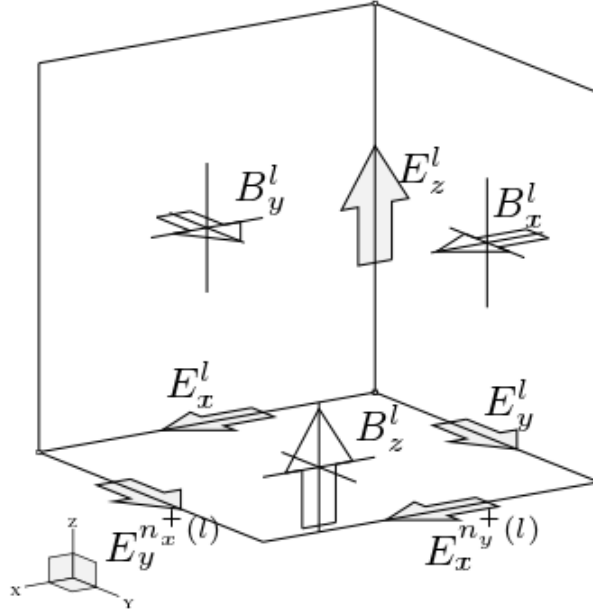


Figure B.1. The l -th gridcell with its six field components. Additionally the two field components of neighbour cells are shown, which are needed to compute the curl of \vec{E} at the position of H_z^l (the field components of H are denoted by B in this picture) [81].

components of \vec{H} in the computational volume, similar to eq. B.2, can be written in matrix form as

$$\frac{d}{dt}\vec{h} = -\mathbf{C}^e\vec{e} \quad (\text{B.3})$$

and, for $\frac{d}{dt}\vec{E}$, as

$$\frac{d}{dt}\vec{e} = [\epsilon]^{-1}\mathbf{C}^h[\mu]^{-1}\vec{h} = \mathbf{C}^{h*}\vec{h}. \quad (\text{B.4})$$

Once the curl operators have been discretized, the fields in the time domain are computed at the next timestep from the previous fields, on the basis of the leap frog scheme [79].

Resonant fields, instead, are computed by GdfidL solving an eigenvalue problem derived directly from eqs. B.3 and B.4. ¹ Substituting \vec{h} given by eq. B.3 into eq. B.4 and taking the Fourier harmonic of the time derivative, the equation describing the algebraic eigenvalue problem is found to be:

$$-\mathbf{C}^{h*}\mathbf{C}^e\vec{e} = -\omega^2\vec{e}. \quad (\text{B.5})$$

The lowest nonzero eigenvalues and their corresponding eigenvectors are found with the algorithm by Tückmantel [82].

The S-parameters GdfidL computation proceeds performing a time domain simulation and then a Fourier transform of the histories of the tangential fields at the

¹Resonant fields can be computed by exciting a structure with a broadband pulse, then examining the ringing of the fields. But such an approach can be valid only if a good resolution in frequency is not demanded, given this latter requiring a long simulation time, as $\Delta f = 1/T$.

ports of the structure. At the locations where the waveguide crosses the boundary of the computational volume, Absorbing Boundary Conditions (ABCs) are applied. They are implemented into the code as orthogonal functions which are the tangential fields of the TE, TM and TEM waveguides modes.

In order to compute wakepotentials, finally, a rigid beam is allowed to traverse the computational volume. For long range wakefields, ABCs must be applied where the beam enters and exits the cavity. The primary field of the charge, in this case, cannot be expanded in the waveguides modes. Thus, with known velocity of the charge, the primary field at the ABCs is also known and can be subtracted from the total field. The scattered waves remaining can be expanded in orthogonal waveguide modes.

As a concluding remark, generally the solution of difference equations does differ from the solution of the differential equations. There are two main sources of error, i.e. the approximation of the differential equation by a difference equation - for a homogeneous mesh this error is proportional to the square of the mesh spacing - and the error due to the approximation of the material distribution. The coefficients of the difference equations depend on the material parameters. In the “staircase” approximation, constant material parameters are assumed in each cell of the grid. Better approximations use the prismatic cells. GdfidL implements a mesh-filling that is constructed by a boolean combination of prismatic fillings. The reason for such a choice is that the finite difference coefficients for a field component depend only on the material in the immediate vicinity of the edge where the component is defined on. This guarantees a reduction of the frequency error by a factor of ten, as compared to a prismatic filling [83].

Bibliography

- [1] Lyndon Evans and Philip Bryant. Lhc machine. *Journal of Instrumentation*, 3(08):S08001, 2008.
- [2] Lyndon Evans. The large hadron collider. *New Journal of Physics*, 9(9):335, 2007.
- [3] Peter W. Higgs. Broken symmetries and the masses of gauge bosons. *Phys. Rev. Lett.*, 13:508–509, Oct 1964.
- [4] F. Englert and R. Brout. Broken symmetry and the mass of gauge vector mesons. *Phys. Rev. Lett.*, 13:321–323, Aug 1964.
- [5] Mike Lamont. Status of the lhc. *Journal of Physics: Conference Series*, 455(1):012001, 2013.
- [6] The LHCb collaboration. Observation of J/ψ Resonances Consistent with Pentaquark States in $\Lambda_b^0 \rightarrow J/\psi K^- p$ Decays. *Phys. Rev. Lett.*, 115(7):072001, 2015.
- [7] The ATLAS Collaboration. Observation of a new particle in the search for the standard model higgs boson with the atlas detector at the lhc. *Physics Letters B*, 716(1):1 – 29, 2012.
- [8] The ATLAS Collaboration. A particle consistent with the higgs boson observed with the atlas detector at the large hadron collider. *Science*, 338(6114):1576–1582, 2012.
- [9] The CMS collaboration. Observation of a new boson at a mass of 125 GeV with the CMS experiment at the LHC. *Phys. Lett.*, B716:30–61, 2012.
- [10] The CMS collaboration. A New Boson with a Mass of 125 GeV Observed with the CMS Experiment at the Large Hadron Collider. *Science*, 338:1569–1575, 2012.
- [11] European Strategy for Particle Physics, adopted by the CERN Council at a special session at ministerial level in Lisbon in 2006. <http://cern.ch/council/en/EuropeanStrategy/ESParticlePhysics.html>.
- [12] European Strategy for Particle Physics Update 2013, CERN-Council-S/106, adopted at a special session in the Brussels on 30 May 2013. <http://cern.ch/council/en/EuropeanStrategy/ESParticlePhysics.html>.

- [13] The HL-LHC collaboration. HL-LHC Preliminary Design Report Deliverable: D1.5. Technical report, 2014. CERN-ACC-2014-0300.
- [14] E. Metral. Beam intensity limitations, Deliverable: D2.4. Technical report, 2014. CERN-ACC-2014-0297.
- [15] O. Brüning et al. LHC Design Report. Technical report, Geneva, 2004. CERN-2004-003.
- [16] R.W. Assmann et al. Requirements for the LHC collimation system. *Proceedings of the 8th European Particle Accelerator Conference*, pages 197–199, 2002.
- [17] R.W. Assmann et al. An improved collimation system for the LHC. *Proceedings of the 9th European Particle Accelerator Conference*, pages 536–538, 2004.
- [18] R.W. Assmann. Collimation for LHC high intensity beams. *Proceedings of the 46th ICFA Advanced Beam Dynamics Workshop on High-Intensity and High-Brightness Hadron Beams HB2010*, pages 21–33, 2010.
- [19] A. Bertarelli et al. The Mechanical Design for the LHC Collimators. *Proceedings of European Particle Accelerator Conference EPAC04*, pages 545–547, 2004. LHC-PROJECT-REPORT-786.
- [20] E. Metral et al. Transverse Impedance of LHC Collimators. *Proceedings of Particle Accelerator Conference PAC07*, pages 2003–2005, 2007. CERN-LHC-PROJECT-REPORT-1015.
- [21] N Mounet et al. Impedances of Two Dimensional Multilayer Cylindrical and Flat Chambers in the Non-Ultrarelativistic Case. *Proceedings of the 46th ICFA Advanced Beam Dynamics Workshop on High-Intensity and High-Brightness Hadron Beams HB2010*, pages 353–357, 2010.
- [22] A.W. Chao. *Physics of Collective Beam Instabilities in High Energy Accelerators*. Wiley, 1993.
- [23] K.Y. Ng. *Physics of Intensity Dependent Beam Instabilities*. World Scientific, 2005.
- [24] Wolfgang K. H. Panofsky and Melba Phillips. *Classical Electricity and Magnetism*. Addison-Wesley, 1962.
- [25] K. L. F. Bane and P. L. Morton. Deflection by the image current and charges of a beam scraper. *Proceedings of the 1986 Linac Accelerator Conference*, page 490, 1986.
- [26] P. Wilson. The Fundamental Theorem of Beam Loading. Technical report, 1987. SLAC-PUB-4441.
- [27] B. W. Zotter and S. A. Kheifets. *Impedances and Wakes in High Energy Particle Accelerators*. World Scientific, 1998.
- [28] S. Y. Lee. *Accelerator Physics*. World Scientific, 2013.

- [29] L. Palumbo, V.G. Vaccaro, and M. Zobov. Wake fields and impedance. *LNF-94-041-P, C93-09-20.6*, 1994.
- [30] F.J. Sacherer. A longitudinal stability criterion for bunched beams. *IEEE Transactions on Nuclear Science*, 20(3):825–829, 1973.
- [31] B. W. Zotter and F. J. Sacherer. Transverse instabilities of relativistic particle beams in accelerators and storage rings. *Conf.Proc.*, C761110:175–218, 1976.
- [32] D. Boussard. Observation of microwave longitudinal instabilities in the CPS. Technical Report CERN/LAB/II/RF/75-2, CERN, Geneva, 1975.
- [33] E. Keil and W. Schnell. Concerning longitudinal stability in the ISR. Technical Report CERN-ISR-TH-RF-69-48. ISR-TH-RF-69-48, CERN, Geneva, Jul 1969.
- [34] K. W. Robinson. Stability of Beam in Radiofrequency Systems. Technical Report CEAL-1010, Cambridge Electron Accelerator, 1964.
- [35] N. Mounet. *The LHC Transverse Coupled-Bunch Instability*. PhD thesis, Ecole Polytechnique, Lausanne, Mar 2012. Presented 2012.
- [36] G. Rumolo and F. Zimmermann. Electron cloud simulations: beam instabilities and wakefields. *Phys. Rev. ST Accel. Beams*, 5:121002, Dec 2002.
- [37] J. F. Esteban Müller et al. Probing the LHC impedance with single bunches. Technical Report CERN-ATS-Note-2013-001 MD, Jan 2013.
- [38] B. Salvachua et al. Results on nominal collimator settings MD at 4 TeV. Technical report, Jun 2012.
- [39] N. Mounet et al. Beam stability with separated beams at 6.5 tev. In *LHC Beam Operation Workshop Evian 17-20 December 2012*, 2012.
- [40] W. Bruns. <http://www.gdfidl.de>.
- [41] Y. H. Chin. User's Guide for ABCI. <http://abci.kek.jp/abci.htm>.
- [42] G.V. Stupakov. Geometrical wake of a smooth taper. *Part.Accel.*, 56:83–97, 1996.
- [43] Robert L. Gluckstern et al. Coupling impedance of beam pipes of general cross-section. *Phys.Rev.*, E47:656–663, 1993.
- [44] G. Stupakov. Low Frequency Impedance of Tapered Transitions with Arbitrary Cross Sections. *Phys.Rev.ST Accel.Beams*, 10:094401, 2007.
- [45] R.W. Assmann et al. LHC Collimation: Design and Results from Prototyping and Beam Tests. pages 1078–1080., 2005.
- [46] Kaoru Yokoya. Resistive wall impedance of beam pipes of general cross-section. *Part.Accel.*, 41:221–248, 1993.
- [47] A. Grudiev. Simulation of longitudinal and transverse impedances of trapped modes in lhc secondary collimator. *CERN AB-Note-2005-042*, 2005.

- [48] H. A. Day. *Measurements and Simulations of Impedance Reduction Techniques in Particle Accelerators*. PhD thesis, Manchester U., 2013. Presented 28 Jun 2013.
- [49] B. Salvant. Impedance of the TCTP design. Presented at 12th TCTP design meeting, 2011.
- [50] N. Mounet et al. Impedance and instabilities. In *LHC Beam Operation Workshop Evian 2-4 December 2014*, 2014.
- [51] E. Metral. Initial estimate of machine impedance. (Milestone Report MS29, CERN-ACC-2014-0005), Jan 2014.
- [52] N. Mounet et al. Transverse impedance in the HL-LHC era. Presented at the 3rd Joint HiLumi LHC-LARP Annual Meeting, Daresbury, UK, 2013.
- [53] D. Wollmann et al. Beam feasibility study of a collimator with in-jaw beam position monitors. *Nuclear Instruments and Methods in Physics Research Section A: Accelerators, Spectrometers, Detectors and Associated Equipment*, 768:62 – 68, 2014.
- [54] S. Krinsky et al. Impedance of finite length resistive cylinder. *Phys. Rev. ST Accel. Beams*, 7:114401, Nov 2004.
- [55] Gennady Stupakov. Resistive wall impedance of an insert. *Phys. Rev. ST Accel. Beams*, 8:044401, Apr 2005.
- [56] Y. Shobuda et al. Coupling impedances of a resistive insert in a vacuum chamber. *Phys. Rev. ST Accel. Beams*, 12:094401, Sep 2009.
- [57] N. Biancacci et al. Impedance studies of 2d azimuthally symmetric devices of finite length. *Phys. Rev. ST Accel. Beams*, 17:021001, Feb 2014.
- [58] CST Computer Simulation Technology AG.
- [59] O. Frasciello et al. Wake fields and impedances calculations with GdfidL, MMM and CST for benchmarking purposes, 2014. Contributed talk at BE-ABP Impedance meeting, February 2nd, CERN, Geneva, Switzerland.
- [60] H. Tsutsui et al. Transverse Coupling Impedance of a Simplified Ferrite Licker Magnet Model. Technical report, 2000. LHC-PROJECT-NOTE-234.
- [61] H. Tsutsui. Some Simplified Models of Ferrite Kicker Magnet for Calculations of Longitudinal Coupling Impedance. Technical report, 2000. CERN-SL-2000-004 AP.
- [62] L.D. Landau and E.M. Lifshitz. *Electrodynamics of Continuous Media (Second Edition Revised and Enlarged)*, volume 8 of *Course of Theoretical Physics*. Pergamon, Amsterdam, 1984.
- [63] The Sage Developers. *Sage Mathematics Software (Version 6.8)*, 2015. <http://www.sagemath.org>.

- [64] R. Boni et al. Study of the parasitic mode absorbers for the Frascati ϕ -factory rf cavities. Technical Report LNF-93-014-P, INFN-LNF, Frascati, Apr 1993.
- [65] S. Ramo, J. R. Whinnery, and T. Van Duzer. *Fields and Waves in Communication Electronics (3rd Edition)*. John Wiley & Sons, 1994.
- [66] Frasciello O. et al. Geometric beam coupling impedance of LHC secondary collimators. *Nuclear Instruments and Methods in Physics Research Section A: Accelerators, Spectrometers, Detectors and Associated Equipment*, <http://dx.doi.org/10.1016/j.nima.2015.11.139>.
- [67] O. Frasciello et al. Present status and future plans of LHC collimators wake fields and impedance simulations, 2015. Contributed talk at BE-ABP Impedance meeting, March 23rd, CERN, Geneva, Switzerland.
- [68] N. Biancacci et al. Impedance bench measurements on TCTP collimator with ferrite, 2014. Contributed talk at BE-ABP Impedance meeting, August 8th, CERN, Geneva, Switzerland.
- [69] N. Biancacci et al. Impedance bench measurements on TCTP and SLAC collimators, 2014. Contributed talk at BE-ABP Impedance meeting, April 14th, CERN, Geneva, Switzerland.
- [70] O. Frasciello et al. Beam coupling impedance of the new LHC collimators, 2015. Contributed talk at 101st National Congress of the Italian Physical Society (SIF), September 24th, Rome, Italy.
- [71] J. Uythoven et al. Upgrades to the LHC injection and beam dumping systems for the HL-LHC project. In *Proceedings of IPAC 2014*.
- [72] J. Uythoven et al. Injection protection upgrade for the HL-LHC. In *Proceedings of IPAC 2015*.
- [73] N. Mounet et al. Impedance effects on beam stability. In *LHC Beam Operation Workshop Evian 2011*, 2011.
- [74] J. Esteban Muller et al. Measurements of the LHC longitudinal resistive impedance with beam. *Proceedings of the 48th ICFA Advanced Beam Dynamics Workshop on High-Intensity and High-Brightness Hadron Beams HB2012*, 2012.
- [75] B. Podobedov and I. Zagorodnov. Impedance minimization by nonlinear tapering. In *Proceedings of Particle Accelerator Conference PAC07*, pages 2006–2008, Albuquerque, New Mexico, USA, 2007.
- [76] B. Salvant and L. Gentini. Private communications.
- [77] N. Biancacci. Update on the HL-LHC impedance budget, 2014. Contributed talk at HL-LHC WP 2 Task 2.4 meeting, November 19th, CERN, Geneva, Switzerland.
- [78] B. Salvant. Private communications.

-
- [79] K. Yee. Numerical solution of initial boundary value problems involving Maxwell's equations in isotropic media. *Antennas and Propagation, IEEE Transactions on*, 14(3):302–307, 1966.
- [80] T. Weiland. Eine Methode zur Lösung der Maxwell'schen Gleichungen für sechskomponentige Felder auf diskreter Basis. *Archiv für Elektrotechnik und Übertragungstechnik, (Electronics and Communication)*, Band 31 (1977), Seiten 116-120.
- [81] W. Bruns. GdfidL: a finite difference program with reduced memory and CPU usage. In *Proceedings of Particle Accelerator Conference*, volume 2, pages 2651–2653, 1997.
- [82] Tückmantel, J. An improved version of the eigenvector processor SAP applied in URMEL. Technical report, 1985. CERN-EF/RF-85-4.
- [83] Bruns, W. GdfidL with generalized diagonal fillings and periodic boundary conditions. <http://www.gdfidl.de>.